

Electron capture and emission dynamics of self-assembled quantum dots

INAUGURAL-DISSERTATION

zur Erlangung des Doktorgrades der
Mathematisch-Naturwissenschaftlichen Fakultät der
Heinrich-Heine-Universität Düsseldorf

vorgelegt von:

Laurin Maximilian Schnorr

aus Düsseldorf

Düsseldorf, Dezember 2021

aus dem Institut für Experimentelle Physik der kondensierten Materie der
Heinrich-Heine-Universität Düsseldorf

Gedruckt mit der Genehmigung der
Mathematisch-Naturwissenschaftlichen Fakultät der
Heinrich-Heine-Universität Düsseldorf

Berichterstatter:

1. Prof. Dr. Thomas Heinzel
2. Prof. Dr. Reinhold Egger

Tag der mündlichen Prüfung: 17.2.2022

Abstract

This thesis is concerned with the study of electron capture and emission dynamics of InAs self-assembled quantum dots (SAQDs) that are embedded into a Schottky diode structure grown by molecular beam epitaxy. SAQDs are small islands of semiconducting material in which charge carriers can only occupy a discrete density of states. The charge state of the SAQDs is measured via the capacitance of the Schottky diode. A sudden change in the applied voltage causes the SAQDs to either emit or capture electrons, the time dependence of which is analyzed using Deep Level Transient Spectroscopy (DLTS) and Laplace DLTS (LDLTS) at different temperatures.

The goal of this thesis is to electronically measure the charge transfer dynamics of SAQDs in doped sample structures with large distances (> 100 nm) between the quantum dots and the electrodes, as commonly found in optoelectronic devices. Measurements are conducted under experimental conditions that have been carefully avoided before, where assumptions about the dominance of a single charge transfer process can no longer be justified. First, the implementation of the inverse Laplace transform algorithm and the details of its application to realistic measurement data is described. Subsequently, temperature and voltage dependent measurements of the electron emission are analyzed via LDLTS and compared to results of other established methods. Furthermore, the capture rates are measured as a function of the applied bias voltage at $T = 7$ K and $T = 77$ K, where the interplay between the capture and emission dynamics could be observed and modeled quantitatively. The model allows for the extrapolation of the steady state electron occupancy of the SAQDs which is found to be orders of magnitude larger than the electron distribution in the bulk material, indicating an additional electron source filling the SAQDs. The hysteretic capacitance-voltage (CV) behavior that has previously only been explained qualitatively could be quantitatively predicted without modification to the model, and features in the CV trace could be unambiguously related to the sample and SAQD properties.

Eidesstattliche Versicherung

Ich versichere an Eides Statt, dass die Dissertation von mir selbständig und ohne unzulässige fremde Hilfe unter Beachtung der „Grundsätze zur Sicherung guter wissenschaftlicher Praxis an der Heinrich-Heine-Universität Düsseldorf“ erstellt worden ist.

Ort, Datum

Laurin Maximilian Schnorr

Contents

Introduction	1
1 Fundamental concepts	5
1.1 Quantum dots	5
1.1.1 Self-assembled growth	6
1.1.2 The Fock-Darwin spectrum	8
1.1.3 Coulomb blockade	9
1.2 The Schottky diode	10
1.2.1 Schottky junction in equilibrium	10
1.2.2 Band structure under external bias	12
1.2.3 IV characteristics	12
1.2.4 CV characteristics	13
1.3 Defect states	13
1.4 Carrier dynamics	14
1.4.1 Pure thermal activation	14
1.4.2 Electric field effects	15
1.4.3 Leakage currents	17
1.5 Charge transients	18
1.6 Capacitance transients	19
2 Experimental techniques	21
2.1 Sample structure	21
2.2 Cryogenic setup	23
2.2.1 Liquid nitrogen dewar	23
2.2.2 Dilution refrigerator	24
2.3 Bias pulses	24
2.4 Capacitance measurements	25
2.5 Transient recording	27
2.6 Device synchronization	28
3 Data analysis techniques	31
3.1 Deep Level Transient Spectroscopy	31
3.1.1 Boxcar DLTS	32
3.1.2 Lock-in DLTS	33
3.2 Numerical Laplace inversion	35
3.2.1 Discretization	35

3.2.2	Tikhonov regularization	37
3.2.3	Implementation	37
3.2.4	Offset correction	39
4	Laplace DLTS on SAQDs	45
4.1	Context	45
4.2	Paper 1	46
5	Capture and emission dynamics far from equilibrium with the environment	61
5.1	Context	61
5.2	Paper 2	62
6	CV-Hysteresis at low temperatures	79
6.1	Context	79
6.2	Paper 3	80
7	Conclusion and outlook	93
	Growth protocol for sample #14691	95
	Bibliography	97
	Danksagung	105

Introduction

Self-assembled quantum dots (SAQDs) are electronically zero-dimensional structures of semiconducting material that are formed during epitaxial growth on a suitable host substrate [1, 2]. Their dimensions are each in the order of magnitude of the Fermi wavelength, giving rise to a discrete, atom-like density of states (DOS) that earned such systems the name *artificial atoms*. In contrast to real atoms, however, SAQDs are two to three orders of magnitude larger and the confinement potential is of different shape, leading to a different energy spectrum with smaller level spacing [3–5]. These differences make properties of the SAQDs electronically accessible that would be impossible to observe or alter in real atoms, which has created interest in SAQDs for fundamental research [6–10]. SAQDs have also proven to be suitable for practical applications, especially in the field of optoelectronics where they are used in light emitting diodes [11] and laser structures [12, 13] operating in the infrared range. They are also studied as a possible way to improve the performance of solar cells [14, 15]. The fabrication of SAQD based single photon sources [6, 16] and on-demand sources for entangled photons [8] alongside the possible use of SAQDs as spin quantum bits [7, 9] make them interesting regarding the ongoing efforts in the miniaturization of quantum computers. Concerning classical computation, possible SAQD-based applications are in the field of memory devices like memristors [17] and fast memory cells [18–20] that rely on the charge stored inside the SAQDs to represent one classical bit of information.

Depending on external parameters like temperature and bias voltage, as well as the sample structure that defines the local potential and electric field in the vicinity of the SAQDs [21, 22], charge transfer time scales between 600 ps [23] and 10^4 s [19] have been reported. Ideally, a device can be switched between such two time scales by applying a voltage to allow for both fast writing of information as well as long storage times without the need for the information being refreshed. The dynamics of these charge transfers have been studied using various techniques like transconductance spectroscopy [10, 24], which measures the influence of the charge stored inside SAQDs on a nearby conductive channel or capacitance-voltage (CV) spectroscopy [4, 5, 25–28], which relies on elastic tunneling of charge carriers between the SAQD states and the Fermi edge inside a reservoir that is usually less than 30 nm away. Here, the dynamics are observed as a decrease in the samples response with increasing frequency of an AC driving voltage of small amplitude, as the SAQDs become too slow to get charged and discharged during one cycle. In such experiments both the dynamics of the emission and the capture process enter into the observed frequency response of the sample, giving rise to an observable average charge transfer rate [4, 5].

Deep level transient spectroscopy (DLTS) [29] on the other hand does not rely on direct tunneling between the SAQDs and the Fermi edge inside a reservoir, instead the charge inside the SAQD layer affects the junction capacitance of a p-n or Schottky diode in which the quantum dots are embedded. This also allows for larger distances between the quantum dots and the contacts, resembling the layout in the optoelectronic applications [11, 12] of SAQDs. Several DLTS measurements on such systems have been published before [30–39]. In contrast, only few *Laplace DLTS* [40] measurements [41, 42] that rely on the inverse Laplace transform of (multi-)exponential capacitance transients, which allows for a much higher rate resolution have been published. All of these DLTS and LDLTS measurements were however limited to emission dynamics and to temperature regimes where thermal emission is the dominating influence on the dynamics. Only few works have studied the tunneling regime using these techniques [43, 44].

The goal of this thesis was to electronically measure the charge transfer dynamics of SAQDs in doped sample structures with large distances (> 100 nm) between the quantum dots and the electrodes as commonly found in optoelectronic devices [11, 12]. Measurements should be conducted under experimental conditions that have been carefully avoided before [30–39], where assumptions about the dominance of a single charge transfer process can no longer be justified. When advantageous, the high-resolution LDLTS technique should be used for which a Laplace inversion algorithm suited for typical transient data had to be implemented. A deeper understanding of the charge transfer dynamics in such devices may help in finding ways to improve their design such that the performance in existing fields of their practical application can be enhanced, e.g. by increasing the intrinsic modulation bandwidth of semiconductor lasers [45, 46]. The results presented in Paper 1 [47] show the first high-resolution LDLTS measurements of the emission rates from the one- and two-electron state covering a continuous temperature range from the tunneling regime into the thermal regime. A similar study has been performed previously using conventional DLTS [44], where the resolution was not high enough to distinguish the emission from individual charge states. The emission rates for the one- and two-electron state obtained here could be modeled quantitatively in the entire temperature interval including the transition from tunneling dominated to thermally dominated emission and are in agreement with the results obtained via the established measurement procedures in the limits of low and high temperatures, respectively. Additionally the voltage dependence of the emission rates at $T = 77$ K was studied for the first time using isothermal LDLTS for the one- and two-electron state and explained in terms of the effect of the electric field on the confinement potential. Previous investigations of this effect required temperature sweeps for each bias voltage under study [43] introducing unavoidable uncertainties compared to the direct measurements using LDLTS.

Electrical measurements of the charging dynamics on these structures have so far been limited to bias voltage regimes where the emission of electrons from the SAQDs is the dominant process and the capture of electrons into the quantum dots could be neglected [30–39]. Optical measurements of the charge capture process have been reported [48–50] as well as indirect electronic measurements of the influence of the capture dynamics on subsequent emission processes [37, 51]. Direct electrical measurements of the capture

dynamics of SAQDs in these sample structures, however, have not been reported before. Such measurements in the thermal regime at $T = 77$ K are presented in Paper 2 [52] where the capture dynamics were directly measured using high resolution isothermal LDLTS. Furthermore, isothermal DLTS measurements were conducted over a large bias voltage interval covering on the one hand regimes where either electron capture or emission are dominant, while the other can be neglected, and on the other hand the transition regime. In this regime the observed behavior could only be described in terms of an effective charge transfer rate that was derived from a simple two-step charging model. The emission rates from the one- and two-electron states obtained from said model are in agreement with the ones measured in Paper 1, while the capture rates showed no dependence on the charge state of the SAQDs at this temperature. In contrast to the voltage dependence of the emission rates the capture rate was found to increase with an increased bias voltage. This indicates that the capture dynamics are dominated by the energetic alignment of the SAQD layer within the band structure, rather than by the deformation of the confining potential due to the electric field. This deformation of the potential, however, is known to be the dominant cause for the voltage dependence of the emission rates, as discussed in Paper 1. The magnitude of the capture rate was also found to be significantly larger than it would be expected when assuming a thermal equilibrium between the SAQDs and the electron reservoir at the back contact of the sample. The applied model allows for the calculation of the charge density inside the SAQD layer as a function of time under a bias voltage with an arbitrary time dependence. Thus, it was possible to extrapolate the steady state occupancy of the SAQDs as a function of the bias voltage, which was found to deviate from the occupation probability in the surrounding bulk material.

Paper 3 [53] extends the isothermal methods introduced in Paper 2 to the tunneling regime at $T = 7$ K. These measurements were motivated on the one hand by the more pronounced influence of the applied bias voltages on the charge transfer rates due to the lack of competing thermal activation rates. On the other hand the generally slower charging/discharging times at lower temperatures allow for the observation of the dynamics of SAQD states higher than the two-electron state, which are unobservable at $T = 77$ K within the experimentally accessible time scale. It was found that both for electron emission and capture processes the signatures of the s-, p- and d-orbitals of the SAQDs could be observed, with the charge state dependence of the emission rates being much stronger than for the capture rates. Tunneling emission has been observed using similar methods from the s- and p-states before [43]. The results presented in Paper 3 are, however, the first direct electrical measurements of the capture rates at low temperatures, covering, like in Paper 2, a large bias voltage interval where the interplay of the capture and emission processes can in general not be neglected. As already observed at $T = 77$ K, the capture rates were found to increase with an increased bias voltage indicating that also in the tunneling regime the capture dynamics are dominated by the energetic alignment of the SAQD layer instead of the electric field effects on the confining potential. Hence, the sign of the voltage dependence of the capture rate does not change over the temperature range studied in this thesis. Furthermore, it was found that the capture rate decreases with an increased electron occupancy of the SAQDs which can be understood in terms of the Coulomb blockade [54]. The extended model used to reproduce the results of the transient measurements at $T = 7$ K

could also be applied without modification to quantitatively model the CV hysteresis that has previously been observed at quasi-continuous bias sweeps for comparable structures [55–58] as well as in samples where the charge inside the SAQDs affects the conductivity of nearby channels [20, 21, 56, 59–65]. The voltage and time dependent charging state predicted from the model agrees well with the values obtained from the experimental data and allows for a clear attribution of the features observed in a hysteretic CV trace to the properties of the SAQDs and the sample layout.

This thesis is organized as follows. Chapter 1 introduces the fundamental concepts of semiconductor physics relevant for this thesis, most prominently the properties of SAQDs, the physics of the Schottky diode and the origins of capacitance transients are discussed. Chapter 2 describes the experimental techniques used throughout this thesis, starting with the layout of the sample structure and continuing with the cryogenic and electronic measurement setups used in the experiments. The relevant data analysis techniques are presented in chapter 3. First, the working principle of the DLTS technique is explained. Then the relevant numerics as well as the practical details concerning the application of the Laplace inversion algorithm implemented in this thesis are given. Within this thesis three papers concerning various hitherto not studied aspects of the charge transfer dynamics of SAQDs have been published, which are included in chapters 4 - 6. A conclusion and an outlook to potential research in the future is given in chapter 7.

Chapter 1

Fundamental concepts

1.1 Quantum dots

In quantum dots, electric charge carriers are confined by a potential well in all three dimensions on a scale that leads to a size quantization of the available quantum mechanical states that can be occupied by either electrons, holes or both. The relevant length scale is the de-Broglie wavelength [66] of a particle at the Fermi edge inside the material, which decreases with an increasing particle density n , with the exact relationship depending on the dimensionality. Hence, compared to metals, semiconductors with their generally low particle densities are particularly well suited since size quantization effects can be observed at larger scales. Since the fundamental principles of the relevant physics in quantum dots are qualitatively identical for electrons and holes throughout this chapter the discussion will be given exclusively for electrons.

In the most fundamental one-dimensional particle in a box scenario, where two infinitely high and infinitely steep potential barriers confine the particle to the left and right, one can observe that the spacing between the energy eigenvalues of the corresponding Hamiltonian scales with the inverse square of the confining length [67].

Qualitatively this behavior can also be observed in systems with finite confinement potentials that act in all three dimensions [67]. Such a confining potential $V(\vec{r})$ can be realized by different techniques:

In colloidal quantum dots (CQD), a semiconducting material is crystallized in a suitable solution under such conditions that the resulting crystalline grains are of appropriate size (e.g. typically ≈ 5 nm diameter for CdSe CQDs [68]). These types of quantum dots can be mass-produced and chemically modified to a large degree which makes them suitable for biotechnology and medical applications [69]. They are, however, not easy to access in purely electronic measurements.

Lithographically and electrostatically defined quantum dots can be created by locally depleting a conductive layer using lithographically defined etched mesa structures [70] or electrostatic gates [71], respectively. These quantum dots can be electronically contacted using standard processing techniques and thus can be easily studied electronically. Since these types of quantum dots have to be contacted individually one

is limited to experiments on a small number. They can, however, be positioned with high precision to create e.g. quantum dot molecules [72].

Self-assembled quantum dots (SAQDs) [1,2] are quantum dots that are produced by self-assembled growth of a semiconducting material on a host substrate. The criteria that a combination of two materials has to fulfill in order to yield self-assembled quantum dots of usable dimensions will be discussed in the following sections.

1.1.1 Self-assembled growth

Molecular beam epitaxy (MBE) [73] is used to deposit few monolayers of the SAQD guest material on top of the host substrate. For the sample studied in this thesis the SAQD material was InAs and the substrate GaAs, however, other combinations are established as well, e.g. Ge dots on Si [74], GaN on AlN [75] or InP on $\text{Ga}_{0.5}\text{In}_{0.5}\text{P}$ [30]. In thin film deposition using MBE there are three growth modes that can be distinguished:

- the Volmer-Weber growth mode [76], where deposited material forms isolated islands on top of the substrate,
- the Frank-van der Merwe mode [77], where new material completes a monolayer before beginning a new one such that only the uppermost layer can be incomplete,
- and the Stranski-Krastanov mode [78] where deposited material forms a few monolayer thick *wetting layer* on top of which isolated islands are formed.

An illustration of the different growth modes is shown in figure 1.1.

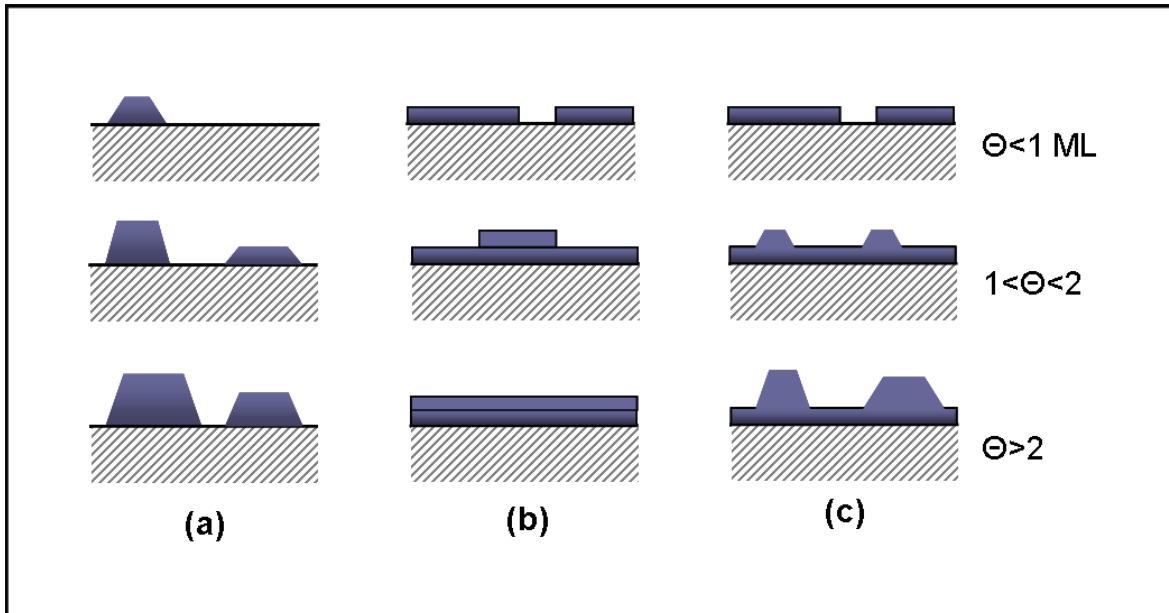


Figure 1.1: Epitaxial growth of thin films as function of the coverage factor Θ in the Volmer-Weber (a), Frank-van der Merwe (b), and Stranski-Krastanov (c) mode. (Public domain)

A material grows according to the growth mode that minimizes the total energy of the layers that depends on surface, volume interface and strain contributions. In a simplified model [79], Volmer-Weber growth corresponds to a situation where the energetic cost per unit area of the host material's surface is smaller than the cost of the guest material's surface and the cost of the interface between host and guest material combined. Thus, an energetic optimum is reached when as much of the host material remains uncovered. In the opposite case when it is energetically favorable to cover as much of the host material's surface as possible, Frank-van der Merwe growth will take place. Stranski-Krastanov growth takes place only when there is a lattice mismatch between the two materials. The first layers of the guest material adapt to the lattice constant of the host material leading to an increased energetic cost for the deposition of the guest material close to the interface per unit area caused by the elastic strain. Due to relaxation of the lattice strain in subsequent layers it becomes energetically favorable to deposit new guest atoms on top of higher layers where the lattice strain has relaxed the most. Thus, after a few monolayers known as the *wetting layer* island growth can be observed.

For the combination of InAs on top of GaAs used in this thesis, the material arranges itself in the Stranski-Krastanov mode. After the wetting layer is formed, SAQDs are formed with a height of ≈ 8 nm and a circular base with a diameter of ≈ 30 nm. A transmission electron microscopy (TEM) image of a representative InAs-SAQD grown under similar conditions as the dots studied in this thesis is shown in figure 1.2.

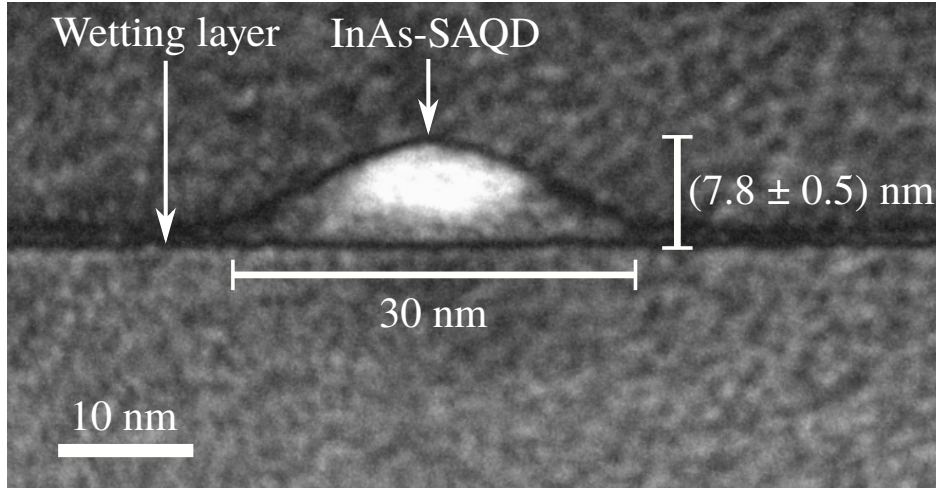


Figure 1.2: Transmission electron microscopy image of a representative InAs-SAQD grown under similar conditions as the dots studied in this thesis. Measured by Jean-Michel Chauveau and Arne Ludwig and included with their permission.

The ensemble of SAQDs grown in such a way is very homogeneous in size, with measurements showing a variance of only $\approx 10\%$ [1]. The broadening of their size distribution due to Ostwald ripening [80] is inhibited by the growth kinetics [81,82] until the SAQD layer is capped.

1.1.2 The Fock-Darwin spectrum

In order to model the energy spectrum in SAQDs and its magnetic field dependence qualitatively the Fock-Darwin spectrum [83, 84] is often used since the quantum mechanical equations can be solved analytically under applied perpendicular magnetic fields B . One assumption justified by the usual shape of SAQDs is that the confinement is much stronger in z -direction (the growth axis) than in x - and y -direction. The significantly larger energy spacing due to the strong confinement in z -direction is assumed to be strong enough that only the respective ground state can be occupied, reducing the problem to effectively two dimensions. In the xy -plane the rotational symmetric confinement potential

$$V_{FD}(r) = \frac{1}{2}m^*\omega_0^2 r^2 \quad (1.1)$$

is defined, with m^* denoting the effective electron mass in the SAQD material and ω_0 as a scaling parameter.

From the solution of the resulting Schrödinger equation the energy eigenvalues

$$E_{n,l} = (2n + |l| + 1) \hbar\Omega + \frac{1}{2}\hbar\omega_C l \quad (1.2)$$

where

$$\Omega = \sqrt{\omega_0^2 + \frac{1}{4}\omega_C^2} \quad (1.3)$$

and

$$\omega_C = \frac{qB}{m^*} \quad (1.4)$$

with the positive elementary charge q can be obtained [85]. The main quantum number n and the angular momentum quantum number l enumerate the allowed eigenstates of the system under the constraints

$$l = 0, \pm 1, \pm 2 \dots \quad (1.5)$$

$$n = 0, 1, 2, \dots, l \quad (1.6)$$

where each enumerated eigenstate is still spin-degenerate. Since all results presented in this thesis did not involve any applied magnetic field the following discussions will be restricted to the case $B = 0$. A detailed discussion of the magnetic field evolution of the eigenstates can be found elsewhere, e.g. Refs. [85, 86].

For $B = 0$ it follows that $\omega_C = 0$ and thus $\Omega = \omega_0$. It becomes obvious from eq. (1.2) that for $B = 0$ the spectrum is degenerate with respect to the sign of l . The resulting energy spacing in units of $\hbar\omega_0$ is given alongside the associated combination of quantum numbers in figure 1.3 (left). Note that each Fock-Darwin state represented by the quantum numbers (n, l) can be occupied by two electrons with opposite spin. The labeling of the states along the energy axis as s-, p- and d-states stems from the analogy of quantum dots (sometimes referred to as *artificial atoms*) with real atoms and is the common way to refer to a particular SAQD state and will be used throughout this thesis. It should be noted that, due to the broken symmetry between

the z -direction and the xy -plane, the p-states of the Fock-Darwin spectrum together contain only four instead of six electrons as compared to the energy spectrum of the hydrogen atom. The missing two electrons associated with the p_z orbital are, due to the assumed strong confinement in that direction, at such high energies that they are not considered to be bound states. For SAQDs comparable to the ones studied in this thesis this assumption is verified by numerous experiments, e.g. Refs. [3–5].

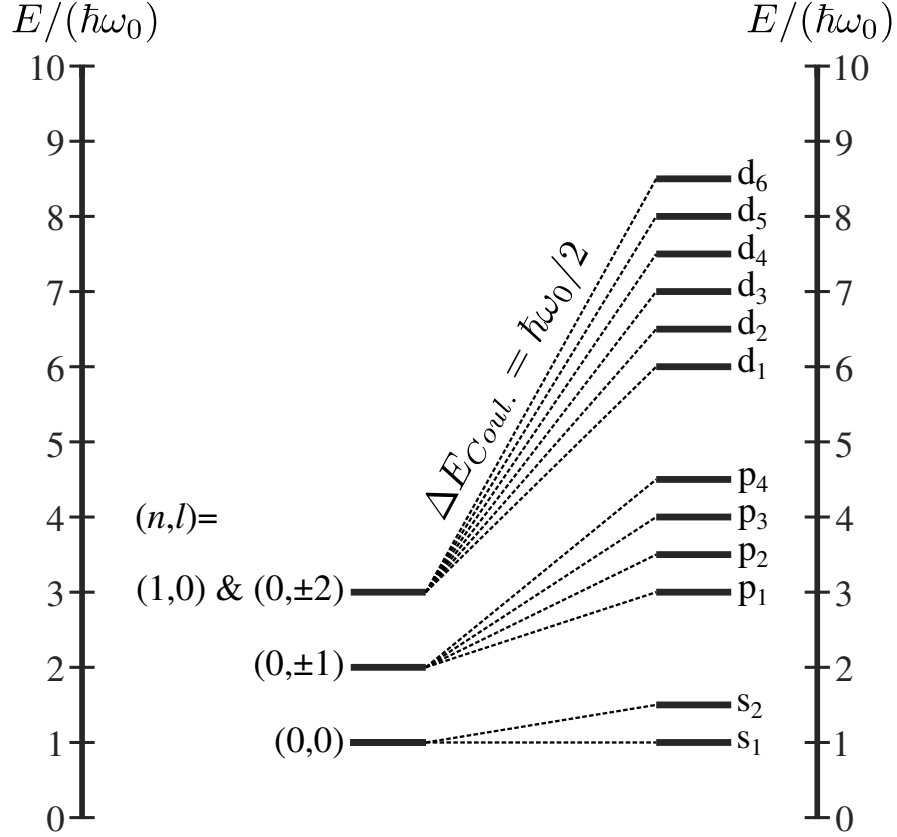


Figure 1.3: Fock-Darwin spectrum for spin-degenerate electrons without (left) and with (right) Coulomb interaction.

1.1.3 Coulomb blockade

Conductive material that is embedded in a dielectric host system bears a self-capacitance C_Σ which is proportional to its radius. For small conductive islands this self-capacitance is small and hence, when such an island is charged with one elementary charge, the energy necessary to bring another elementary charge onto it, given by

$$\Delta E_{Coul.} = \frac{q^2}{C_\Sigma} \quad (1.7)$$

can become comparable to the quantization energy spacing $\hbar\omega_0$. The Coulomb blockade energy has to be surpassed for all but the first electron to enter the SAQD. A sketch of the resulting energy spectrum under the assumption $\Delta E_{Coul.} = \hbar\omega_0/2$ is shown in figure 1.3 (right) in units of $\hbar\omega_0$. The degeneracies are lifted since each subsequent

electron that enters the SAQD will have a higher energy than the one before it. The total energy of a filled SAQD can thus be significantly higher than it would be without the Coulomb blockade. Another consequence is that the higher SAQD states might not be bound states anymore, resulting in a Fock-Darwin spectrum that is cut off at higher energies. The naming conventions of the resulting energy levels are given next to the bars representing each state. Calculations regarding the overlap of the eigenstates of the Fock-Darwin spectrum show that the Coulomb blockade energy between two electrons depends on their quantum numbers, with the Coulomb blockade between the s_1 and s_2 states being the strongest [87].

1.2 The Schottky diode

The layer of SAQDs under study in this work is embedded into a metal/n-type-semiconductor Schottky diode structure, see section 2.1 for the experimental realization, that acts as a detector for the amount of charge stored in the quantum dots. The relevant physics of an n-type Schottky junction according to the Schottky-Mott model will be given in this section which is based upon Refs. [86, 88, 89] and [79].

1.2.1 Schottky junction in equilibrium

The work required to remove a conduction electron from the metal is given by the work function $\Phi_M = E_{vac} - E_F$, where E_{vac} is the vacuum energy level and E_F is the Fermi energy of electrons inside the metal. The equivalent is defined in the same way for the semiconductor side, but is of little use since for non-degenerately doped semiconductors there are no free electrons available at the Fermi level of the semiconductor. Instead, the electron affinity $q\chi = E_{vac} - E_C$ is used, where E_C is the conduction band edge of the semiconductor.

Before the materials are brought into contact each of them is charge neutral and each material has a defined Fermi energy. These two levels are, in general, not identical. Once the materials are brought into contact electrons from the conduction band of the semiconductor will diffuse into the metal since it is energetically favorable, giving rise to a diffusion current I_{diff} . These electrons will leave behind their ionized donor atoms close to the interface, that are now no longer compensated by the donated electrons. Thus, the semiconductor accumulates a positive net charge. Likewise, the additional electrons on the metal side cause the build up of a negative net charge. The volume that has now become charged is referred to as the *space charge region*. The combination of metal and semiconductor as a whole remains charge neutral. The electron concentration in a metal is large compared to the free carriers introduced by the n-doping of the semiconductor. Thus, the positive charge on the semiconductor side that is realized by immobile donor atoms takes up more physical space than the negative charge of the same magnitude in the metal, that is caused by free electrons. Thus, it is generally assumed that the space charge region exists solely on the semiconductor side and the extension into the metal is negligible. Because the semiconductor is devoid of

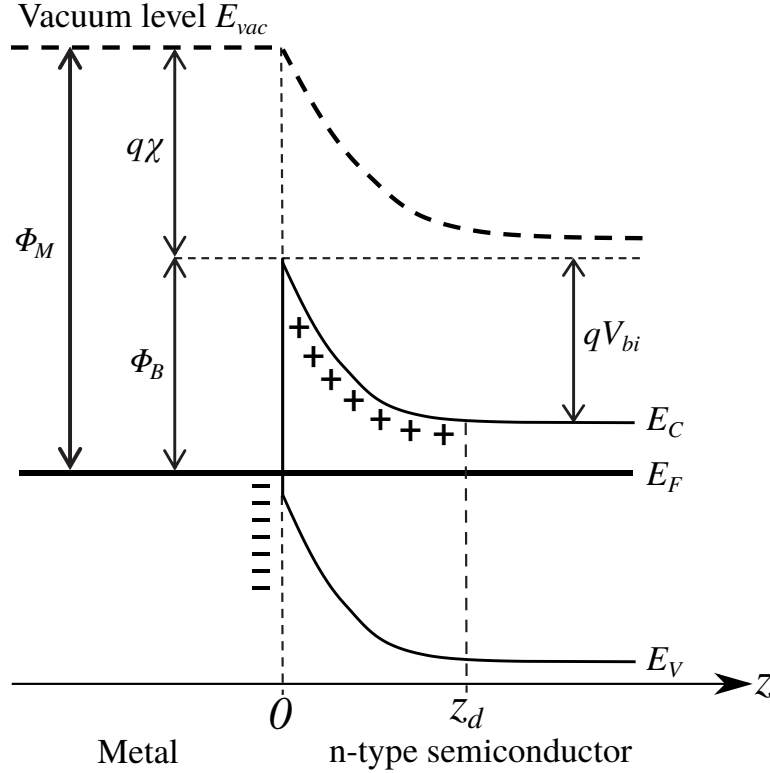


Figure 1.4: Band diagram of an n-type Schottky diode under equilibrium conditions.

free charge carriers inside the space charge region it is also called the *depletion region*, with the size given by the depletion region width z_d .

Since the charge distribution inside the space charge region creates an electric field, a drift current I_{drift} is caused in the opposite direction of I_{diff} . The build up of the space charge region will hence continue until the net current $I = I_{drift} + I_{diff}$ becomes zero, and the system has reached its equilibrium state.

Assuming a homogeneous doping density in the semiconductor the space charge region can be idealized as

$$\rho(z) = \begin{cases} qN_D & \text{for } z \leq z_d \\ 0 & \text{for } z > z_d \end{cases} \quad (1.8)$$

Here it is assumed that for the n-type material the acceptor density N_A is negligible. According to Poisson's equation such a charge distribution gives rise to a linearly varying electric field and a quadratic potential which is the cause of the upwards bending of the energy bands of the semiconductor towards the interface. This situation is shown in figure 1.4. Electrons going from the metal into the semiconductor face the potential barrier $\Phi_B = \Phi_M - q\chi$, also known as the *Schottky barrier*. Electrons going from the semiconductor into the metal have to overcome the *built-in-potential* qV_{bi} . It has to be noted though, that in contrast to this ideal model the Schottky barrier in real world devices is almost independent of the bulk material properties of the metal [90] and instead is mostly governed by surface effects like pinning of the Fermi level by

large densities of surface states [91, 92] and has to be determined experimentally if the exact value is needed.

1.2.2 Band structure under external bias

In the following sections voltages are applied to the metal side with respect to the grounded semiconductor side. Once an external voltage V is applied, the space charge region has to change to satisfy Poisson's equation. As discussed earlier, the width of the space charge region is negligible inside the metal. For negative bias voltages the potential difference across the semiconductor increases and thus the width of the space charge region has to increase. Likewise, for positive bias voltage the width of space charge region decreases. With the size of the space charge region changing on the semiconductor side of the interface, the electric field changes according to Poisson's equation and with it the drift current I_{drift} . The diffusion current remains unchanged so the net current is non-zero. In the same way due to the change of the charge distribution in the semiconductor the barrier electrons have to overcome going from the semiconductor into the metal is changed from $qV_{bi} \rightarrow q(V_{bi} - V)$ while the Schottky barrier Φ_B they have to overcome going from the metal into the semiconductor remains unchanged.

Thus, by applying bias voltages to a Schottky diode it is possible to tune the energetic alignment of the material inside the space charge region. This is used throughout this thesis where the alignment of the SAQD layer is controlled in that way. According to Poisson's equation, a change in the energetic alignment always comes with a change of the local electric field strength.

Both effects are relevant for the behavior of SAQD states (see section 1.4) and can when needed be obtained from self-consistent calculations of the band structure for different applied bias voltages V and temperatures T [93]. These calculations do not rely on the idealizations that were assumed in the analytical discussion of the Schottky junction and also consider temperature dependent material properties, for instance ionization probabilities of the donor atoms.

1.2.3 IV characteristics

It can be shown [89] that the net current that results from the imbalance of the drift- and diffusion currents can be written as

$$I = A R^* T^2 \cdot \exp\left(-\frac{\Phi_B}{k_B T}\right) \cdot \left[\exp\left(\frac{qV}{k_B T}\right) - 1\right] \quad (1.9)$$

with A as the interface area, T the temperature, k_B Boltzmann's constant and R^* the modified Richardson constant defined as

$$R^* = 120 \text{ A cm}^{-2} \text{ K}^{-2} \cdot \frac{m^*}{m_0} \quad (1.10)$$

with the electron mass m_0 and the effective electron mass of the semiconductor m^* .

Realistic Schottky diode structures deviate from this ideal current voltage characteristics due to e.g. interface states [94] or a non-negligible voltage dependent charge redistribution on the metal side [95]. Inhomogeneities on the interface can lead to an effective parallel circuit between rectifying and ohmic contacts while general bulk material resistance and connecting wires give rise to a series resistance [96]. These effects can be extracted from the current voltage characteristics [97] and have been found to be negligible for the sample and the effects studied in this thesis.

1.2.4 CV characteristics

In analogy to the plate capacitor the conductive bulk material in the metal and the semiconductor separated by the depletion region exhibits a capacitance. By replacing the relevant terms in the well known formula for the capacitance of the plate capacitor

$$C = A \frac{\epsilon}{z} \quad (1.11)$$

with A now referring to the gate area, $\epsilon = \epsilon_0 \epsilon_r$ the total permittivity of the semiconductor and $z = z_d$ the depletion region width one obtains [88]

$$C_{Schottky}(V) = A \cdot \sqrt{\frac{\epsilon_0 \epsilon_r q N_D}{2(V_{bi} - V)}}. \quad (1.12)$$

Deviations from these idealized CV characteristics can be used to obtain information about a sample's structure and electronic effects that influence the charge distribution in the depletion region, see e.g. Paper 3.

1.3 Defect states

Defect states are electronic states that exist inside the otherwise forbidden band gap of a semiconductor. Such states can be realized e.g. by crystal defects like impurities [98], vacancies [99] or the electronic states of SAQDs [30]. The interaction of a defect state situated at an arbitrary energy E_T between the conduction band edge E_C and the valence band edge E_V can happen in four ways, see figure 1.5.

Any defect state can capture/emit electrons from/into the conduction band and/or capture/emit holes from/into the valence band. The dynamics of each process are defined by a charge transfer rate, c for capture processes and r for emission (release). The subscripts correspond to electrons (n) or holes (p), respectively. It should be noted that each process changes the charge state of a defect state and thus causes a change in the overall charge distribution of the system, which can be used to investigate these dynamics electronically, see section 1.6.

Depending on the energetic position of the defect state within the band gap and the free carrier densities in the conduction (n) and valence band (p) one or more of the interactions shown in figure 1.5 can be neglected: In n-doped semiconductors where

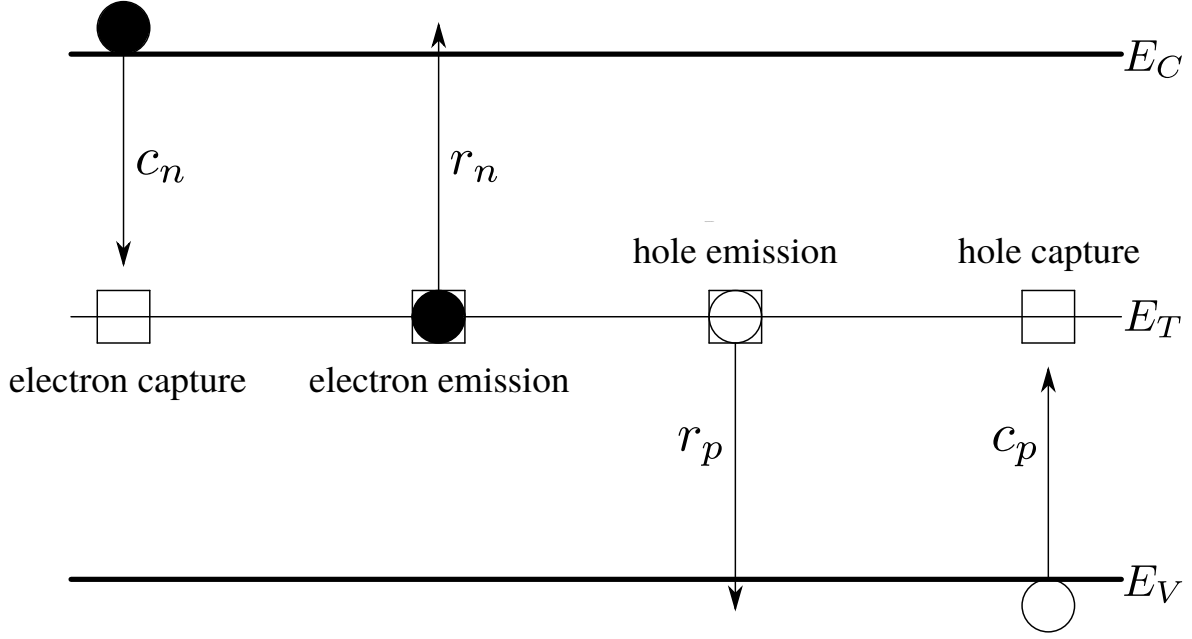


Figure 1.5: Interaction between defect states (empty squares) with electrons (filled circles) in the conduction band and holes (empty circles) in the valence band. Adapted from Ref. [100].

$n \gg p$ the interaction with holes is generally negligible, while the opposite assumption holds for p-doped structures [100]. Such defect states that interact only with one type of carriers are commonly called a *trap*.

The SAQD-structure investigated in this thesis is an n-type Schottky diode, hence in the following all interactions between the SAQD states and holes are neglected.

1.4 Carrier dynamics

Given the sample layout, the discussion of the carrier dynamics associated with the SAQD states in this section will be limited to the interaction with electrons from the conduction band and the subscript n will be omitted. The corresponding expressions for holes require only trivial variations. Furthermore, it is assumed that the defect states are highly localized inside the SAQD plane at a sharply defined distance from the Schottky gate.

1.4.1 Pure thermal activation

Under the assumption of thermal equilibrium the electron capture rate c can be written

$$c = \frac{n \langle v \rangle}{g} \sigma \quad (1.13)$$

where $\langle v \rangle$ is the mean thermal velocity of electrons passing the defect state, n is the local electron density in the conduction band at the position of the SAQD layer, σ the constant capture cross section that is to be determined experimentally and g a degeneracy factor.

Under the assumption of thermal equilibrium throughout the sample, the electron density n can be expressed via the effective density of states in the conduction band N_C where

$$n = N_C \cdot \exp\left(-\frac{E_C - E_F}{k_B T}\right) \quad (1.14)$$

and from the principle of detailed balance the corresponding emission rate r can be obtained [101] as a function of the temperature T

$$r = \frac{N_C \langle v \rangle \sigma}{g} \cdot \exp\left(-\frac{E_C - E_T}{k_B T}\right) \quad (1.15)$$

where k_B is Boltzmann's constant.

By inserting the definitions for the product $N_C \langle v \rangle$ and defining the binding energy $E_b = E_C - E_T$ of a trap state equation (1.15) can be rewritten as [86]

$$\ln\left(\frac{T^2}{r}\right) = \frac{E_b}{k_B} \cdot \frac{1}{T} - \ln\left(\sigma \cdot g \sqrt{3} (2\pi)^{3/2} k_B^2 m^* h^{-3}\right) \quad (1.16)$$

where m^* is the effective electron mass in the semiconductor host material. This emission path is depicted by the third arrow from the top bottom in figure 1.6. When measured pairs of r and T are plotted according to equation (1.16) as a function of $1/T$ the binding energy E_b and the capture cross section σ can be extracted from the slope and the y -axis intercept, respectively. The precise measurement scheme to obtain such data will be explained in section 3.1. Such a procedure is well known as an Arrhenius analysis [102] and is extensively used to determine trap signatures of various defects in semiconductor structures [98].

There are, however, multiple effects that invalidate essential assumptions made to obtain equations (1.13) and (1.15). Those relevant to the results presented in this thesis will be discussed in the following sections.

1.4.2 Electric field effects

Vincent et al. [103, 104] have given expressions for the emission rate of electrons from defect states that are subjected to a non-negligible electric field F . Depending on the relative importance of the thermal activation rate and tunneling emission through an approximately triangular barrier caused by the electric field the emission characteristics can be categorized into one of three regimes: pure tunneling, thermally assisted tunneling and pure thermal activation. In addition, the Poole-Frenkel effect [105, 106] causes a lowering of the confining potential barrier. Figure 1.6 shows the emission paths described in the aforementioned works and the expressions that are relevant for the results presented in this thesis are reproduced in the following sections.

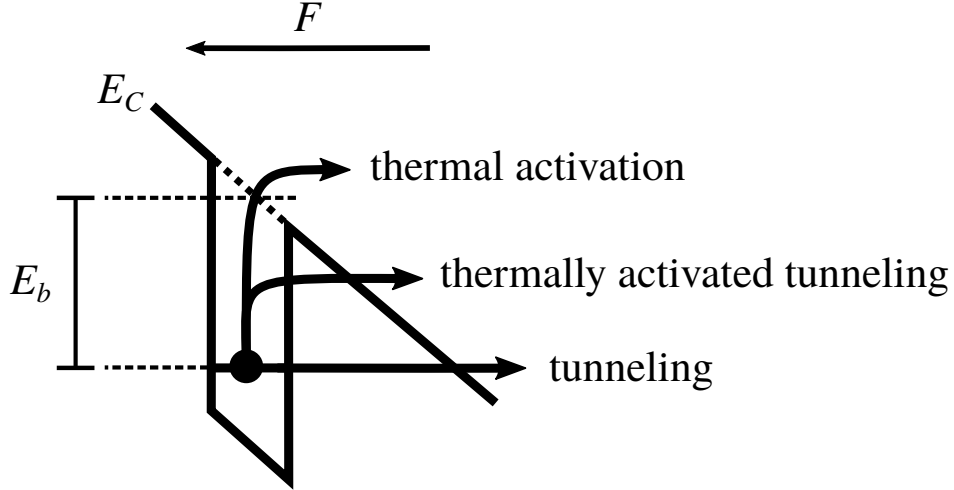


Figure 1.6: Emission paths under the influence of an electric field F , adapted from Ref. [107].

Poole-Frenkel effect

The binding energy of a confined state is lowered when the confining potential is tilted due to the influence of an electric field F , causing an increased thermal emission rate. This effect is known as the *Poole-Frenkel effect* [105]. The emission rate r_{PF} due to the barrier lowering caused by the Poole-Frenkel effect can be calculated for different potential types (e.g. Coulomb [105,108] or square well [109]), both for various dimensionalities [109].

For a three-dimensional Coulomb potential one obtains

$$\frac{r_{PF}}{r} = \frac{1}{\gamma^2} [\exp(\gamma)(\gamma - 1) + 1] + \frac{1}{2} \quad (1.17)$$

where r is the emission rate without consideration of the Poole-Frenkel effect and

$$\gamma = \sqrt{\frac{qF}{\pi\epsilon_r\epsilon_0}} \cdot \frac{q}{k_B T}. \quad (1.18)$$

A similar expression for the square well potential relates the emission rate increase to the geometry of a defect state [109], which in case of the SAQD sample studied in this thesis allows for the extraction of the SAQD height from the emission rate measurements. The application of this model and the discussion of its validity can be found in section 3 of Paper 1.

Pure tunneling

Direct tunneling between the defect state and the free states in the conduction band with the same energy can be assumed to be the dominant emission process at low temperatures where thermal activation is negligible and/or high electric fields where the barrier width becomes small. This process is depicted by the first arrow from the

top bottom in figure 1.6. Paper 1 discusses in detail the transition from tunneling dominated to thermally dominated emission as the temperature is increased. The pure tunneling emission rate $r_{tun.}$ is independent of the temperature and given by [104]

$$r_{tun.} = \frac{qF}{4\sqrt{2m^*E_b}} \exp\left(-\frac{4}{3} \frac{\sqrt{2m^*E_b}^{3/2}}{q\hbar F}\right) \quad (1.19)$$

with the binding energy E_b being the only parameter via which the properties of the defect state enter. By externally varying the electric field strength F and measuring the emission rate at low temperatures it is thus possible to directly obtain the binding energy. Paper 1 and Paper 3 make use of this technique.

Thermally activated tunneling

Thermally activated tunneling occurs when electrons can be thermally excited from a defect state into conduction band states that leak through a sufficiently thin confinement barrier into the potential well. Such a process is depicted by the second arrow from the top bottom in figure 1.6. Since the density of states in the conduction band is continuous, the tunneling density of states leaking into the potential well is continuous as well and the total thermally activated tunneling emission rate has to be obtained by integrating over all energies between the defect state and the conduction band edge. Vincent et al. [104] showed that these processes can be described by a correction factor $r_{Vin.}/r$ to the pure thermal emission rate r (equation (1.15)), often referred to as the *Vincent factor*

$$\frac{r_{Vin.}}{r} = 1 + \int_0^{E_b} (k_B T)^{-1} \exp\left(\frac{E}{k_B T} - \frac{4\sqrt{2m^*E}^{3/2}}{3q\hbar F}\right) dE \quad (1.20)$$

which has to be calculated numerically, although analytical approximations exist for defined cases [104]. In all results presented in this thesis equation (1.20) has been solved numerically.

1.4.3 Leakage currents

The presence of leakage currents flowing through the sample during capture/emission rate measurements increases the number of free charge carriers available for capturing into a defect state [110]. Thus, equating the electron concentration n in equation (1.13) with the equilibrium density of free electrons in the conduction band (equation (1.14)) underestimates the actual carrier concentration. This underestimation has been directly measured for the first time and discussed in section 3 of Paper 2, although the source of the electrons could not be determined unambiguously. Thermally activated leakage currents have also been reported [111, 112] to affect measurement schemes like DLTS (see section 3.1) which rely on the validity of the assumption that equation (1.15) correctly models both the magnitude and temperature dependence of the emission rate. Since even the reverse bias current of a perfect Schottky diode shows a thermally

activated behavior with the activation energy Φ_B (see equation (1.9)) an influence of leakage currents is difficult to exclude.

1.5 Charge transients

Charge transients are caused by non-steady-state charge occupancies of defect states that approach their steady-state. The steady-state charge occupancy of a defect state can generally be obtained from the solution of a system of coupled differential equations describing the occupation probability of each possible charge state. For simplicity this section will be limited to the discussion of the simplest defect state that can either be charged with one electron or be neutral. The transition between the two possible charge states takes place with the rates c for charging and r for discharging. The corresponding system of differential equations is

$$\frac{d}{dt}w_0 = +r \cdot w_1 - c \cdot w_0 \quad (1.21)$$

$$\frac{d}{dt}w_1 = -r \cdot w_1 + c \cdot w_0 \quad (1.22)$$

with $w_{0,1}(t)$ representing the probabilities of finding a defect state charged with 0 or 1 electron, respectively and $w_0 + w_1 = 1$ at all times. Solving equations (1.21) and (1.22) for the general initial conditions $w_1(0) = W$ and $w_0(0) = 1 - W$ one obtains

$$w_0(t) = \frac{r}{r+c} - \frac{W(r+c) - c}{r+c} \cdot \exp(-t(r+c)) \quad (1.23)$$

$$w_1(t) = \frac{c}{r+c} + \frac{W(r+c) - c}{r+c} \cdot \exp(-t(r+c)) \quad (1.24)$$

and it immediately becomes clear that the steady state occupancies are given by

$$w_0(t \rightarrow \infty) = \frac{r}{r+c} \quad (1.25)$$

$$w_1(t \rightarrow \infty) = \frac{c}{r+c} . \quad (1.26)$$

Furthermore it can be seen that unless the initial condition equals the steady state configuration $W = c/(r+c)$ the system will undergo a transition towards the steady state via a *charge transient* in the form of an exponential decay with one single observable charge transfer rate $r_{obs.} = r+c$.

It should be noted that the dynamics of the system, i.e. the observable charge transfer rate does not depend on the initial condition but solely on the individual transfer rates c and r , whereas the amplitude of the transient depends on both. This general behavior also holds true for more complicated systems with more than two charge states

and is well known from the study of the dynamics of chemical multi-step reactions, the mathematical treatment of which is identical [113]. An analytical discussion of a system with three charge states is given in Paper 2 and a system with four charge states is discussed and solved numerically in Paper 3. From these discussions it could be observed that for a system with N_{cs} charge states the solutions w_i are each sums of $N_{cs} - 1$ exponential decays with $N_{cs} - 1$ different observable charge transfer rates $r_{obs.,j}$.

A non-steady-state charge occupancy can be created by exploiting the dependencies of equations (1.13) and (1.15) on external parameters, particularly the applied bias voltage. In a Schottky structure the applied bias voltage strongly affects the free electron density n and the electric field F . Suppose a preparation bias voltage V_p is applied for a sufficiently long time t_p and then abruptly changed to a measurement bias voltage V_m at $t = 0$. If the transition time is small compared to the observable charge transfer time constant for applied bias voltages in the interval $V \in [V_p, V_m]$, the system will be in a non-steady-state at V_m . The resulting charge transient can be used to investigate the properties of the system under $V = V_m$.

For the simple model described via equations (1.23) and (1.24) the charge transient can be written as

$$\rho(t) = -qn_T \cdot [0 \cdot w_0(t) + 1 \cdot w_1(t)] \quad (1.27)$$

with the elementary charge q and the density of defect states n_T . For the SAQDs studied in this thesis n_T can be identified with the area density of the quantum dots in the SAQD layer such that $\rho(t)$ becomes a sheet charge density.

Since the dynamics of the transient are independent of the initial conditions once $V = V_m$ is reached, it is independent of the choice of V_p . The amplitude of the transient on the other hand depends on the initial conditions and thus both on the choice of V_p and the exact time dependence of the bias voltage transition from V_p to V_m .

1.6 Capacitance transients

Capacitance transients are the experimentally accessible manifestation of charge transients inside the active region of a rectifying electronic contact, like a Schottky junction and have first been used to study defects in semiconductors by Williams in 1966 [114]. The introduction of *Deep Level Transient Spectroscopy* (DLTS) by Lang in 1974 [29] further established capacitance transients as one of the main methods to study defect properties [101].

Qualitatively a capacitance transient is caused by the additional time dependent charge inside the depletion region of the Schottky diode. This charge causes the depletion region width to change (and with it the junction capacitance according to equation (1.12)). For n-type Schottky diodes like the structure studied in this thesis the additional negative charges inside the depletion region require more positive ionized donor atoms, and thus a larger depletion region width, to obtain overall charge neutrality together with the negative charges on the narrow metal side of the depletion region.

Thus, with an increased negative charge density in the defect states, the capacitance decreases, and vice versa.

Quantitatively the exact relationship between the charge density in defect states and the measured capacitance is often derived assuming that the defect states are homogeneously distributed throughout the depletion region [114] or given in differential form to obtain arbitrary concentration profiles from the measured data [101].

Schulz has shown [86] that for a layer of SAQDs with the corresponding electronic states modeled via a delta-like layer of defect states at a distance z_Q from the Schottky gate the total junction capacitance can be written as

$$C(V,t) = \epsilon_r \epsilon_0 A \sqrt{\frac{qN_D}{2(\epsilon_r \epsilon_0 (V_{bi} - V) - \rho(t)z_Q)}} \quad (1.28)$$

with the SAQD sheet charge density $\rho(t)$.

For $\rho(t) \ll \epsilon_r \epsilon_0 (V_{bi} - V)/z_Q$ equation (1.28) can be linearized to

$$C(V,t) \approx C_{Schottky}(V) \cdot \left(1 + \frac{\rho(t)z_Q}{2\epsilon_r \epsilon_0 (V_{bi} - V)}\right) \quad (1.29)$$

with $C_{Schottky}(V)$ given by equation (1.12). For the sample studied in this thesis this approximation is valid for low bias voltages or low occupancies but might not be valid at high bias voltages and high amounts of charge in the SAQDs. When the approximation is valid the measured capacitance transients dynamic can directly be evaluated as if it were the underlying charge transient.

Chapter 2

Experimental techniques

2.1 Sample structure

The sample studied in this thesis is an n-type GaAs Schottky diode with a single embedded SAQD layer at $z_{QD} = 413\text{ nm}$ distance from the surface. The sample was grown using Molecular Beam Epitaxy [73] by Sven Scholz from the group of Prof. A. D. Wieck from the Lehrstuhl für Angewandte Festkörperphysik at the Ruhr-Universität Bochum as sample #14691. The different layers are shown in figure 2.1 (Top) and their function will be explained in the following paragraphs. The growth sheet as provided by the group of Prof. Wieck is included at the end of the thesis.

Starting with an un-doped GaAs single crystal 100 nm of un-doped GaAs are grown, followed by 100 nm containing 20 periods of a GaAs/AlAs super-lattice to on the one hand increase the smoothness of the surface and on the other hand hold off impurities that might diffuse from the bulk material into the active regions. The super-lattice is capped with 50 nm of un-doped GaAs on top of which the active sample region is grown.

A layer of 300 nm degenerately Si-doped GaAs acts as the back contact of the Schottky diode. The targeted doping density during the growth of this layer was $N_{D,2} = 2 \times 10^{18}\text{ cm}^{-3}$. Due to this high doping density this layer acts as a quasi-metallic electron reservoir.

The semiconductor part of the Schottky diode is formed in part by the following 500 nm of weakly Si-doped GaAs. The targeted doping density during the growth of this layer was $N_{D,1} = 2 \times 10^{16}\text{ cm}^{-3}$, a C^{-2} analysis [88] however revealed a net doping density of $N_{D,1} = 6 \times 10^{15}\text{ cm}^{-3}$.

The InAs-SAQD layer is grown on top of 10 nm of un-doped GaAs in the Stranski-Krastanov mode, see section 1.1.1. From AFM-scans over similarly grown un-capped SAQDs it is known that the resulting quantum dots have a sheet density of $n_{QD} \approx 10^{14}\text{ m}^{-2}$, a circular base with a diameter of approximately 30 nm and a height of $\approx 7\text{ nm}$. The SAQD layer is capped with 13 nm of un-doped GaAs to provide a smooth surface for the subsequent layer.

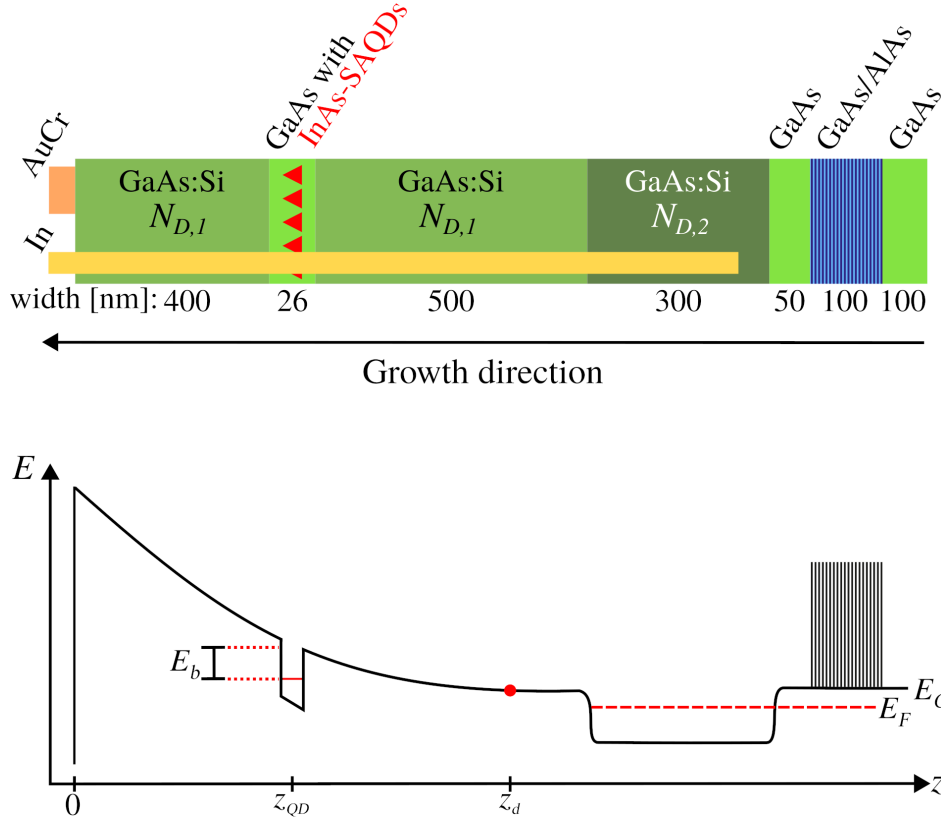


Figure 2.1: Top: Layer structure of the sample studied in this thesis. The SAQDs are represented by the red triangles. Bottom: Sketch of the band diagram on the same scale for negative applied bias voltages.

The final layer consists of 400 nm of weakly Si-doped GaAs grown with the same parameters as the previous doped layer. It completes the n-type semiconductor of the Schottky structure.

The wafer is then cut into pieces of $\approx 5 \text{ mm} \times 5 \text{ mm}$. Optical lithography and metalization are used to define 12 square AuCr gates (edge length $300 \mu\text{m}$ each) on top of the sample that act as the metal part of the Schottky structure. Only one is used in the measurements, the others serve as back-up. Four indium contacts are alloyed into the structure, one at each of the corners of the sample, to form an ohmic contact that connects the degenerately doped back contact layer to the surface. Again, only one is used during a measurement with the others serving as spare contacts. The In and AuCr electrodes were processed by Charlotte Rothfuchs-Engels, at that time also part of the group of Prof. A. D. Wieck.

Figure 2.1 (bottom) shows a sketch of the band diagram on the same scale as the layer structure on top for negative applied bias voltages. For applied voltages $V < 0 \text{ V}$ the end of the depletion region z_d lies within the 500 nm wide layer.

The sample is glued into a chip carrier using polymethylmethacrylate (PMMA) and one AuCr and one In contact are connected to the pads of the chip carrier using gold bond wires (bonded onto the AuCr gate and glued using silver epoxy onto the In contact).

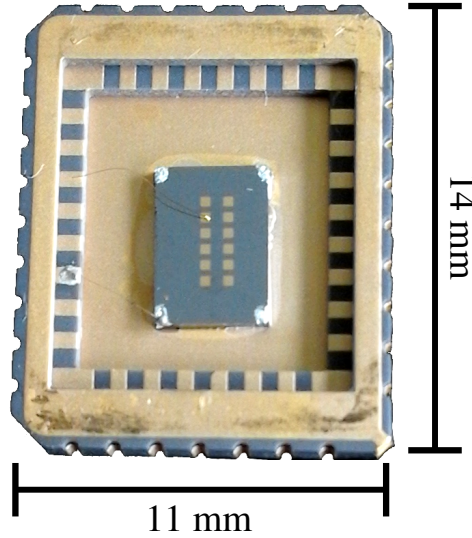


Figure 2.2: Photo of the sample glued into the chip carrier with connected electrodes.

Figure 2.2 shows the sample glued into the chip carrier with connected electrodes. This way it can be easily moved between different setups suitable for measurements in different temperature intervals.

2.2 Cryogenic setup

The results presented in this thesis required measurements at constant temperatures for a long period of time or during temperature sweeps. Temperatures established in the measurements range from $T = 3\text{ K}$ up to $T = 100\text{ K}$. The relevant details of the cryogenic setup will be discussed in the following sections.

2.2.1 Liquid nitrogen dewar

For measurements at $T = 77\text{ K}$ the sample was inserted into either a 100 L or 120 L liquid nitrogen dewar, depending on availability, that is grounded via a braided copper strip. The dewar is metallic and acts as a Faraday cage. It has two openings at the top to allow evaporating nitrogen to escape and one where the sample is inserted. The ventilation openings are angled and partly blocked by several metal disks with small openings, each of which is rotated with respect to the next one to block stray light to enter the inside of the dewar. Additionally the outlet is covered with black cloth.

The chip carrier containing the sample is inserted into a socket that is mounted on a metal rod such that it can be inserted approximately 80 cm below the liquid nitrogen surface. A Pt1000 temperature sensor is positioned directly besides the socket and connected in a four wire resistance measurement setup. The anode and cathode of the sample are connected from the socket onwards via $50\ \Omega$ impedance coax cables. With this setup long time measurements can be conducted with a high temperature

stability. Depending on outside temperatures measurements can be conducted for up to two weeks with no measurable temperature increase at the sample.

2.2.2 Dilution refrigerator

To achieve temperatures below and above $T = 77$ K a dilution refrigerator [115] from *Leiden Cryogenics* was used that is pre-cooled using a pulse tube cooler [116]. The dilution refrigerator used in this thesis uses He^4 as working fluid in the pulse tube cooler and a mixture of He^3 and He^4 to achieve dilution refrigeration. With the pre-cooling due to the pulse tubes alone temperatures as low as $T = 3$ K could be reached, while the dilution refrigeration can reach a base temperature of 25 mK.

For the measurements presented in this thesis the base temperature of the pulse tube cooling has proven to be sufficiently low and hence the dilution refrigeration was not used.

The sample is mounted inside of the housing of the cryostat and is shielded from outside influences by multiple layers of Faraday shields, vacuum chambers and gold foil to reflect heat radiation. An electric heater is thermally coupled to the interior of the cryostat and can be used to introduce a heating power such that the temperature can be stabilized above the base temperature. It takes approximately one day from the beginning of the heating to the stabilization of the temperature, which is monitored by a model *CX-1010 Cernox* temperature sensor from *LakeShore Cryotronics* that was calibrated from $T = 1.4$ K to $T = 325$ K. The sensor is connected in a four wire resistance measurement setup. The sample is mounted in a socket which is connected via $50\ \Omega$ impedance coax cables to a vacuum feed-through.

The pulse tube cooler is driven by a compressor that can be switched on and off from a computer to realize pre-programmed temperature sweeps. If the cryostat is warmed up from the pulse tube's base temperature of $T = 3$ K by turning off the compressor and without using the electric heater the time to reach $T \approx 100$ K can be up to two days, depending on the vacuum quality in the insulation and the thermal mass inside the cryostat. This allows for slow measurements during temperature sweeps in the interval of interest.

2.3 Bias pulses

The bias pulses were generated using an arbitrary waveform generator (AWG) built into the oscilloscope used to capture the capacitance transients, see section 2.5 for the results presented in Paper 1, and in later measurements (Papers 2+3) by a separate Keithley model 3390 AWG which offers an increased output voltage range and better resolution.

In both cases the duty cycle, frequency as well as the HIGH and LOW values of the pulses can be controlled remotely. The output of the AWGs was fed into an external voltage input of the lock-in amplifier used to measure the capacitance where it is added to the AC test signal generated by the lock-in, see section 2.4. Additionally

the signal was connected to a second input of the oscilloscope used to capture the capacitance transients such that the applied bias pulses could be recorded as well. This was done to ensure that possible drifts in the constant parts of the voltage pulses or ringing/overshooting of the AWGs did not cause effects on the samples Schottky capacitance (see equation (1.12)) that could be misinterpreted as transient capacitance due to charge rearrangements in the sample.

To trigger the oscilloscope recording the transients the Keithley 3390 offers a synchronization output with TTL logic levels independent of the actual pulse amplitudes, whereas for the oscilloscope's AWG the trigger level had to be adjusted every time the pulse voltages changed.

For transient measurements that require a high signal to noise ratio it has proven beneficial to choose the bias pulse frequency such that subsequently recorded transients start at an alternating phase difference of $\Delta\varphi = 0 + \varphi_0$ and $\Delta\varphi = \pi + \varphi_0$ with respect to the 50 Hz power line cycle, where φ_0 is an arbitrary constant initial phase difference. This way possible electrostatic or magnetic influences get averaged out of the recorded transients faster. A choice of the pulse parameters to achieve this is usually possible without deviating too much from the optimal settings for a specific measurement.

2.4 Capacitance measurements

The capacitance of the sample was measured using a HF2LI lock-in amplifier and a HF2TA transimpedance amplifier from *Zurich Instruments*. All devices have been operated in DC-coupling mode to avoid the influence of coupling capacitors in the capacitive signal from the sample. A small AC voltage (typically with $V_{AC} = 10$ mV amplitude and a frequency in the order of $f \approx 10$ MHz) was applied to the anode (AuCr gate) of the sample. This AC voltage can be added to an external voltage input via which the bias pulses are applied, see section 2.3. The cathode was connected to the input of the HF2TA which keeps its input at a virtual ground potential.

Another AC voltage with an adjustable amplitude that is shifted by $\Delta\varphi = \pi$ can be applied to a 100 pF capacitor which is connected to the same input of the HF2TA. Doing so, a capacitive AC current offset can be subtracted from the input such that the measurement devices can be operated in a more sensitive range. The total cable length, via which this capacitor is connected, roughly matches the length of the cables to the sample, such that the additional phase shift that arises due to the runtime of the signals in the cables is matched. When no analog offset subtraction is needed the capacitor is disconnected from the HF2TA.

The resulting AC current was converted into an AC voltage via the relationship $V = ZI$ where the transimpedance Z of the HF2TA can be chosen from 100 V/A to 100 MV/A in factors of 10. Z was chosen to be at most 1 kV/A since higher values cause a bandwidth limitation [117] that is undesirable for fast capacitance measurements. The output of the HF2TA was connected to the voltage input of the HF2LI using 50 Ω impedance coax cables. 50 Ω impedance matching between the HF2TA and the HF2LI causes a decrease of the measured voltages by a factor of 2 which has to be taken into ac-

count when calculating absolute values of the capacitance. A sketch of the capacitance measurement setup is shown in figure 2.3.

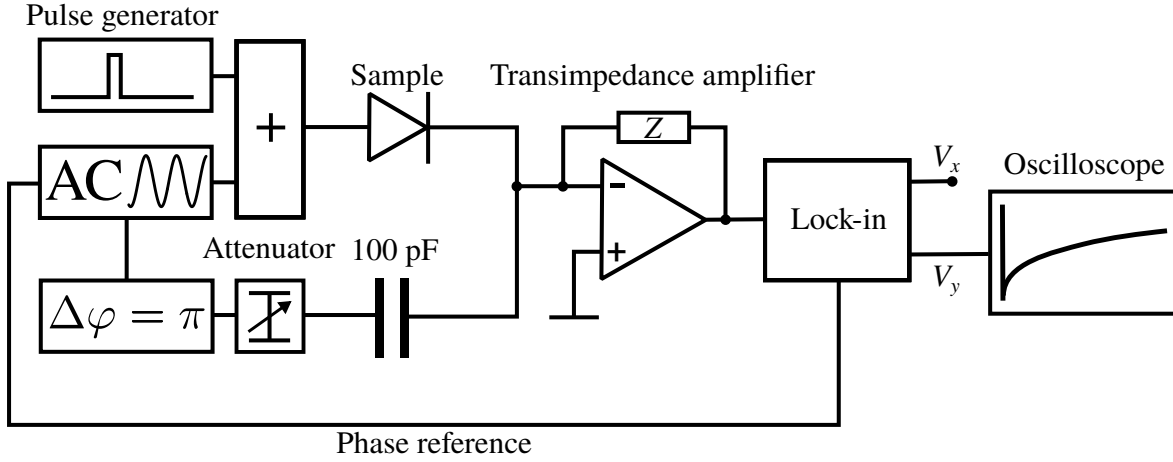


Figure 2.3: Sketch of the capacitance measurement setup used in this thesis.

The signal is then demodulated by the HF2LI and the frequency component of interest in the input signal is separated into an in-phase (V_x) and out-of-phase (V_y) component. The phase shift that arises from the runtime of the signals in through the cables can be compensated by digitally offsetting the reference phase of the demodulator. The bandwidth of the demodulator can be controlled digitally and governs the time resolution in the output signal. For transient measurements the bandwidth was chosen large enough to ensure that the output signal has reached 99 % of its settling value after one time sampling interval of the transient has passed [117]. To reduce the poor signal to noise ratio that comes with high-bandwidth measurements the repetitive transients can be averaged until the signal to noise ratio is acceptable.

By using complex circuit analysis it is easy to show that the capacitance of the sample is directly proportional to the out-of-phase component of the AC current with respect to the applied AC voltage (and with it the demodulated voltage V_y) via the relationship

$$C = \frac{I_y}{2\pi f V_{AC}} \quad (2.1)$$

which is applicable as long as the sample can be represented by a parallel circuit of a capacitor and a resistor. This approach has proven itself to be justified for the sample studied here.

The demodulated out-of-phase component V_y of the input voltage of the HF2LI can be read out digitally from a computer, however, while this method works well for slow readouts (e.g. for a CV trace) the data transfer rate has shown to be too slow to record capacitance transients with the desired time resolution. Instead the HF2LI can output an analogue signal sufficiently fast that is proportional to the demodulator outputs. This signal is then captured using an oscilloscope, see section 2.5.

2.5 Transient recording

For fast recording of the measured capacitance transients the analogue output of the lock-in amplifier was recorded using either a PicoScope 5244B or 5444B digital oscilloscope from *Pico Technology*, depending on the availability, with a hardware voltage resolution of 15 bits. These two models differ only in the number of input channels (2 for the 5244B and 4 for the 5444B). In any case both the output of the lock-in and the applied bias pulse were recorded with a time resolution that matches the bandwidth setting of the demodulator.

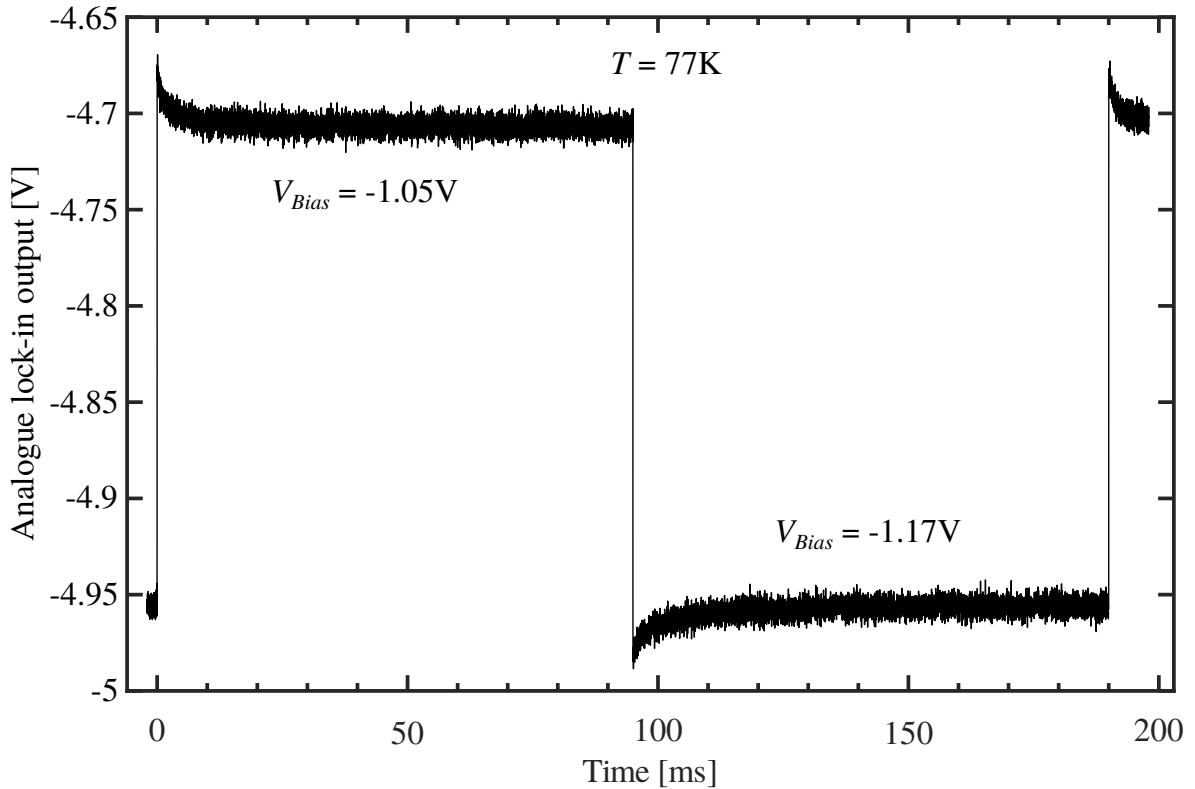


Figure 2.4: Raw data from the analogue output of the lock-in amplifier as measured with the oscilloscope at $T = 77$ K. The data shown here consist of 20,000 time samples and represent the average of 500 identical voltage pulses. This measurement corresponds to two pixels in figure 3(a) of Paper 2.

Figure 2.4 shows a representative transient measurement at $T = 77$ K obtained for analysis using the lock-in DLTS technique, see section 3.1. This method does not require very high signal to noise ratios and thus the transient measurement can be sped up by restricting the number of averages. Typical data that were averaged excessively to obtain a high signal to noise ratio is shown in figure 1(c) of Paper 1.

The oscilloscopes are controlled by a computer and store the acquired data in an internal buffer that is transferred to a PC after one waveform is recorded. It has proven beneficial to the latency of the data acquirement process to run the software controlling the oscilloscope (PicoScope 6 [118]) on a separate PC, where the raw recorded transient data was also stored.

A software was written that listens on the RS232 port for commands from the main laboratory computer that controls the entire measurement setup (see section 2.6). It sets the parameters of the PicoScope 6 program controlling the oscilloscope via an inter process communication interface provided by *Pico Technology* accordingly. Once a waveform measurement is completed this is also signalized via the RS232 connection.

The PicoScope 6 control program can be configured to capture multiple waveforms subsequently, average them in the PC's RAM memory and only save the averaged traces to the hard disk. This feature was always used to save memory on the disk, especially when many transients (up to 10^6) need to be averaged to obtain a high signal to noise ratio. Due to RAM limitations the practical number of transients averaged in this way is ≈ 1000 or less. Each set of 1000 transients was thus averaged and then only the average was saved to a file. Subsequent files are indexed by an integer appended to the file name and after the measurement is completed the individual files can be averaged as well to obtain the final transient. In measurements where parameters like the temperature or the pulse configuration were changed between transient recordings, this principle stayed the same. Typical measurements require a disk space of approximately 5 GB. All transient data measured with by the oscilloscope PC is saved directly onto an external 4 TB hard drive to save time consuming file transfers when a measurement has finished. The main computer controlling the lab equipment synchronizes the change in parameters with the recording of the transients, see section 2.6.

2.6 Device synchronization

To synchronize the individual devices in the laboratory a program was written that can control devices connected to the computer and operate them according to a main script. The individual devices are in turn controlled by driver scripts that handle the abstraction from the raw communication protocol that differs from device to device and the exposed abstract driver functions that read/set values or change the parameters of an instrument. The main program itself can communicate with devices that are connected via either:

- an RS232 connection (e.g. the multimeter that read out the temperature sensors or the compressor)
- TCP/IP (the lock-in amplifier)
- the USB-TMC protocol (the bias pulse generator)
- GPIB
- I²C

and anything that provides a C-compatible control library.

After setting the bias pulse configuration and the heating/cooling power a typical measurement script for temperature sweeps takes care of these steps:

- read out the temperature sensors,
 - start the capture of a set of transients that are meant to be averaged together
-

and if multiple sweeps are planned once a certain temperature is reached:

- adjust the heating/cooling power to return to the starting temperature,
- setting the new bias pulse configuration,
- and start a new measurement.

For isothermal measurements the program only monitors the temperature sensors to issue an alarm per email if the deviation gets too large, e.g. due to too much liquid nitrogen having evaporated from the dewar or the cooling water supply cooling the compressor has failed.

In this way measurements that require lots of parameter scans and/or a lot of averaging can be carried out automatically over a course of weeks without requiring permanent supervision. All steps of the measurement process are logged and saved alongside the actual measurement data for future reference.

Figure 2.5 shows a sketch of the minimum setup in the laboratory required for the measurements presented in this thesis. The helium compressor is not used when measuring in the N₂ dewar. Not shown are the vacuum pumps and the heater for the cryostat.

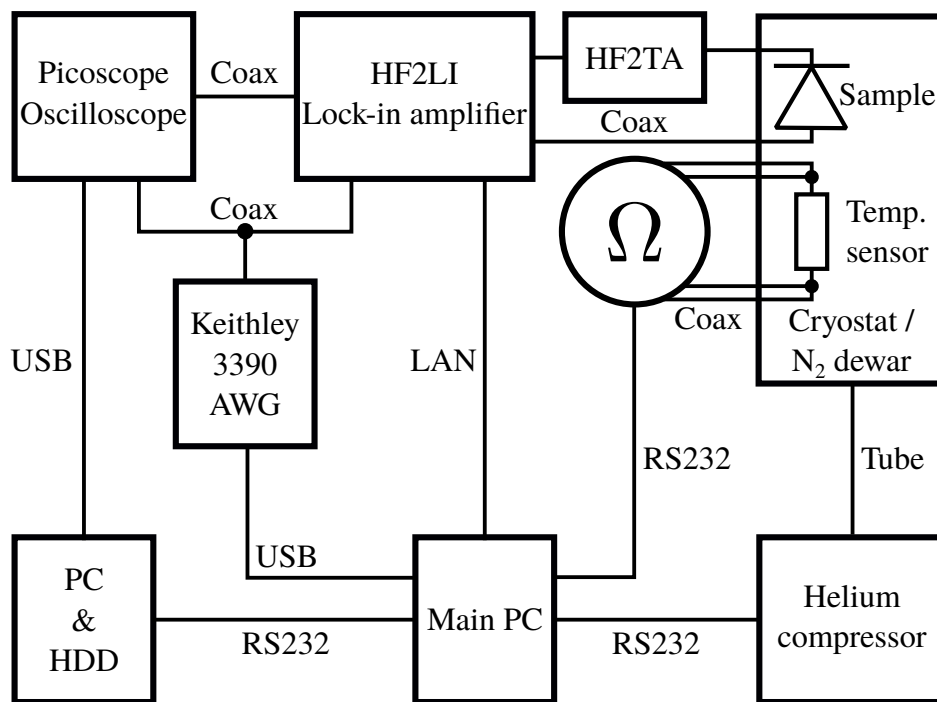


Figure 2.5: Sketch of the minimum measurement setup for the results presented in this thesis. The helium compressor is not used when measuring in the N₂ dewar. Not shown are the vacuum pumps and the heater for the cryostat.

Chapter 3

Data analysis techniques

3.1 Deep Level Transient Spectroscopy

Deep Level Transient Spectroscopy (DLTS) has been introduced by D. Lang in 1974 [29] and has since become a standard technique in the study of defects in semiconductors, see e.g. Refs. [98,101,119]. The original working principle of DLTS is to analyze a set of capacitance transients related to emission processes recorded at different temperatures T and to calculate the magnitude of a specific filter signal $S(T)$ defined by a *weighting function* $w(t)$ for each transient

$$S(T) = \int_0^{\infty} C(t,T) w(t) dt \quad (3.1)$$

where $C(t,T)$ are the sets of the recorded capacitance transients. By finding the temperature where the signal calculated using the weighting function is maximized it is possible to obtain one pair of values of the relationship $\tau(T)$. At the maximum of the signal the dominant apparent lifetime τ in the transients matches the reference value τ_{max} (commonly referred to as the *rate window*), which is defined by the chosen weighting function. Changing the parameters of the weighting function such that τ_{max} is changed and repeating the steps mentioned before more data points of the relationship $\tau(T)$ can be obtained and then be compared to a model. In the original proposal of DLTS this was the simple thermally activated carrier emission described by equation (1.16), but later works have extended the technique to more sophisticated models, e.g. Refs. [104,110]. It should also be noted that, while the original DLTS technique relied on a variation of the temperature, the underlying data analysis methods can be applied to transient measurements where other parameters have been varied as well, most notably the applied bias voltage during [43] and/or before the transient measurement (see Paper 2), thus replacing the T -dependence in equation (3.1) with the respective voltage V_m and/or V_p . There are many possible choices for the weighting function $w(t)$ [101]. The originally proposed *Boxcar* and the *Lock-in* weighting function that was used in this thesis will be briefly introduced in the following sections based on Refs. [29,101] and [120].

3.1.1 Boxcar DLTS

The *Boxcar* method originally proposed by Lang [29] exclusively makes use of two data points of each capacitance transient to calculate $S(T)$. The weighting function in this case is given by

$$w(t) = \delta(t_1 - t) - \delta(t_2 - t) \quad (3.2)$$

with Dirac's Delta Distribution $\delta(t)$.

The effect of the weighting function is illustrated in figure 3.1.

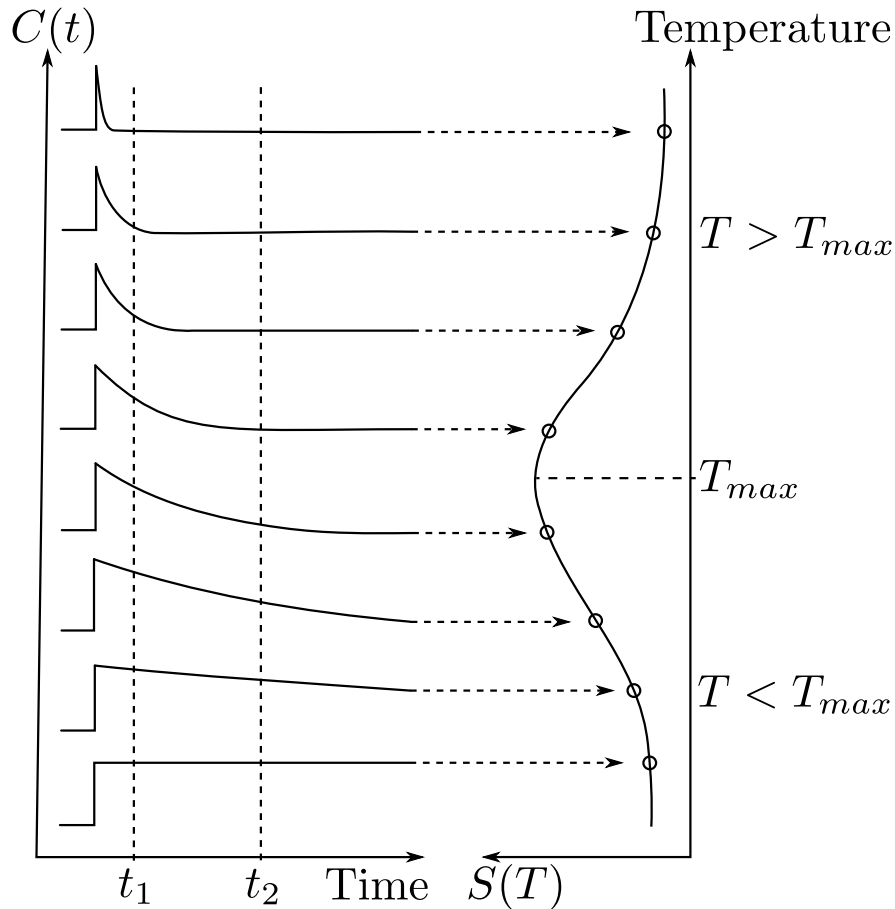


Figure 3.1: Temperature dependence of the Boxcar signal. The DLTS signal $S(T)$ will show a peak at T_{max} where the effective lifetime of a defect state matches the rate window τ_{max} . Adapted from Ref. [29].

The relationship between the parameters of $w(t)$ and the rate window can be derived by taking the derivative of $S(T)$ with respect to τ under the assumption that $C(t, T) = \exp(-t/\tau(T))$ and setting this expression to zero. For the Boxcar weighting function this procedure yields the relationship [29]

$$\tau_{max} = \frac{t_1 - t_2}{\ln(t_1/t_2)} . \quad (3.3)$$

It is obvious that due to the limitation to only two data points per transient the resulting value of $w(t)$ will be strongly influenced by the signal-to-noise ratio of the measurement data.

3.1.2 Lock-in DLTS

Miller et al. also proposed other weighting functions to obtain the dominant time constant of a transient [101]. To improve the signal-to-noise ratio compared to the Boxcar method, the corresponding weighting function has to take more than two measurement points into account. They found that the *lock-in weighting function* provides a good compromise between sensitivity and time constant resolution. It is given by

$$w(t) = \frac{1}{P} \cdot \begin{cases} +1 & 0 \leq t \leq P/2 \\ -1 & P/2 < t \leq P \\ 0 & \text{otherwise} \end{cases} \quad (3.4)$$

with the lock-in period P .

Due to the cables used in the setup which induce resistances, capacitances and inductances an RLC circuit response to the bias pulses can be generated by the setup. Additionally, due to the response of the various measurement devices to the voltage pulses, there might be an initial section of the recorded transients that has to be excluded from the analysis, since it is dominated by that responses rather than the sample's capacitance transient. In order to exclude these effects, an initial time t_d can be gated off from the transient such that the weighting function becomes

$$w(t) = \frac{1}{P - t_d} \cdot \begin{cases} +1 & t_d \leq t \leq P/2 \\ -1 & P/2 < t \leq P \\ 0 & \text{otherwise.} \end{cases} \quad (3.5)$$

For all measurements presented in this thesis however, the response of the measurement setup has been negligible even after the first time sample point in the recorded transients and hence $t_d = 0$ for all results presented here.

Numerically the lock-in DLTS signal can thus be approximated by

$$S(T) = \frac{1}{N_t} \left(\sum_{i=1}^{N_t/2} C(t_i, T) - \sum_{i=N_t/2+1}^{N_t} C(t_i, T) \right) \quad (3.6)$$

with $t_{N_t} = P$.

The DLTS signal $S(T)$ obtained by using the lock-in weighting function is qualitatively similar to the one obtained from the Boxcar method, but since all data points of the transients are taken into account the signal-to-noise ratio is improved. This allows for shorter measurement times since the transients themselves do not need to be averaged as much to yield a clear DLTS signal. In the case of temperature sweeps the shorter measurement times per transient also increases the temperature resolution. It has to

be noted though that the lock-in DLTS method has a slightly poorer lifetime resolution [86, 101].

In order to obtain the relationship between the parameters t_d and P and the rate window τ_{max} one has to go through the same procedure as for the Boxcar method. However, this yields no analytical solution any more. Day et al. have discussed the dependence of the rate window on the relevant parameters as well as on various phase differences between the signal and the weighting function in detail [120] where they find the approximately linear relationship $\tau_{max} \approx 0.424 \cdot P$ for real time data analysis using a physical lock-in amplifier. The data in this thesis were analyzed after an entire transient has been digitized and the lock-in DLTS signal was calculated numerically from these discrete data points according to equation (3.6). For these conditions the relationship between P and the rate window τ_{max} was calculated numerically and is shown in figure 3.2, where a linear relationship with $\tau_{max} = 0.398 \cdot P$ can be observed that deviates slightly from the result reported by Day et al..

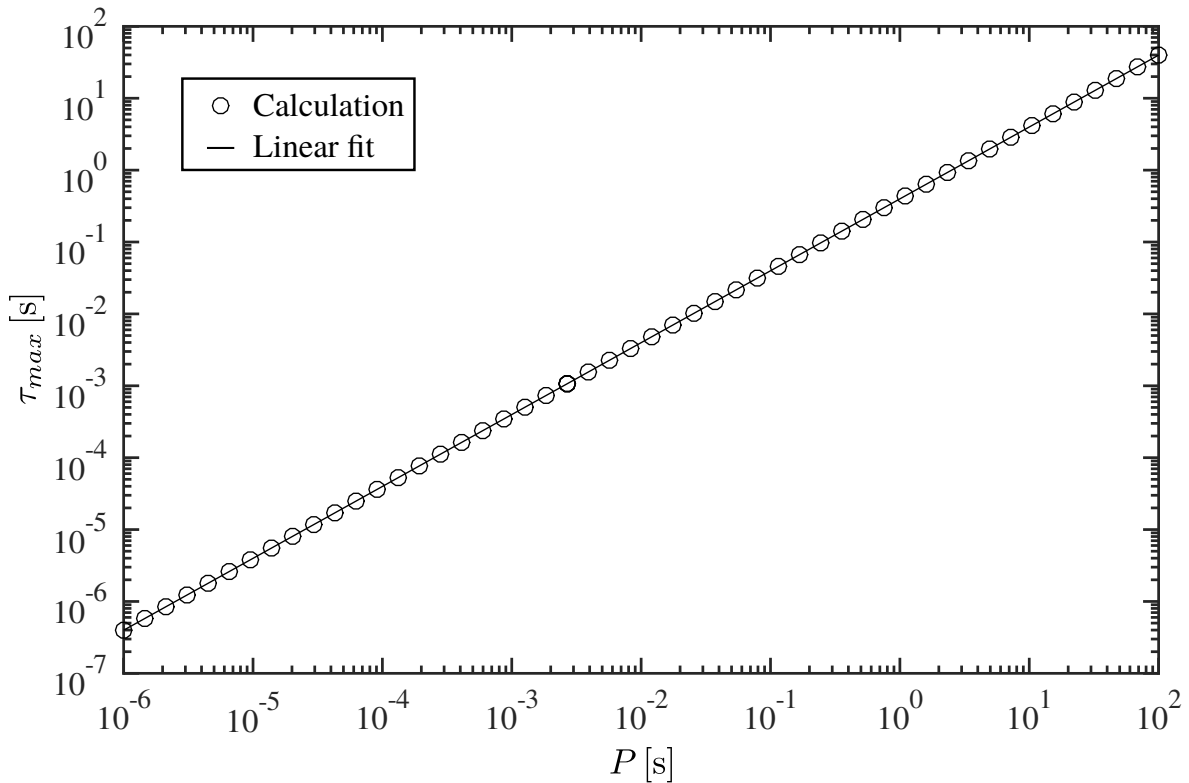


Figure 3.2: Numerically determined relationship between τ_{max} and P according to equation (3.6). The linear fit yields $\tau_{max} = 0.398 \cdot P$.

3.2 Numerical Laplace inversion

A capacitance transient $C(t)$ can be thought of as the Laplace transform of a spectral density function representing a distribution of rates $g(r)$ (or time constants $g(\tau) = g(r^{-1})$)

$$C(t) = \int_0^\infty g(r) \exp(-rt) dr. \quad (3.7)$$

From a measured transient the *inverse Laplace transform* then gives the spectral density function g . This approach is called *Laplace DLTS* (LDLTS) and was originally proposed by Dobaczewski in 1994 [40]. Instead of applying a filter function with a constant rate window to a set of transients with varying dominant time constants, one single transient with a high signal-to-noise ratio is recorded and the inverse Laplace transform is calculated numerically. Theoretically, an inverse Laplace transform of a transient signal which consists of a sum of exponential decays shows a set of delta peaks at the time constants of these decays [121].

The analytical definition of the inverse Laplace transform is given by

$$g(r) = \frac{1}{2\pi i} \int_{\gamma-i\infty}^{\gamma+i\infty} C(t) \exp(+rt) dt, \quad \gamma \in \mathbb{R}. \quad (3.8)$$

Algorithms based on this analytical definition of the inverse Laplace transform usually require the input data to be continuously known in the complex plane (see e.g. Refs. [122–125]), a condition that cannot be met by discrete sampled measurement data [121]. Instead, for discrete real valued input data g has to be obtained by solving equation (3.7). The numerical difficulties originating from the ill-posed nature of this integral equation make it difficult to obtain a Laplace spectrum from measured data, since for these kind of integral equations (first kind Fredholm integral equations [121]) if a solution exists it might not be unique and/or depend continuously on the input data [126]. Even small contributions of generally unavoidable measurement noise in the input data can thus lead to great variations of the solutions and if several solutions are found they might differ to such an extent that a physical interpretation becomes impossible, see e.g. the example by Lanczos [127].

To manage these problems several methods are known, like the Fourier transform based Gardner Transform [128], the Truncated Singular Value Decomposition (TSVD) [126] or the Tikhonov Regularization [129].

In the Laplace inversion code written and used during this thesis the Tikhonov regularization approach was chosen. The details of the numerical Laplace inversion using this method will be explained in the next sections.

3.2.1 Discretization

To solve equation (3.7) numerically it first has to be discretized. The time variable t will be discretized in equidistant time steps with the step size Δt representing the time samples of the measured capacitance signal. Hence, the time scale can be represented as a vector containing all time steps from t_0 to t_{end} given by

$$t \rightarrow \vec{t} = \begin{pmatrix} t_0 \\ t_1 \\ \dots \\ t_{end} \end{pmatrix} \Rightarrow \vec{t}_i = t_0 + i \cdot \Delta t . \quad (3.9)$$

The linear spacing of the time steps is due to the digitizing process in the oscilloscope, which captures the data with a fixed sampling rate.

Due to the expected large variation of the time constants in the measurement data (see e.g. Ref. [36]) the spectral density function g was discretized using logarithmic spacing. With such a spacing the conversion between the forms of g defined as a function of a decay rate r or a time constant τ becomes trivial. In the following g will be defined in terms of the time constant τ . The time constant grid can be represented as a vector containing all life time steps from τ_{min} to $\tau_{max} = \tau_{min} \cdot v^{N_\tau}$

$$\tau \rightarrow \vec{\tau} = \begin{pmatrix} \tau_{min} \cdot v^0 \\ \tau_{min} \cdot v^1 \\ \dots \\ \tau_{min} \cdot v^{N_\tau} \end{pmatrix} \Rightarrow \vec{\tau}_j = \tau_0 \cdot v_\tau^j \quad (3.10)$$

where N_τ denotes the total number of grid points for the τ -axis.

Accordingly the discrete spectral density vector is defined as the continuous function evaluated at the discrete lifetime grid points

$$\vec{g}_j = g(\tau_j) . \quad (3.11)$$

If one defines a transformation matrix $\underline{\underline{A}}$ as

$$\underline{\underline{A}}_{ij} = \exp(-\vec{t}_i / \vec{\tau}_j) \quad (3.12)$$

it is possible to write the discrete Laplace transformation of the spectral density vector \vec{g} as a matrix times vector product

$$\vec{C} = \underline{\underline{A}} \cdot \vec{g} . \quad (3.13)$$

Since the final goal is to numerically obtain the inverse Laplace transform one has to find a \vec{g} such that the measured capacitance transient data stored in the vector \vec{C}_m equals the one calculated from equation (3.13).

With typical measurement parameters the transform matrix $\underline{\underline{A}}$ usually has dimensions in the range of $10,000 \times 300$. It is a dense non-square matrix and cannot be inverted. The naive approach is to find a spectral density vector that minimizes the mean squared deviation

$$f(\vec{g}) = \|\underline{\underline{A}} \cdot \vec{g} - \vec{C}_m\|_2^2 \quad (3.14)$$

of the Laplace transform result compared to the measured data by varying \vec{g} . Here $\|\dots\|_2$ represents the 2-norm of a vector. This is, as discussed above, impractical due to the ill-posed nature of the problem.

3.2.2 Tikhonov regularization

The Tikhonov regularization [129] introduces a second term to the objective function that is to be minimized and thus penalizes unwanted aspects in the solution. The regularized objective function then becomes [126]

$$f_{reg}(\vec{g}) = \|\underline{\underline{A}} \cdot \vec{g} - \vec{C}_m\|_2^2 + \|\alpha \cdot \underline{\underline{D}} \cdot \vec{g}\|_2^2 \quad (3.15)$$

where $\underline{\underline{D}}$ is the *Tikhonov matrix*, the exact choice of which determines what is considered to be unwanted aspects in the solution and α determines the relative weight of the regularization term $\underline{\underline{D}} \cdot \vec{g}$ compared to the Laplace transform term $\underline{\underline{A}} \cdot \vec{g} - \vec{C}_m$. The choice of α is non-trivial yet crucial [126] to obtain neither under- nor over-regularized solutions that exhibit too much non-physical or too little physical information, respectively. Multiple criteria for the proper choice of the regularization parameter exist [126], e.g. the *L-criterion* [130] or the *discrepancy principle* [131]. The approach to determine a reasonable weighting of the regularization used throughout this thesis is explained in detail in the supplement to Paper 1.

Common choices for the Tikhonov matrix $\underline{\underline{D}}$ are the identity matrix, the forward difference operator and the squared forward difference operator [126]. Each choice penalizes different aspects of the spectral density vector \vec{g} :

- The identity matrix penalizes non-zero elements in \vec{g} such that the regularization favors sparse solutions with few time constants
- The forward difference matrix penalizes rapid changes in \vec{g} such that the regularization favors solutions with little detail in \vec{g}
- The squared forward difference matrix penalizes curvature in \vec{g} such that the regularization favors solutions with few peaks

These three choices have been implemented in the code and can be selected via pre-processor definitions. For the difference operators the boundary conditions were set to zero, since it is expected that the solution vector is zero outside of the calculated time constant interval. Test calculations have shown that while for transient data typical for this thesis the forward difference operator preforms the best in terms of convergence speed, the overall effect of the choice of the Tikhonov matrix on the results is not dramatic. It should be noted that due to the regularization and its unawareness of the spacing of the time constant axis the peak shape in a calculated spectrum is of no physical meaning, the width being governed by the regularization parameter α and the shape by the choice of the Tikhonov matrix and the time constant spacing.

3.2.3 Implementation

The Laplace inversion algorithm was implemented in the C programming language. To implement equation (3.15) the C interface of the industry standard BLAS [132] linear algebra library API is used. In general the BSD licensed OpenBLAS implementation is used that aims to achieve high performance on many hardware architectures [133, 134]. On the high performance computation cluster HILBERT of the university the code

can also be used together with Intel's MKL implementation of the BLAS API which is highly optimized for the CPUs used there [135].

Equation (3.15) is a linear least squares problem in \vec{g} which becomes obvious if one rewrites it as

$$f_{reg}(\vec{g}) = \|\underline{\tilde{A}} \cdot \vec{g} - \vec{\tilde{C}}_m\|_2^2 \quad (3.16)$$

where

$$\underline{\tilde{A}} = \begin{pmatrix} \underline{A} \\ \alpha \cdot \underline{D} \end{pmatrix} \quad (3.17)$$

and

$$\vec{\tilde{C}}_m = \begin{pmatrix} \vec{C}_m \\ 0 \\ \vdots \\ 0 \end{pmatrix}. \quad (3.18)$$

An unconstrained linear least squares system could be solved by calculating the Moore-Penrose inverse [136, 137] which is a generalization of the matrix inverse to non-square matrices. For the problem at hand it is, however, clear that for a normalized capacitance transient with a given amplitude C_0 at $t = 0$ (corresponding to the first element of the vector \vec{C}_m) and $C(t \rightarrow \infty) = 0$ the condition

$$\sum_j \vec{g}_j = C_0 \quad (3.19)$$

must be fulfilled. Furthermore, it is beneficial to be able to limit the solution space to $\vec{g}_j \leq 0$ or $\vec{g}_j \geq 0$ for all j if it is known that a capacitance transient consists only of decay contributions with that sign [126]. It was possible to make one of these assumptions for all LDLTS results presented in this thesis. Hence, a more general purpose minimization algorithm that can deal with such box constraints is desirable.

Thus, an established GPLv2 (or later) licensed implementation [138] of the Levenberg-Marquardt optimization algorithm [139, 140] was used to carry out the minimization. In accordance with its license the inverse Laplace transform algorithm implemented in this thesis is licensed under the GNU General Public License version 3 or later.

The Levenberg-Marquardt optimization algorithm makes use of the Jacobian matrix \underline{J} of the objective function to approach a local minimum. Since the algorithm is designed to deal with non-linear objective functions the Jacobian is re-evaluated after each iteration. For the box-constrained linear least squares problem given by equation (3.16) the Jacobian is a constant and can be easily identified with $\underline{J} = \underline{\tilde{A}}$. Thus, the source code of the Levenberg-Marquardt implementation was modified to keep the constant Jacobian in memory and not re-evaluate it during the minimization process to increase the performance.

Due to the sparse nature of the regularization matrices \underline{D} the actual calculation of the objective function in the code is carried out according to equation (3.15) instead

of (3.16) to be able to exploit the structure of the chosen regularization matrix for a performance increase.

The initial guess for the spectral density vector can be either all zeros or a constant chosen such that the resulting transient matches the initial value of the measurement. This can be selected from the configuration file, although the choice of the initial guess never showed any meaningful influence on the final result so far.

The resulting Laplace inversion code reads the transient data from a `.csv`-file and carries out a box-constrained, regularized minimization according to equation (3.16) for a set of α values over a logarithmically spaced time constant interval. The box constraints, the values of α for which the calculation should be carried out and the time constant interval on which a solution is to be searched, are defined via a configuration file. The choice of the regularization matrix has to be made during compile time. The resulting spectral density vector for each α value is then written to a separate `.csv`-file. For testing purposes intermediate results of the spectral density vector can be piped to Gnuplot after each iteration.

Since each calculation for a specific α value is completely independent of the other calculations these computations can be carried out in parallel. Typical inversions presented in this thesis use approximately 300 different values for the regularization parameter and this thus allows for a trivial parallelization on 300 CPU cores. If multiple transients from a measurement set have to be inverted with similar parameters (see Paper 1) this allows for an even stronger parallelization. The Laplace inversion code written during this thesis can be parallelized either according to the Message Passing Interface (MPI) standard, or by simple multiple invocation with appropriately set command line arguments from a job scheduling system found on most high performance computing clusters like the HILBERT.

3.2.4 Offset correction

Ideally every capacitance transient that is to be Laplace inverted is measured long enough until the transient has decayed well below the signal to noise ratio. This quiescent value of the capacitance is treated as an offset and subtracted from the input data such that for Laplace inversions $C(t \rightarrow \infty) = 0$ is always true. This is necessary since the inversion algorithm as described until now has no possibility of introducing a constant offset other than via an infinite time constant. The time constant interval over which the spectral density vector is calculated is, however, limited to experimentally reasonable values that do not include excessively large (or small) values. Hence great care has to be taken to determine and subtract the offset before the inversion.

Furthermore, especially when measuring a set of transients with varying external parameters that influence the effective time constants of the underlying processes (e.g. the temperature sweeps in Paper 1) it is not a priori possible to set the measurement parameters and the recording time such that all measured transients are captured up until their saturation value.

To let the Laplace inversion algorithm deal with unknown offsets the obvious solution would be to introduce a constant offset as an additional fit parameter for the Levenberg-

Marquardt algorithm. This approach was taken and it was found that, unless the offset fit parameter is box-constrained to a small interval, this introduces a too large additional degree of freedom to the system. A too large offset can e.g. cause the calculated transient values to be too high and consequently cause large time constants in the solution to shift to smaller values to reduce the transients amplitudes towards larger t . A properly chosen box-constraint does require at least some knowledge or estimation regarding the actual offset, so this method was not found satisfactory.

Instead, a measured transient \vec{C}_m (the exact offset of which is not known) is always normalized such that the capacitance for the last time sample point equals to zero. The transformation matrix $\underline{\underline{A}}$ is modified to carry out the same offset subtraction on the calculated transients and can be written as

$$\underline{\underline{A}}_{ij} = \exp(-\vec{t}_i/\vec{\tau}_j) - \exp(-t_{end}/\vec{\tau}_j) = \underline{\underline{A}}_{ij} - \exp(-t_{end}/\vec{\tau}_j) . \quad (3.20)$$

In all expressions $\underline{\underline{A}}$ is thus replaced with $\underline{\underline{A}}$. For the Laplace inversion code this behavior can be switched on or off from the configuration file. For transient measurements where the precise offset is known it is best to disable this feature since it strongly reduces the influence of time constants large compared to the recording time, see figure 3.4. The points in the spectral density vector that are thus without any meaningful influence on the minimization process can still assume non zero values, e.g. due to the influence of neighboring points due to the regularization or residua from a non-zero initial guess. Care has to be taken such that these artifacts are not misinterpreted as having a physical origin. The criteria for the range of time constants which one can expect to carry meaningful information given in section 2 of Paper 1 have proven to provide a good rule of thumb.

To demonstrate the effect of the offset compensation test data was generated according to

$$C(t) = \exp\left(-\frac{t}{1\text{ s}}\right) + \exp\left(-\frac{t}{2\text{ s}}\right) + 2\exp\left(-\frac{t}{10\text{ s}}\right) + C_\infty \quad (3.21)$$

for different values for C_∞ . Each transient was normalized such that $C(0) = 1$ and random noise with an amplitude of 10^{-3} was added. The transients consist of 10^4 time samples and cover a time interval from 0 s to 10 s such that $C(t)$ has not yet decayed below the noise level.

The transients are shown in figure 3.3, where transients with positive offsets are shown in red, those with negative offsets are shown in blue and the original transient without offset is printed in bold black. It should be noted that since the transient has not yet decayed after $t = 10\text{ s}$ a negative offset does not necessarily imply negative values of $C(t)$ which makes such offset errors in measurement data less obvious.

Figure 3.4 (a) shows Laplace inversions of the test data without offset correction. Spectra with positive offsets are shown in red, those with negative offsets are shown in blue and the spectrum corresponding to the original transient without offset is printed in bold black. The dotted green lines represent the time constants in the test transients. For the unperturbed case it can be seen that for these conditions the first two time constants $\tau = 1\text{ s}$ and $\tau = 2\text{ s}$ have merged into one peak centered roughly in the middle

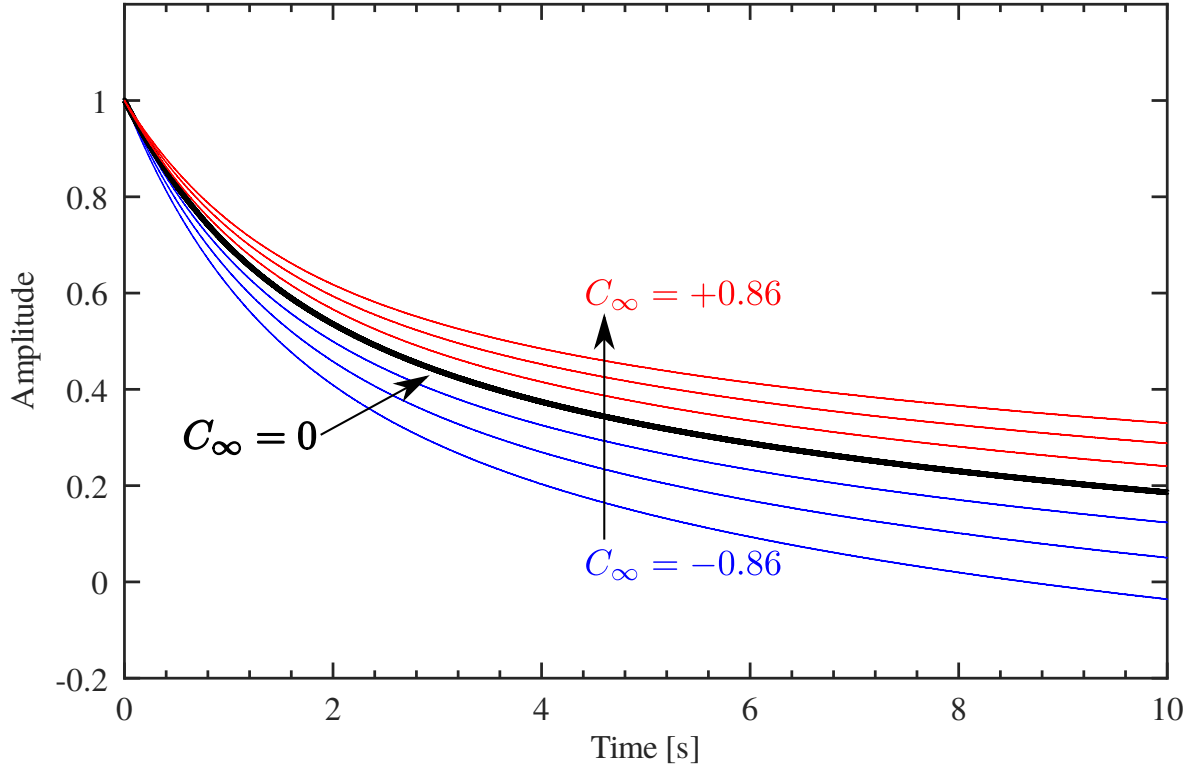


Figure 3.3: Plot of the test transients used to study the effects of offset errors in transient Laplace inversions.

of the individual time constants. The weak double peak structure is not clear enough to reliably determine the individual constituents given the non-physical peak shape. The peak for $\tau = 10$ s is positioned approximately at the correct time constant.

For positive C_∞ the spectrum gets broadened with contributions at larger time constants affected stronger. The two small time constants have been merged into one symmetric peak for all positive C_∞ . With increasing C_∞ the broadening gets stronger, consequently reducing the height of the affected peaks to maintain the correct transient amplitude according to equation (3.13). The maximum positions of the resolvable peaks are, however, almost unaffected.

For negative C_∞ even the smallest perturbation of the transient renders the resulting spectrum useless. The amplitudes of the peaks diverge and the maximum positions are shifted to smaller C_∞ . It has to be noted that the offset $C_\infty = -0.29$, causing the already drastic effects on the spectrum, causes no clearly identifiable feature in the input data. This underlines that great care has to be taken when transforming transients with unknown C_∞ .

Figure 3.4 (b) shows the same data Laplace inverted using the offset correction. It can be seen that the spectra are independent of C_∞ with the maximum positions of the resolvable peaks roughly at the correct time constants. The peaks are slightly broadened towards larger time constants which can be explained by the aforementioned reduced influence of time constants large compared to the recording time on the objective function. With the regularization now being the only effect influencing the spectrum at

these time constants the optimal solution becomes an overly smooth variation towards zero. The remaining negligible differences for different C_∞ stem from the random noise that was added resulting in small uncorrected effective offset errors on the scale of $|C_\infty| < 10^{-3}$.

Thus, it can be concluded that, unless the offset is known with high accuracy, the broadening of the spectrum induced by the offset correction is preferable over the possibly dramatic effects of a possible offset of undetermined magnitude.

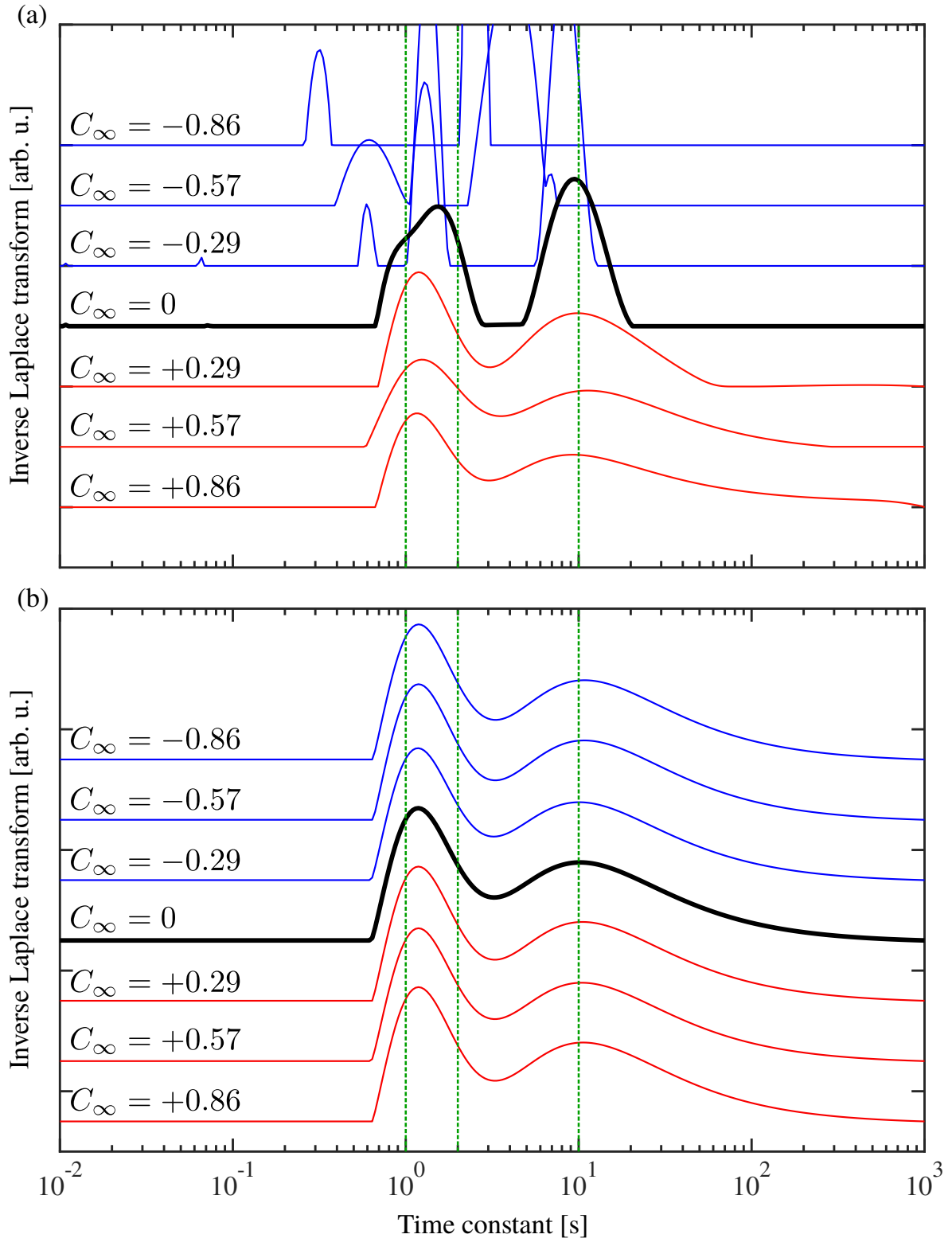


Figure 3.4: Laplace inversions of the test transients with different offset errors without (a) and with (b) offset correction turned on. Both subfigures share the same x -axis. The individual traces are shifted along the y -axis for clarity. The dashed green lines represent the time constants present in the test data.

Chapter 4

Laplace DLTS on SAQDs

4.1 Context

Conventional DLTS has been used to study the emission of electrons from SAQDs in structures similar to the one studied in this thesis [30–39]. The advantages of the LDLTS technique are shown in detail in Ref. [40] and [141] and it has been successfully used to study a wide variety of point defects in semiconductors, see e.g. Refs. [40, 141], or piezoelectric effects [142]. It has also been applied to quantum dot samples [41, 86], however, the results published so far suffer from regularization problems or were conducted in a parameter range that has also previously been accessible using conventional DLTS.

After the first task of my thesis, the implementation of an inverse Laplace transform algorithm, was completed, measurement data were taken with the explicit goal to analyze them using LDLTS. It was possible to observe the isothermal electron emission both in the tunneling regime and the thermal regime and subsequently monitor the transition between those two regimes continuously.

The observed results could be modeled using established theories and, where applicable, could be confirmed using conventional DLTS, establishing Laplace DLTS as a valuable and practical technique for the study of self-assembled quantum dots. The results have been published in a peer reviewed international journal and are included in this thesis as Paper 1.

4.2 Paper 1

JOURNAL OF APPLIED PHYSICS **124**, 104301 (2018)

Laplace deep level transient spectroscopy on self-assembled quantum dots

L. Schnorr,¹ T. Heinzel,^{1,a)} S. Scholz,² A. Ludwig,² and A. D. Wieck²¹*Solid State Physics Laboratory, Heinrich-Heine-Universität Düsseldorf, 40204 Düsseldorf, Germany*²*Lehrstuhl für Angewandte Festkörperphysik, Ruhr-Universität Bochum, 44780 Bochum, Germany*

(Received 9 March 2018; accepted 19 August 2018; published online 11 September 2018)

Self-assembled InAs quantum dots in a GaAs matrix are studied by Laplace deep level transient spectroscopy (LDLTS). This technique is demonstrated to be complementary to the well-established capacitance spectroscopy concepts and is particularly well suited for characterization of quantum dot layers with large separations from conductive layers. In comparison to conventional deep level transient spectroscopy, LDLTS can also be applied in the tunneling regime where the lifetimes of the confined states are independent of temperature, while in the thermal regime, LDLTS has a superior selectivity. The problems encountered hitherto with this technique are demonstrated to originate from the ill-posed character of the inverse Laplace transform and can be solved by a properly adapted choice of the regularization parameter. *Published by AIP Publishing.*

<https://doi.org/10.1063/1.5028319>

Reference

Reproduced from [L. Schnorr, T. Heinzel, S. Scholz, A. Ludwig, and A. D. Wieck, "Laplace deep level transient spectroscopy on self-assembled quantum dots", *Journal of Applied Physics* **124**, 104301 (2018) <https://doi.org/10.1063/1.5028319>], with the permission of AIP Publishing

Copyright statement

Authors do not need permission from AIP Publishing to reuse their own AIP Publishing article in their thesis or dissertation.

Contributions

I planned and conducted all experiments and analyzed all data. I contributed to the manuscript writing.

Laplace deep level transient spectroscopy on self-assembled quantum dots

Cite as: J. Appl. Phys. **124**, 104301 (2018); <https://doi.org/10.1063/1.5028319>

Submitted: 09 March 2018 • Accepted: 19 August 2018 • Published Online: 11 September 2018

L. Schnorr,  T. Heinzel, S. Scholz, et al.



View Online



Export Citation



CrossMark

ARTICLES YOU MAY BE INTERESTED IN

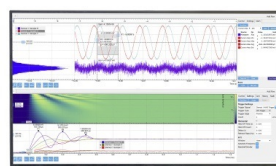
[Deep-level transient spectroscopy: A new method to characterize traps in semiconductors](#)
Journal of Applied Physics **45**, 3023 (1974); <https://doi.org/10.1063/1.1663719>

[Laplace-transform deep-level spectroscopy: The technique and its applications to the study of point defects in semiconductors](#)
Journal of Applied Physics **96**, 4689 (2004); <https://doi.org/10.1063/1.1794897>

[Nonequilibrium carrier dynamics in self-assembled quantum dots](#)
Applied Physics Reviews **6**, 031306 (2019); <https://doi.org/10.1063/1.5091742>

Challenge us.

What are your needs for
periodic signal detection?



Zurich
Instruments

Laplace deep level transient spectroscopy on self-assembled quantum dots

L. Schnorr,¹ T. Heinzel,^{1,a)} S. Scholz,² A. Ludwig,² and A. D. Wieck²

¹*Solid State Physics Laboratory, Heinrich-Heine-Universität Düsseldorf, 40204 Düsseldorf, Germany*

²*Lehrstuhl für Angewandte Festkörperphysik, Ruhr-Universität Bochum, 44780 Bochum, Germany*

(Received 9 March 2018; accepted 19 August 2018; published online 11 September 2018)

Self-assembled InAs quantum dots in a GaAs matrix are studied by Laplace deep level transient spectroscopy (LDLTS). This technique is demonstrated to be complementary to the well-established capacitance spectroscopy concepts and is particularly well suited for characterization of quantum dot layers with large separations from conductive layers. In comparison to conventional deep level transient spectroscopy, LDLTS can also be applied in the tunneling regime where the lifetimes of the confined states are independent of temperature, while in the thermal regime, LDLTS has a superior selectivity. The problems encountered hitherto with this technique are demonstrated to originate from the ill-posed character of the inverse Laplace transform and can be solved by a properly adapted choice of the regularization parameter. *Published by AIP Publishing.*

<https://doi.org/10.1063/1.5028319>

I. INTRODUCTION

Self-assembled quantum dots (SAQDs) form, under certain conditions, during the epitaxial growth of semiconductor heterostructures.¹ SAQDs have matured into a broad research field over the past 20 years and are used in optical devices like infrared light emitting diodes² and lasers,³ solar cells,⁴ and as single photon sources,⁵ as well as for the generation of entangled photons.⁶ In electronics, they have been studied in relation to flash memory cells,⁷ to spin storage,⁸ and as spin quantum bits which may act as nodes in optoelectronic quantum networks.⁹

It is, therefore, important to have a large repertoire of methods available for the preparation and diagnostics of SAQD states and their interaction with the environment. The optical and optoelectronic techniques are complemented by all-electronic concepts. In addition to conductance spectroscopy,¹⁰ capacitance spectroscopy¹¹ is a powerful tool that provides many fascinating results such as the magnetic-field dependence of the SAQD electron and hole states and the corresponding wave functions,¹² or the study of many-particle spin states out of equilibrium.¹³ The standard capacitance vs. voltage (CV) spectroscopy is based on elastic tunneling of electrons between the SAQD states and a conductive layer, which must be in close proximity ($\lesssim 30$ nm) to the SAQD layer, in order to keep the tunneling rates sufficiently large.^{14–16} However, in many structures, larger distances are required. In intermediate-band solar cells, for example, the SAQD layers are embedded in the space charge region of a p-n diode with typical widths of $1\ \mu\text{m}$.^{4,17} Single photon sources, which host the SAQDs at the center of an optical resonator, require a spacing of about a quarter of an optical wavelength to the closest conductive layer. In structures for a conductive readout of the SAQD state, a high mobility of the two-dimensional electron gas is helpful, which requires a large distance in order to avoid a reduction of the mobility by strain effects of the SAQD layer.¹⁴

Deep level transient spectroscopy (DLTS)¹⁸ overcomes this limitation of the conventional capacitance spectroscopy since it does not require direct tunneling between the SAQDs and the conductive layer. Some DLTS measurements on SAQD layers with large distances to the contacts have been reported,^{19–28} and the activation energies of the SAQD states were obtained from the temperature dependence of the capacitance transients.²⁹ This method, however, has some limiting requirements. Measurements over large temperature intervals are necessary, and the interpretation of the data is hampered by the coexistence of thermal emission and tunneling with a temperature-dependent weight.

Laplace-DLTS (LDLTS), which is based on an inverse Laplace transformation of capacitance transients, is a complementary technique, which offers some distinct advantages when compared to more established characterization techniques based on transport spectroscopy.³⁰ It does not require temperature sweeps, can be used in both the thermal and the tunneling regime, and has a higher resolution under certain circumstances, for example, in the study of point defects in Si.³¹ Also, since the lifetime of a localized state in the tunneling regime depends exponentially on the width of the approximately triangular tunneling barrier, a suitable tunneling rate window can be selected via the applied bias voltage. Furthermore, the concept is commensurate with the increasingly important characterization of deep impurity levels in SAQD samples which are known to, for example, limit the lifetime of spin qubits and reduce the quantum efficiency.³²

Thus, LDLTS is potentially a valuable and complementary experimental method to characterize samples that contain SAQD layers with large distances from electrodes, which are inaccessible using conventional CV spectroscopy based on resonant tunneling, since it is capable of providing separate information on electron- and hole states (in contrast to optical methods) at a fixed temperature (in contrast to DLTS), which also enables a separation and quantification of thermal and tunneling contributions.

Applications of LDLTS to SAQD layers have been scarce.^{31,33} In a pioneering work, Lin *et al.* have obtained

^{a)}thomas.heinzel@hhu.de

multi-peaked lifetime distributions, which could not be attributed to the SAQD states.³¹ They interpreted this observation in terms of charge-dependent emission rates which hamper the extraction of the corresponding energy spectra. Since that time, LDLS has essentially no longer been applied to SAQD samples. However, it appears somewhat strange that established capacitance-voltage measurements, as well as DLTS, do give accurate energy spectra of large SAQD ensembles embedded in quite similar heterostructures.

In this work, we revisit LDLS on SAQD samples and show that meaningful data can be obtained by this technique. The results demonstrate that by LDLS, the lifetimes and the binding energies of the states of SAQDs, which are highly decoupled from their environment in our samples, can be studied with hitherto unprecedented resolution and accuracy in the tunneling regime. LDLS also offers complementary options in the thermal regime, which are demonstrated by a discussion of thermally assisted tunneling and by an analysis of the emission lifetimes in the mixed regime, where tunneling and thermal emission coexist. The difficulties previously described were encountered, but they can, at least in our experimental implementation, be traced back to the numerics of the inverse Laplace transformation and are avoided by carefully selecting the regularization parameter.

The outline of the paper is as follows. In Sec. II, the layout of the samples, the experimental setup, and the Laplace DLTS algorithm are described. The experimental results and their interpretation are given in Sec. III. The paper closes with a summary in Sec. IV.

II. EXPERIMENTAL SETUP AND DATA ANALYSIS METHODS

The semiconductor heterostructures that contain the SAQDs are grown by molecular beam epitaxy. A GaAs/AlAs short-period superlattice is grown on a GaAs single crystal which predominantly smoothens the growth interface, but also acts as a trap for diffusing and segregating impurities. After an undoped GaAs spacer layer of 50 nm thickness, a 300 nm layer of highly Si-doped GaAs (doping density $2 \times 10^{18} \text{ cm}^{-3}$) is grown, which acts as a back electrode. A weakly Si-doped GaAs layer (thickness 500 nm, doping density $2 \times 10^{16} \text{ cm}^{-3}$) forms the spacer between the back electrode and the SAQD layer, which is grown by a conventional Stranski-Krastanov protocol, where InAs SAQDs form on top of an InAs wetting layer. The SAQDs have a sheet number density of 10^{14} m^{-2} , a nearly circular base area of about 30 nm diameter, and a height of approximately 7 nm. Another weakly doped GaAs layer (thickness 400 nm, doping density $2 \times 10^{16} \text{ cm}^{-3}$) finishes the heterostructure. This design excludes CV spectroscopy based on elastic tunneling and at the same time corresponds to typical distances between the SAQD layer and the electrodes encountered in SAQD-based, optoelectronic devices. The wafer is cleaved into pieces of $\approx 25 \text{ mm}^2$ size, and optical lithography, in combination with metallization and annealing steps, is used to define a Cr/Au top electrode of lateral size $0.3 \text{ mm} \times 0.3 \text{ mm}$, as well as an In Ohmic contact to the back electrode. The capacitor structure to be measured is formed by the top and back electrode,

the latter of which is grounded in all experiments reported below. A cross-sectional scheme of the sample is shown in Fig. 1(a).

The experiments are carried out at electron temperatures between $T \approx 3.3 \text{ K}$ and 80 K in a $^3\text{He}/^4\text{He}$ dilution refrigerator. All measurements reported below were taken on the same sample and in the absence of magnetic fields. In Fig. 1(b), a capacitance-voltage (CV) spectrum of the sample is shown. An AC voltage (amplitude 10 mV, frequency 7.1 MHz) is added to the DC bias voltage V_G , which is applied to the top electrode with respect to the grounded back electrode, and the out-of-phase signal is detected with a lock-in amplifier. As V_G is increased, a characteristic increase in the capacitance is observed, showing weakly pronounced peaks that indicate the population of the s- and p-states of the SAQDs, respectively. These chemical contributions to the capacitance from SAQD states are poorly visible when compared to those obtained at samples which are optimized for CV spectroscopy, i.e., where the spacer between the back electrode and the SAQD layer is about one order of magnitude thinner than in our system (see, e.g., Refs. 12, 14, and 34). We note that in our experiments, these spectra are independent of the excitation frequency down to 5 Hz. In comparison to conventional structures used for CV spectra,^{11,12,14–16} the resonances due to the SAQD states remain observable at much higher frequencies, which we attribute to the doping of the spacer layer which flattens the band at energies close to resonance, thereby decreasing the effective width of the tunnel barrier.

Figure 1(c) illustrates our concept for the LDLS measurements. The readout state is defined by a bias voltage V_r ,

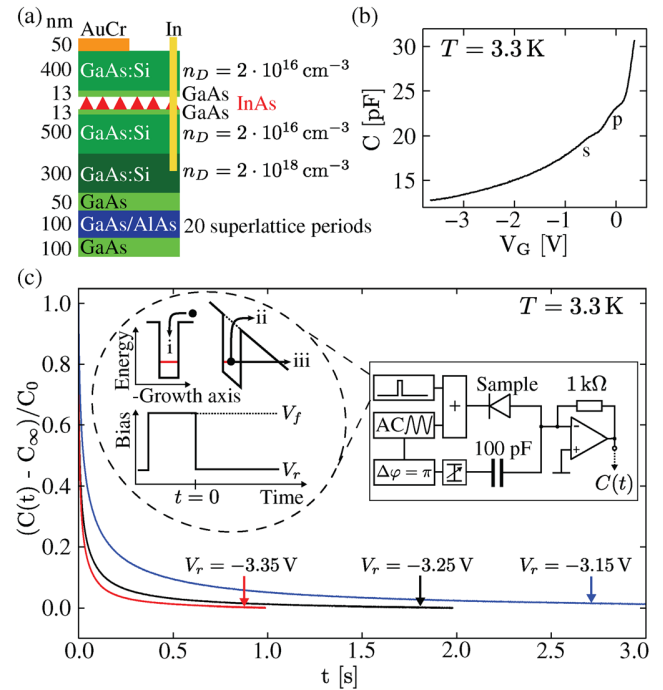


FIG. 1. (a) Cross sectional schematic view of the sample layout. (b) A conventional CV-spectrum of the sample, recorded at an excitation frequency of 7.1 MHz. (c) A set of capacitance transients recorded in the tunneling regime for different emission voltages. Sketches of the measurement setup and of the bias pulse sequence are shown in the inset.

i.e., the emission voltage at which the SAQDs emit the electrons across the approximately triangular barrier into the conduction band. V_r is chosen well below the voltage $V_s \approx -800$ mV, see Fig. 1(b), at which resonance between the s states and the back electrode is established, such that all SAQD states are well above the Fermi level of the back electrode. To fill the SAQD levels [process i in Fig. 1(c)], a positive filling pulse voltage V_f is applied for a sufficiently long time t_f (typically $t_f \in [50 \text{ ms}, 500 \text{ ms}]$). After the filling pulse, V returns to V_r , and the electrons leave the SAQDs by thermionic emission [process ii in Fig. 1(c), which dominates at higher temperatures], elastic tunneling (process iii, which is most relevant at low temperatures) or by a combination of both in the form of activated tunneling. These relaxation processes have characteristic time constants which manifest themselves in the recorded capacitance transient $C(t)$. The relationship between the relevant charge distributions and the measured capacitance transients was explained in detail by Miller *et al.*³⁵

Our setup is sketched in the inset of Fig. 1(c). The bias pulses are generated by an arbitrary waveform generator (PicoScope 5244B digital oscilloscope from Pico Technology), and the resulting capacitance transients are measured using a HF2LI lock-in amplifier oscillating at $f = 10.4$ MHz and a HF2TA transimpedance amplifier with $Z = 1$ k Ω from Zurich Instruments. A second AC voltage, which is shifted by a phase of $\Delta\varphi = \pi$ with respect to the test voltage, is applied to a 100 pF capacitor, and the resulting current is added to the current through the sample. By varying the amplitude of the shifted excitation voltage, the input of the transimpedance amplifier can be brought close to zero, which allows for transient measurements in a more sensitive range. The transients in the out-of-phase component of the resulting current are sampled with a time resolution of at least $\Delta t = 100$ μ s over a variable total recording time t_r , using the above-mentioned PicoScope 5244B. All transients were averaged over several identical pulses to achieve a decent signal to noise ratio a_S/a_N . Figure 1(c) shows typical examples of the resultant averaged capacitance transients.

We proceed by describing the algorithm for the numerical inverse Laplace transformation, where, for a given lifetime grid $\vec{\tau}$, the inverse Laplace transform vector $g(\vec{\tau})$ of the normalized capacitance transient $C(\vec{\tau})$ is calculated. It is well-known that due to the ill-posed character of the inverse Laplace transform,³⁶ it is unreliable to obtain the results by determining the least-squares solution of

$$f(\vec{g}) = \|\vec{C} - \underline{\underline{A}} \cdot \vec{g}\|_2^2, \quad (1)$$

where $\underline{\underline{A}}$ is the transformation kernel matrix given by

$$\underline{\underline{A}}_{ij} = \exp(-\vec{\tau}_i / \vec{\tau}_j), \quad (2)$$

and $\|\dots\|_2$ denotes the 2-norm of the vector. This problem can be avoided by applying the Tikhonov regularization,³⁷ which introduces an additional term to the objective function of the minimization process that inhibits unwanted aspects in the solution and acts as a damping term. The expression to be minimized is then given by³⁸

$$f_{\text{reg}}(\vec{g}) = \|\vec{C} - \underline{\underline{A}} \cdot \vec{g}\|_2^2 + \|\alpha \cdot \underline{\underline{D}} \cdot \vec{g}\|_2^2, \quad (3)$$

where $\underline{\underline{D}}$ is the forward difference operator with zero boundary conditions acting as the Tikhonov matrix. This operator inhibits rapid changes in the solution vector and thereby avoids a Laplace spectrum where noise in the capacitance transient is overrepresented. Since there is no general criterion for the choice of the Tikhonov matrix for a specific problem, this operator was chosen based on the work by Hansen.³⁸ For each inversion, the range of the lifetime grid is chosen such that the solution is guaranteed to be zero at the boundaries. This is achieved by selecting the minimum experimentally meaningful lifetime τ_{\min} smaller than the sampling interval Δt . Also, the maximum lifetime τ_{\max} to be calculated is chosen such that the exponential decay of the signal over the recording time is larger than the noise level. These criteria, thus, lead to the conditions

$$\tau_{\min} < \Delta t, \quad (4)$$

$$\tau_{\max} > \frac{-t_r}{\ln(1 - a_N/a_S)}, \quad (5)$$

where a_N and a_S denote the noise and the signal amplitude, respectively. Note that contributions of lifetimes outside $[\tau_{\min}, \tau_{\max}]$ bear no physical meaning and are included solely for numerical stability.

The regularization parameter α determines the weight of the regularization term and requires a particularly careful selection. If α is chosen too small, the obtained lifetime distribution contains additional, physically meaningless peaks, which emerge from noise in the original data. Too large values of α , on the other hand, would blur the real lifetime distribution. α was chosen by a criterion, which is based on the accurate knowledge of the signal-to-noise ratio of the measured transients as described in the [supplementary material](#). An established implementation³⁹ of the Levenberg-Marquardt optimization algorithm^{40,41} was used to carry out the minimization for 300 different regularization parameters per transient.

III. RESULTS AND DISCUSSION

We begin with the results of two experiments that have been designed to determine the plausibility and quality of our LDLTS data. For a LDLTS study of the electron emission in the tunneling regime, which is impossible by DLTS, capacitance transients were measured at a fixed temperature of 3.3 K after a filling pulse of $V_f = +0.4$ V height and $0.1t_r$ duration, while the recording voltage V_r was varied. As will be shown below, thermal emission is absent at this temperature, and tunneling is the only accessible emission channel. The recording time t_r was adjusted between 100 ms and 10 s such that the saturation of each transient could be captured. The pulse sequences were repeated between 10^4 and 10^6 times, depending on the recording time, and the measured capacitance transients were averaged. A subset of three such transients is depicted in Fig. 1(c).

For each averaged capacitance transient, the inverse Laplace transformation was calculated as outlined above.

Examples of the corresponding Laplace spectra are shown in Fig. 2(a). Thus, two lifetime peaks are observed within the selected range of emission voltages, which we interpret as the lifetimes τ_{s1} and τ_{s2} of the two s-states, the degeneracy of which is lifted by the Coulomb blockade. As will become clear below, the lifetime τ_p of the p-states is much shorter and cannot be resolved under these conditions. The maxima of both peaks shift towards shorter lifetimes as V_r are decreased.

Korol derived an expression for the emission lifetime τ_{si} of the Fowler-Nordheim type tunneling from a confined state with binding energy E_{si} into the conduction band under the presence of an electric field F at zero temperature T ,⁴² which reads

$$\tau_{si}(T = 0, F) = \frac{4\sqrt{2m^*E_{si}}}{eF} \exp\left(\frac{4}{3} \frac{\sqrt{2m^*E_{si}^3/2}}{e\hbar F}\right), \quad (6)$$

where $m^* = 0.067m_e$ is the effective electron mass of GaAs and e represents the elementary charge. Since the electric field at the quantum dot layer is determined by the applied bias voltage, the doping densities, and the sample geometry, this relation allows a translation of the lifetimes into binding energies. Since, unlike homogeneously distributed defects, all SAQDs in our sample are located at the same distance from the back contact, the electric field F at the SAQD layer could be determined by a one-dimensional Poisson-Schrödinger solver⁴³ at a fixed temperature of $T = 3.3$ K as a function of the applied emission voltage.

The emission lifetimes $\tau_{si}(F)$ ($i = 1, 2$) were determined from the positions of the two peaks of the lifetime distributions. In Fig. 2(b), τ_{si} is plotted vs. the electric field, and the corresponding fits to Equation (6) are shown (solid lines), with the binding energies as fit parameters. The 95% confidence interval for each fit is depicted by the dotted lines. The binding energies $E_{s1} = (177 \pm 2)$ meV and $E_{s2} = (165 \pm 1)$ meV are obtained, both with reasonable values and in agreement with literature values, see below. This analysis shows that LDLTS allows the determination of SAQD binding energies from capacitance transients in the tunneling regime.

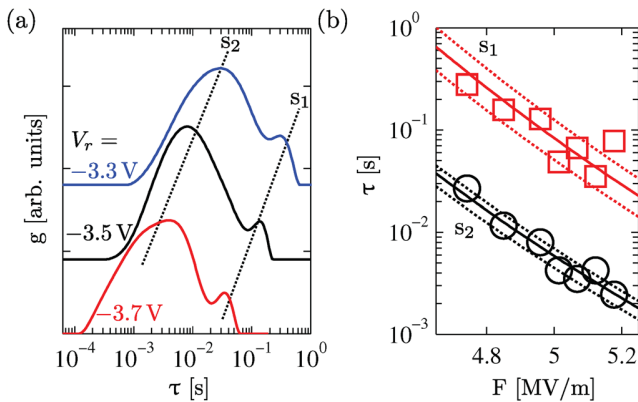


FIG. 2. (a) Lifetime distributions of the s-states for three representative bias voltages as obtained from the inverse Laplace transformation of the averaged transients. The traces are shifted along the y-axis for clarity. (b) Plot of the peak positions vs. the electric field F (symbols), fits to Eq. (6) (solid lines) and the 95% confidence intervals (dotted lines). The vertical size of the symbols corresponds to the error bar for the lifetimes.

It is noted that the shape and width of the lifetime distribution peaks in Fig. 2(a) are dominated by the analysis algorithm and cannot be interpreted in terms of a distribution of the SAQD energy levels. However, the full-width at half maximum represents an upper limit for the band widths ΔE_{si} of E_{si} . In our case, this estimation is given by $\Delta E_{s1} \lesssim 6$ meV and $\Delta E_{s2} \lesssim 12$ meV.

LDLTS is also a valuable technique for experiments in the thermal regime. In our samples, thermal emission dominates the lifetimes at temperatures well above 45 K (see below). The validity of LDLTS in this regime is illustrated by a comparison of LDLTS spectra to those obtained by conventional DLTS, see Fig. 3. An emission voltage of $V_r = -1.25$ V was used, the highest value where both s-states could be observed in a DLTS scan. Also, under these conditions, the tunneling lifetimes of the SAQD states are sufficiently long, such that the emission lifetimes change significantly, but remain in a detectable range as T is varied between 3 K and ≈ 82 K. The DLTS data were obtained from the capacitance transients for two rate windows $\tau_{ref} = 500 \mu\text{s}$ and 20 ms using a standard lock-in weight function described in detail elsewhere.^{44,45} In the LDLTS experiment, the transients were measured for each temperature and inverted with a constant lifetime grid to determine $g(\tau)$. To obtain a LDLTS spectrum that can be directly compared to a classical DLTS spectrum, one fixed point of the Laplace inversion was plotted for each recorded temperature. Hence, the LDLTS spectrum shown in Fig. 3(a) can be written as $S(T) = g(\tau = \tau_{ref}, T)$. As in conventional DLTS, this line will show a maximum at the temperature where the contribution of that lifetime is the largest. The same lifetimes τ_{ref} as for the DLTS plots are chosen.

Figure 3(a) shows a comparison of the results obtained by the two techniques. One can clearly see the better resolution of the LDLTS spectrum. The approximately constant signals for temperatures below $T \approx 40$ K are due to emissions dominated by tunneling. The weakly pronounced features above this background are most likely due to thermal emission from the p-states, but the signals are not sufficiently strong for an analysis of the thermal emission from these states. Therefore, focus is placed on the signals at higher

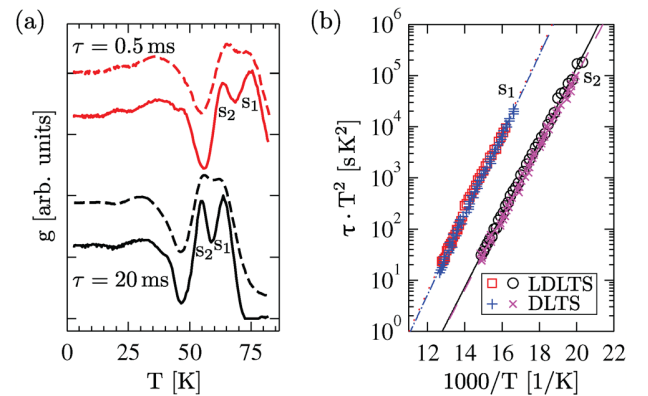


FIG. 3. (a) Comparison of the DLTS spectra obtained from the classical DLTS analysis (dashed lines) and the LDLTS spectra (solid lines) for two different rate windows ($\tau = 500 \mu\text{s}$ and 20 ms). The traces are shifted along the y-axis for clarity. (b) Arrhenius plot of the two peak positions as obtained from both evaluations.

temperatures, where two peaks are observed which we attribute to the two s-states. These peaks are just barely resolved in the conventional DLTS measurement but show a much clearer separation with the LDLTS method. There is no significant difference in the peak positions within the experimental accuracy as extracted from the two methods. The corresponding Arrhenius plots are shown in Fig. 3(b). Identical slopes clearly show that the results from both analysis methods lie on the same trap signature line.

In the thermal emission model, τ_{si} is given by the Richardson equation

$$\tau_{si}(T, F = 0) = A \cdot T^{-2} \exp\left(\frac{E_{si}}{k_B T}\right), \quad (7)$$

where the prefactor A depends on the capture cross section σ via $\sigma^{-1} = 2\sqrt{3}(2\pi)^{1.5} k_B^2 m^* A / h^3$. The fits of Eq. (7) to the data result in the values for the binding energies and the capture cross sections given in Table I.

Clearly, the LDLTS fit results are very similar to those obtained by DLTS measurements, which demonstrates the validity of the LDLTS measurement and analysis. Note that the binding energies as extracted from the temperature dependent measurements are significantly smaller than those obtained from the tunneling experiments, and that the capture cross sections are quite small, in fact much smaller than the lateral extension of the SAQDs of about 10^{-15} m^2 . However, our values are in rough agreement with those obtained by earlier DLTS measurements.²⁶ As has been shown by Vincent *et al.*,⁴⁶ the small binding energies originate from the neglect of thermally assisted tunneling, which decreases the lifetime and thereby leads to smaller apparent binding energies in the thermal emission model. Thermally assisted tunneling can be taken into account via the Vincent correction factor⁴⁶

$$\begin{aligned} f(E_{si}, F, T) &= \frac{\tau_{si}(T, F = 0)}{\tau_{si}(T, F)} \\ &= 1 + \int_0^{E_{si}} (k_B T)^{-1} \exp\left(\frac{E}{k_B T} - \frac{4\sqrt{2m^*} E^{3/2}}{3ehF}\right) dE. \end{aligned} \quad (8)$$

With this correction, we obtain the binding energies and capture cross sections as listed in Table II.

Thus, including thermally assisted tunneling in the analysis gives more realistic values for the binding energies and the capture cross sections. We attribute the remaining differences in the binding energies to the assumptions underlying the Vincent model, namely, that the activated emission rate

TABLE I. Parameters of the fit of the data shown in Fig. 3(b) to the Richardson equation [Eq. (7)].

Expt. technique	State	E_{si} (meV)	σ_{si} (10^{-18} m^2)
DLTS	s1	119	13.7
	s2	94	5.8
LDLTS	s1	119	13.1
	s2	97	8.0

TABLE II. Fit parameters of the thermal emission data including the Vincent correction.

Expt. technique	State	E_{si} (meV)	σ_{si} (10^{-16} m^2)
DLTS	s1	155	2.1
	s2	139	4.3
LDLTS	s1	155	1.8
	s2	142	6.4

at a certain activation energy is given by the tunneling density of states. In reality, the density of states in the SAQDs has additional peaks at the energies of the p- and d-states.

Once the applicability of LDLTS to our samples in the thermal regime has been established, we use this technique to study the electron emission at a fixed temperature. The sample was immersed in liquid nitrogen, and capacitance transients were recorded for different emission voltages at a constant temperature of $T = 77 \text{ K}$.

Transient measurements were carried out for emission voltages between $V_r = -1.25 \text{ V}$ and $V_r = -1.85 \text{ V}$ where both s-states are observable in one Laplace spectrum. A subset of these transients is shown in Fig. 4(a) with their corresponding Laplace inversions in the inset. One observes that the two maxima shift to shorter lifetimes as F is increased. Figure 4(b) shows the positions of these maxima plotted vs. F , as obtained from band diagram calculations for $T = 77 \text{ K}$ as described above. An exponential relationship can be observed for both states.

The decrease in the lifetimes with increasing electric fields can be explained by the Poole-Frenkel effect^{47,48} and/or by thermally activated tunneling.⁴⁶ Ganichev *et al.*⁴⁹ gave a criterion to distinguish the two emission processes. However, the electric field range covered in the measurements presented here is small in order to keep the lifetimes in a manageable interval. Thus, the proposed linear fits of

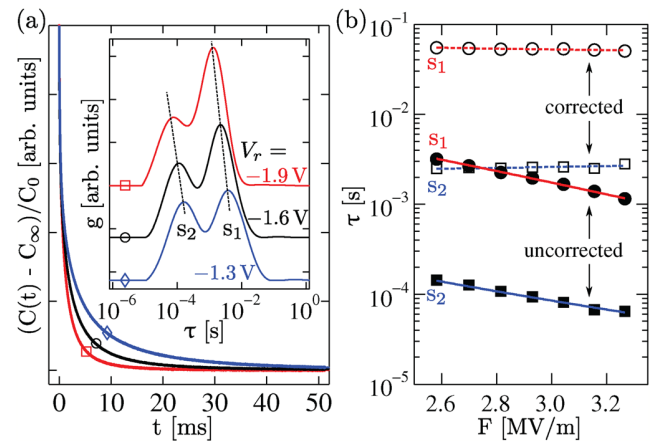


FIG. 4. (a) Normalized capacitance transients and the corresponding Laplace spectra (inset) of the two s-states for different emission voltages in the thermally activated regime. The spectra are shifted along the y-axis for clarity. (b) Semilogarithmic plot of the peak positions vs the electric field (filled symbols) and fits to Eqs. (9) and (7) in Ref. 51 (solid lines) for the s1 and s2-state, respectively (uncorrected). The data points with the Vincent correction included are shown by the empty symbols with the dashed lines as guides to the eye.

$\ln(1/\tau)$ vs. F^2 and \sqrt{F} give no additional information since both agree well with the data. To further investigate the origin of the observed lifetime decrease, we discuss both the Poole-Frenkel effect and phonon assisted tunneling under the assumption that they are the sole contributor and then compare the results with respect to their plausibility. The Poole-Frenkel effect has originally been calculated by assuming a one-dimensional Coulomb potential⁴⁷ and was later extended to also cover the three-dimensional case⁵⁰ and the square-well potential in both dimensionalities.⁵¹ We fitted each model to our data and found the best fit for the s1 state to be the 3d-square-well potential, while for the s2 state the three-dimensional Coulomb potential gave the best results. The solid lines in Fig. 4(b) are fits of Eqs. (9) and (7) in Ref. 51 to the s1 and s2-state, respectively. We attribute this to the Coulomb interaction between the two electrons inside the quantum dot during the emission from the s2 state. From the fits against the 3d-square-well model, the height of the quantum dot layer can be obtained. The resulting values are $h_{s1} = 24.6$ nm and $h_{s2} = 21.1$ nm.

Since AFM-scans over uncapped SAQDs grown under similar conditions yielded quantum dot heights of $h_{SAQD} = 5$ nm, these values are way too large. This is in agreement with earlier experiments, where the SAQD heights, as extracted by the Poole-Frenkel analysis, exceeded the realistic SAQD height by about one order of magnitude.²⁵ This discrepancy can be explained by thermally activated tunneling. We have applied the Vincent correction to the measured values $\tau_{si}(T, F)$ and the resulting values are shown as open symbols in Fig. 4(b). They appear as independent of F , which indicates that any remaining field dependence due to the Poole-Frenkel effect is negligible. If one assumes a 3d-square-well potential, which gave the best fit results for the s1-state, and the SAQD-height determined by AFM-scans, the maximum barrier lowering in the measurements presented here is estimated to $\Delta E_{PF,3d-sq} \approx 2.5$ meV. From the transparency of the triangular barrier used in the Vincent model, one can estimate that under the conditions presented in this section approximately 3% of the electrons are thermally activated in the energy interval $[E_C, E_C - 2.5 \text{ meV}]$. This low fraction explains the negligible contribution of the Poole-Frenkel effect in this measurement.

We now turn our attention to a comprehensive study of the transition from the tunneling regime to the thermal regime, where activated tunneling is significant.

For the studies of the temperature dependent emission, a filling pulse with $V_f = +0.4$ V and $t_f = 500$ ms was applied. An emission voltage of $V_r = -2.70$ V was used, corresponding to an electric field of $F = 4.09$ MV/m at the SAQD layer. The transient was recorded for a time $t_r = 5$ s with a time resolution of $\Delta t = 100$ μ s. As the sample was warmed from $T = 3.3$ K to ≈ 80 K, 120 individual transients were averaged for each data point, which were separated by $\Delta T \approx 1.7$ K. The inverse Laplace transform of the averaged transients was calculated for each temperature, which resulted in the temperature dependent lifetime density function $g(\tau)$, as shown in Fig. 5(a). The electron emission from the double and single occupied s-states can be discriminated for temperatures between $T = 3.3$ K and $T \approx 70$ K. The lifetimes of both

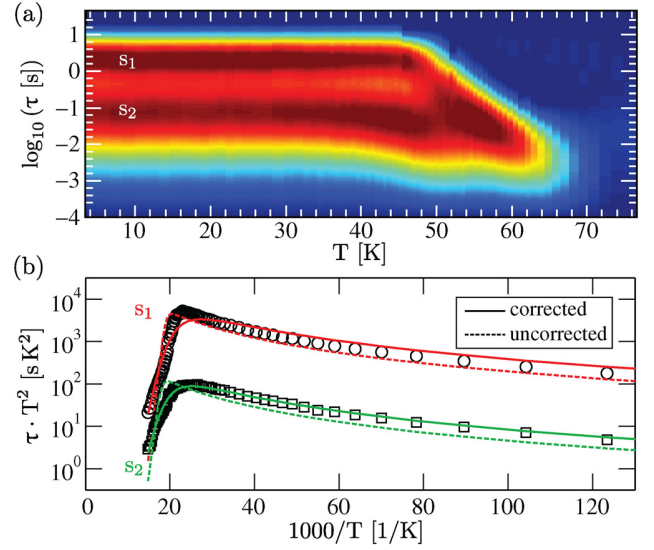


FIG. 5. (a) Color plot of the density function $g(\tau, T)$ for the two s-states as obtained from LDITS. The color code represents the spectral density in arbitrary units from low (blue) to high (red). The tunneling regime at low T is characterized by temperature-independent peaks while in the mixed and thermal regime, the lifetimes shift to smaller values as T is increased. (b) Arrhenius plot of the peak positions obtained from LDITS. The solid and dashed lines are fits to Eqs. (10) and (9), respectively.

states are independent of the temperature up to $T \approx 40$ K, indicating that tunneling from the quantum dots into the conduction band is the dominant emission process. For higher temperatures, the lifetimes of both states decrease, with the s2 state being affected at somewhat lower temperatures than the s1 state. For temperatures larger than ≈ 70 K, the lifetimes become too short to be detected with the parameters used.

For the further analysis of the temperature dependence of the lifetimes, the peak positions of the spectral density functions were determined by fitting a sum of two Gaussian functions to the line scans in Fig. 5(a) parallel to the lifetime axis for all temperatures. The Arrhenius plot of the resulting pairs $\tau_{si}(T)$ ($i = 1, 2$) is shown in Fig. 5(b). Due to the T^2 factor, τT^2 increases monotonically in the tunneling regime as T is increased. The characteristic temperature $T_{t,si}$ for the transition from the tunneling regime into the thermal regime can be defined as the temperature at which τT^2 assumes its maximum. We obtain $T_{t,s1} = 43$ K and $T_{t,s2} = 41$ K for the s1 and the s2 state, respectively. At temperatures above $T_{t,si}$, the Arrhenius plot shows a linearly decreasing behavior, corresponding to an exponential temperature dependence as expected for a thermally activated process.

We first analyze these data under the assumption that emission by tunneling and by purely thermal activation are independent events. In this case, according to Matthiessen's rule, the lifetimes of two emission processes $\tau_{si}(T=0, F)$ and $\tau_{si}(T, F=0)$ add up inversely, and the combined lifetime is obtained via

$$\tau_{si}(T, F)^{-1} = \tau_{si}(T=0, F)^{-1} + \tau_{si}(T, F=0)^{-1}. \quad (9)$$

Here, $\tau_{si}(T=0, F)$ follows Eq. (6) and $\tau_{si}(T, F=0)$ is given by Eq. (7). The results of the corresponding two-parameter

fits (E_{si} and σ_{si}) for each s-state are shown as dashed lines in Fig. 5(b). While this simple model describes the temperature-dependent lifetimes qualitatively, it fails to reproduce it quantitatively, with clearly visible deviations regarding the slope of the Arrhenius plot at small inverse temperatures, the transition temperature, and the values for the lifetimes in the tunneling regime. The fit results are shown in the upper part of Table III.

While the binding energies show good agreement with those obtained from the analysis of the tunneling data at low temperatures, the capture cross sections are extremely large and exceed the lateral SAQD area by two to three orders of magnitude. Applying the Vincent correction changes the expression for the measured lifetime to

$$\tau_{si}(T, F)^{-1} = \tau_{si}(T = 0, F)^{-1} + \frac{f(T, F)}{\tau_{si}(T, F = 0)}. \quad (10)$$

This not only improves the fits to the measured lifetimes, see Fig. 5(b), but also, reasonable values for the capture cross sections are obtained. The wide temperature range over which the Vincent correction factor gives plausible results also further supports the attribution of the electric field dependence of the lifetimes at $T = 77$ K to thermally assisted tunneling, as discussed in the context of Fig. 4.

We end this section with a comparative discussion of the extracted binding energies. Our values agree with those reported by others in comparable samples, which vary from $E_{s1} = 82$ meV (Ref. 21) over 131 meV (Ref. 25) and 154 meV (Ref. 26) to 160 meV,²⁴ with corresponding variations reported for E_{s2} . In our measurements, the largest value for E_{s1} , namely $E_{s1} = 176$ meV, is found by LDLTS in the tunneling regime. With this measurement, we can safely exclude lifetime contributions by thermal emission, while the value may change by applying a more sophisticated model, such as the consideration of the true three-dimensional potential or the inclusion of the wetting layer. The value obtained from the data in the thermal regime is $E_{s1} = 119$ meV, which increases significantly to 155 meV as thermally activated tunneling is included. Finally, the fits to the T -dependent lifetimes transitioning from the tunneling regime into the thermal regime give values of $E_{s1} = 170$ meV. This indicates that tunneling does contribute significantly to the lifetime in the thermal regime. If this contribution is neglected in the thermal regime, the additional decay channel is parameterized in a decrease in the binding energies. Since the Vincent correction of the thermal emission data is based on the tunneling density of states, the extracted, corrected binding energy is still too small, since decay paths via additional states like the p- and d-states, as well as the states in the wetting layer, are

neglected. An inclusion of these states would require extensive simulations or add further fit parameters. In the analysis of the temperature-dependent lifetimes presented in Fig. 5, this deviation is reduced, since the data obtained in the tunneling regime contribute with a larger weight to the analysis. Therefore, in our opinion, the binding energies from an analysis of the LDLTS data in the tunneling regime are the best ones that can be obtained without additional extensive device modeling. Due to the temperature independent nature of the emission process in this regime, temperature fluctuations have no effect on the results, which makes it favorable from a practical point of view as well.

IV. SUMMARY AND CONCLUSIONS

Laplace Deep Level Transient Spectroscopy (LDLTS) offers possibilities in the study of self-assembled quantum dot layers embedded in semiconductor heterostructures. In particular, it enables lifetime measurements at fixed temperatures in samples where the SAQD layer is too far away for capacitance-voltage spectroscopy, which is based on elastic tunneling between the SAQDs and the reservoir. We have used LDLTS to determine the tunneling lifetime as a function of the applied electric field at negligibly small temperatures. These measurements enable an estimation of the relevance of tunneling contributions in the thermal regime, and we show that thermally activated tunneling is significant and can be taken into account to a good approximation by the corresponding correction proposed by Vincent *et al.* A comparison of this correction to the Poole-Frenkel effect shows that the reported over-estimations of the SAQD heights can be explained to a large extent by thermally activated tunneling, which appears as an additional decrease in the barrier height and hence as a larger SAQD height, if it is not included in the analysis. We have also presented the lifetimes of the two s-states over a broad range of temperatures, which include the transition from tunneling dominated to thermally activated emission, where the second advantage of LDLTS, namely, a higher resolution as compared to DLTS, is crucial. Furthermore, we have implicitly used the possibility to adjust the lifetimes to a suitable range by selecting the electric field accordingly.

The application of LDLTS is accompanied by some numerical stepping-stones caused by the ill-posed character of the inverse Laplace transform. We have shown that these problems can be solved reliably by a proper choice of the regularization parameter, which can be cross-checked by a comparison of the LDLTS data to those obtained by conventional DLTS.

SUPPLEMENTARY MATERIAL

See [supplementary material](#) for a detailed description of the method used to find the optimum value for the regularization parameter α , which enters via Eq. (3). The effects of inadequate α values on the Laplace spectra are illustrated.

ACKNOWLEDGMENTS

The authors thank HHU Düsseldorf for financial support and acknowledge experimental support by M. Cerchez and

TABLE III. Parameters obtained from fits of the data in Fig. 5(b) to the model without [Eq. (9)] and with [Eq. (10)] the correction of Vincent *et al.* included.

Model	State	E_{si} (meV)	σ_{si} (m ²)
Without	s1	170	1.5×10^{-12}
Correction	s2	155	3.6×10^{-13}
With Vincent	s1	172	2.7×10^{-16}
Correction	s2	157	1.7×10^{-16}

J. Schluck. The authors are particularly grateful to C. Rothfuchs for assistance during the sample preparation. Stimulating discussions with M. Geller and A. Lorke are gratefully acknowledged. They thank M. Ottensmann for a careful proofread of the manuscript. Computational support and infrastructure was provided by the “Centre for Information and Media Technology” (ZIM) at the University of Düsseldorf (Germany).

- ¹D. Leonard, M. Krishnamurthy, C. M. Reeves, S. P. Denbaars, and P. M. Petroff, *Appl. Phys. Lett.* **63**, 3203 (1993).
- ²I. L. Krestnikov, N. A. Maleev, A. V. Sakharov, A. R. Kovsh, A. E. Zhukov, A. F. Tsatsulnikov, V. M. Ustinov, Z. I. Alferov, N. N. Ledentsov, D. Bimberg, and J. A. Lott, *Semicond. Sci. Technol.* **16**, 844 (2001).
- ³V. M. Ustinov, N. A. Maleev, A. E. Zhukov, A. R. Kovsh, A. Y. Egorov, A. V. Lunev, B. V. Volovik, I. L. Krestnikov, Y. G. Musikhin, N. A. Bert, P. S. Kopev, and Z. I. Alferov, *Appl. Phys. Lett.* **74**, 2815 (1999).
- ⁴A. Luque, A. Marti, and C. Stanley, *Nat. Photonics* **6**, 146 (2012).
- ⁵P. Michler, A. Kirazl, C. Becherl, W. V. Schoenfeld, P. M. Petroff, L. Zhang, E. Hu l, and A. Imamoglu, *Science* **290**, 2282 (2000).
- ⁶C. L. Salter, R. M. Stevenson, I. Farrer, C. Nicoll, D. A. Ritchie, and A. J. Shields, *Nature* **465**, 594 (2010).
- ⁷A. Marent, T. Nowozin, J. Gelze, F. Luckert, and D. Bimberg, *Appl. Phys. Lett.* **95**, 242114 (2009).
- ⁸M. Krouvar, Y. Ducommun, D. Heiss, M. Bichler, D. Schuh, G. Abstreiter, and J. J. Finley, *Nature* **432**, 81 (2004).
- ⁹A. Faraon, A. Majumdar, D. Englund, E. Kim, M. Bajcsy, and J. Vuckovic, *New J. Phys.* **13**, 055025 (2011).
- ¹⁰B. Marquardt, M. Geller, A. Lorke, D. Reuter, and A. D. Wieck, *Appl. Phys. Lett.* **95**, 022113 (2009).
- ¹¹H. Drexler, D. Leonhard, W. Hansen, J. P. Kotthaus, and P. M. Petroff, *Phys. Rev. Lett.* **73**, 2252 (1994).
- ¹²O. Wibelhoff, A. Lorke, D. Reuter, and A. W. Wieck, *Appl. Phys. Lett.* **86**, 092104 (2005).
- ¹³B. Marquardt, M. Geller, B. Baxevanis, D. Pfannkuche, A. D. Wieck, D. Reuter, and A. Lorke, *Nat. Commun.* **2**, 209 (2011).
- ¹⁴A. Kurzmann, B. Merkel, B. Marquardt, A. Beckel, A. Ludwig, A. D. Wieck, A. Lorke, and M. Geller, *Phys. Status Solidi B* **254**, 1600625 (2017).
- ¹⁵R. J. Luyken, A. Lorke, A. O. Govorov, J. P. Kotthaus, G. Medeiros-Ribeiro, and P. Petroff, *Appl. Phys. Lett.* **74**, 2486 (1999).
- ¹⁶S. R. Valentin, J. Schwinger, P. Eickelmann, P. A. Labud, A. D. Wieck, B. Sothmann, and A. Ludwig, *Phys. Rev. B* **97**, 045416 (2018).
- ¹⁷T. Li, H. Lu, L. Fu, H. H. Tan, C. Jagadish, and M. Deganaï, *Appl. Phys. Lett.* **106**, 053902 (2015).
- ¹⁸D. V. Lang, *J. Appl. Phys.* **45**, 3023 (1974).
- ¹⁹S. Anand, N. Carlsson, M.-E. Pistol, L. Samuelson, and W. Seiffert, *Appl. Phys. Lett.* **67**, 3016 (1995).
- ²⁰C. M. A. Kapteyn, F. Heinrichsdorff, O. Stier, R. Heitz, M. Grundmann, N. D. Zakharov, D. Bimberg, and P. Werner, *Phys. Rev. B* **60**, 14265 (1999).
- ²¹C. M. A. Kapteyn, M. Lion, R. Heitz, D. Bimberg, P. M. Brunkov, B. V. Volovik, S. G. Konnikov, A. R. Kovsh, and V. M. Ustinov, *Appl. Phys. Lett.* **76**, 1573 (2000).
- ²²C. M. A. Kapteyn, M. Lion, R. Heitz, D. Bimberg, C. Miesner, T. Asperger, and G. Abstreiter, *Appl. Phys. Lett.* **77**, 4169 (2000).
- ²³M. Geller, C. Kapteyn, L. Müller-Kirsch, R. Heitz, and D. Bimberg, *Appl. Phys. Lett.* **82**, 2706 (2003).
- ²⁴O. Engström, M. Malmkvst, Y. Fu, H. O. Olafsson, and E. O. Sveinbjörnsson, *Appl. Phys. Lett.* **83**, 3578 (2003).
- ²⁵S. Schulz, S. Schnüll, C. Heyn, and W. Hansen, *Phys. Rev. B* **69**, 195317 (2004).
- ²⁶A. Schramm, S. Schulz, J. Schäfer, T. Zander, C. Heyn, and W. Hansen, *Appl. Phys. Lett.* **88**, 213107 (2006).
- ²⁷A. Schramm, S. Schulz, C. Heyn, and W. Hansen, *Phys. Rev. B* **77**, 153308 (2008).
- ²⁸A. Schramm, S. Schulz, T. Zander, C. Heyn, and W. Hansen, *Phys. Rev. B* **80**, 155316 (2009).
- ²⁹M. Geller, E. Stock, C. Kapteyn, R. L. Sellin, and D. Bimberg, *Phys. Rev. B* **73**, 205331 (2006).
- ³⁰L. Dobaczewski, P. Kaczor, I. D. Hawkins, and A. R. Peaker, *J. Appl. Phys.* **76**, 194 (1994).
- ³¹S. W. Lin, E. Stock, M. Missous, I. D. Hawkins, B. Hamilton, O. Engström, and A. R. Peaker, *Mater. Sci. Eng. C* **26**, 760 (2006).
- ³²R. J. Warburton, *Nat. Mater.* **12**, 483 (2013).
- ³³P. Kruszewski, L. Dobaczewski, V. P. Markevich, C. Mitchell, M. Missous, and A. R. Peaker, *Physica B* **401–402**, 580 (2007).
- ³⁴H. Drexler, Ph.D. thesis, LMU Munich (1994).
- ³⁵G. L. Miller, D. V. Lang, and L. C. Kimerling, *Ann. Rev. Mater. Sci.* **7**, 377 (1977).
- ³⁶S. W. Provencher, *Comput. Phys. Commun.* **27**, 229 (1982).
- ³⁷A. N. Tikhonov, *Dokl. Akad. Nauk SSSR* **151**, 3 (1963).
- ³⁸P. Hansen, *Discrete Inverse Problems* (Society for Industrial and Applied Mathematics, 2010).
- ³⁹M. Lourakis, <http://www.ics.forth.gr/lourakis/levmar/> for “levmar: Levenberg-marquardt nonlinear least squares algorithms in C/C++,” 2004; accessed 31 January 2005.
- ⁴⁰K. Levenberg, *Q. Appl. Math.* **2**, 164 (1944).
- ⁴¹D. W. Marquardt, *J. Soc. Ind. Appl. Math.* **11**, 431 (1963).
- ⁴²E. N. Korol, *Fizika Tverdogo Tela* **19**, 1266 (1977).
- ⁴³G. Snider, <https://www3.nd.edu/~gsnider/> for 1D Poisson-Schrodinger solver, 2017; accessed 15 September 2017.
- ⁴⁴D. S. Day, M. Y. Tsai, B. G. Streetman, and D. V. Lang, *J. Appl. Phys.* **50**, 5093 (1979).
- ⁴⁵L. Schnorr, M. Cerchez, D. Ostermann, and T. Heinzel, *Phys. Status Solidi B* **253**, 690 (2016).
- ⁴⁶G. Vincent, A. Chantre, and D. Bois, *J. Appl. Phys.* **50**, 5484 (1979).
- ⁴⁷G. Frenkel, *Phys. Rev.* **54**, 647 (1938).
- ⁴⁸J. G. Simmons, *Phys. Rev.* **155**, 657 (1967).
- ⁴⁹S. D. Ganichev, E. Ziemann, W. Prettl, I. N. Yassievich, A. A. Istratov, and E. R. Weber, *Phys. Rev. B* **61**, 10361 (2000).
- ⁵⁰J. Hartke, *J. Appl. Phys.* **39**, 4871 (1968).
- ⁵¹P. A. Martin, B. Streetman, and K. Hess, *J. Appl. Phys.* **52**, 7409 (1981).

Supplementary Material to "Laplace deep level transient spectroscopy on self-assembled quantum dots"

L. Schnorr and T. Heinzel*

Solid State Physics Laboratory, Heinrich-Heine-Universität

Düsseldorf, 40204 Düsseldorf, Germany

S. Scholz, A. Ludwig, and A. D. Wieck

Lehrstuhl für Angewandte Festkörperphysik,

Ruhr-Universität Bochum, 44780 Bochum, Germany

(Dated: August 20, 2018)

Abstract

This supplement exemplifies our method of choosing the regularization parameter α that appears in eq. (3) of the manuscript as a critical input for the inverse Laplace transform. The choice is illustrated on a representative capacitance transient, recorded at $T = 77$ K and an emission voltage of $V_r = -1.3$ V. Its signal to noise ratio of $a_S/a_N = 1689$ was achieved by averaging over 230300 identical pulses. The transient consists of $N = 49386$ data points over a total recording time of $t_r = 197$ ms.

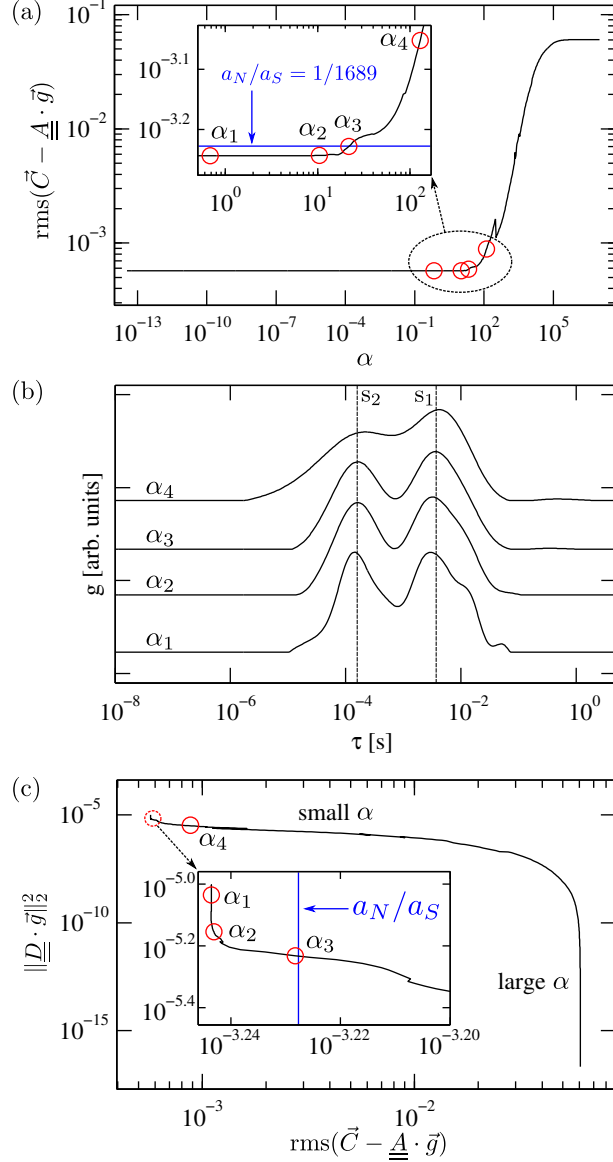


FIG. 1. (color online) (a) Plot of the root-mean-square of the difference between the measured capacitance transient and the back-transformed solution of the minimization process vs. the regularization parameter α . (b) Plot of the spectra obtained from the Laplace inversion using the regularization parameters as indicated in (a). The vertical lines mark the peak position as obtained from the result using $\alpha = \alpha_3$. The traces are shifted along the y-axis for clarity. (c) Plot of the L-curve as described in the text.

Fig. 1(a) shows the root mean square of the difference between the measured capacitance transient and the back-transformed solution of the minimization process as a function of the regularization parameter α . For small (large) α , the residual norm saturates at low

(high) values. The inset shows the onset of the step of this function in comparison to the noise to signal ratio of the averaged transient ($a_N/a_S = 1/1689$). The two traces intersect at α_3 , which is the optimum choice for the regularization. If a smaller value for α is used, the corresponding spectra are difficult to interpret since the minimization process represents measurement noise as additional structure in the spectral density function \vec{g} , as shown in Fig. 1(b) for the spectra with $\alpha = \alpha_1$ and $\alpha = \alpha_2$. If, on the other hand, α is selected too large, the unnecessarily high damping causes a smearing of the spectral function, as is demonstrated for $\alpha > \alpha_3$ in Fig. 1(b). In Fig. 1(c), the L-curve as described in Ref. 38 of the main paper, i.e., the 2-norm of the product of the Tikhonov matrix with the spectral density solution vector vs. the rms of the difference between the measured capacitance transient and the back-transformed solution, is plotted. The inset shows a zoom on the transition region from the vertical to the horizontal branch. The circled data points correspond to the same values of α as in (a). According to the L-criterion, the best choice of α is the point of maximum curvature in the transition region. Here, α_2 marks the best choice, while α_3 would be considered as too large. This comparison shows that for the scenario considered here, the first criterion, which is based on an exact knowledge of the (sufficiently high) signal-to noise ratio, is to be preferred over the criterion based on the L-curve. The additional structure

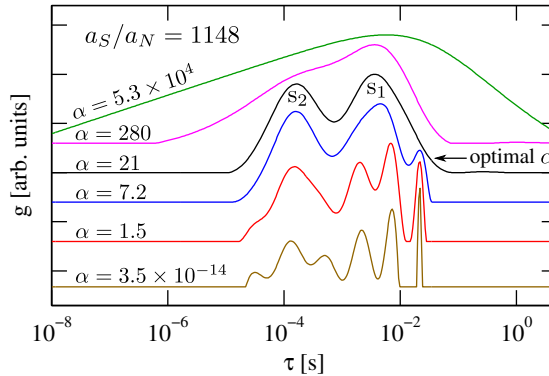


FIG. 2. (color online) Laplace spectra for representative choices of α for the same data set as shown in Fig. 1 but with only half the amount of averaging. The traces are shifted along the y-axis for clarity.

that appears in the Laplace spectra if α has been chosen too small can become dominant if the signal-to noise ratio is not sufficiently high. This is illustrated in Fig. 2, where the same transient as in Fig. 1 is used, but with averaging over only 50% of the traces, such that the

signal to noise ratio decreases to $a_S/a_N = 1148$. The lowermost trace represents a solution with effectively no regularization. It can clearly be seen that this solution incorporates significantly more noise artifacts than the spectrum calculated for $\alpha = \alpha_1$ in figure 1. One can observe six clearly separated peaks which remain visible as α is increased by several orders of magnitude. They merge within a relatively narrow interval until only two peaks are left for the optimal choice of α , according to the above discussion. This example shows that α needs to be chosen carefully and that this choice becomes more and more critical as the signal to noise ratio decreases. In our studies, a reliable inverse Laplace transform is possible for signal to noise ratios above $a_S/a_N \approx 1000$.

* thomas.heinzel@hhu.de

Chapter 5

Capture and emission dynamics far from equilibrium with the environment

5.1 Context

The well established capacitance-voltage spectroscopy [25] is commonly used to study the resonances of SAQD states with the Fermi level of a reservoir [5, 25–28, 143]. In these measurements the dynamics of the SAQD states as a whole can be observed via the dependence of the measurement signals on the frequency used to measure the capacitance [4, 5]. A separate measurement of both the capture and the emission rates has, to the best of my knowledge, not yet been reported using such capacitive techniques.

Until now, DLTS studies on SAQDs have always been conducted in regimes where it was reasonable to only consider carrier emission in the analysis and neglect the capture rate, see e.g. Refs. [36–39].

After establishing LDLTS as a valuable technique for the study of SAQDs the next goal in this thesis was to explicitly study the dynamics of the SAQDs in parameter ranges which have been carefully avoided so far. Isothermal LDLTS and DLTS measurements were conducted at $T = 77$ K and bias pulses were applied that cover the entire experimentally available voltage range for the sample structure under study. The non-trivial results could be modeled quantitatively with great accuracy and required the consideration of non-negligible electron capture rates as well as the interplay between the capture and emission rates in a transition regime. They include the first direct capacitive measurements of electron capture into self-assembled quantum dots.





A key result of this work is that the measured capture rates as well as the steady state configuration that could be extrapolated from the data are much larger than expected if a thermal equilibrium between the SAQDs and their environment is assumed, indicative of a different electron source that dominates the capture process compared to the back contact under the studied conditions.

The results have been published in a peer reviewed international journal and are included in this thesis as Paper 2.



5.2 Paper 2

PHYSICAL REVIEW B **104**, 035303 (2021)

Electron capture and emission dynamics of self-assembled quantum dots far from equilibrium with the environment

L. Schnorr , J. Labes , L. Kürten , and T. Heinzel *

Solid State Physics Laboratory, Heinrich-Heine-Universität Düsseldorf, 40204 Düsseldorf, Germany

C. Rothfuchs-Engels,[†] S. Scholz, A. Ludwig , and A. D. Wieck 

Lehrstuhl für Angewandte Festkörperphysik, Ruhr-Universität Bochum, 44780 Bochum, Germany



(Received 18 March 2021; revised 10 June 2021; accepted 6 July 2021; published 14 July 2021)

The electron transfer dynamics between self-assembled quantum dots and their environment are measured under nonequilibrium conditions by time-dependent capacitance spectroscopy. The quantum dots are embedded in a wide spacer, which inhibits elastic tunneling to or from the reservoirs. At certain bias voltages, electron capture and emission are both significant. A rate equation model is used to determine the corresponding transfer rates and the average occupation numbers of the dots as a function of the bias voltage.

DOI: [10.1103/PhysRevB.104.035303](https://doi.org/10.1103/PhysRevB.104.035303)

Reference

L. Schnorr, J. Labes, L. Kürten, T. Heinzel, C. Rothfuchs-Engels, S. Scholz, A. Ludwig, and A. D. Wieck Phys. Rev. B **104**, 035303 (2021)

DOI: <https://doi.org/10.1103/PhysRevB.104.035303>

©2021 American Physical Society





Copyright statement

The author has the right to use the article or a portion of the article in a thesis or dissertation without requesting permission from APS, provided the bibliographic citation and the APS copyright credit line are given on the appropriate pages.

Contributions

I planned all and conducted most of the experiments and analyzed all data. I contributed to the manuscript writing.

Electron capture and emission dynamics of self-assembled quantum dots far from equilibrium with the environment

L. Schnorr , J. Labes , L. Kürten , and T. Heinzel ^{*}*Solid State Physics Laboratory, Heinrich-Heine-Universität Düsseldorf, 40204 Düsseldorf, Germany*C. Rothfuchs-Engels,[†] S. Scholz, A. Ludwig , and A. D. Wieck *Lehrstuhl für Angewandte Festkörperphysik, Ruhr-Universität Bochum, 44780 Bochum, Germany*

(Received 18 March 2021; revised 10 June 2021; accepted 6 July 2021; published 14 July 2021)

The electron transfer dynamics between self-assembled quantum dots and their environment are measured under nonequilibrium conditions by time-dependent capacitance spectroscopy. The quantum dots are embedded in a wide spacer, which inhibits elastic tunneling to or from the reservoirs. At certain bias voltages, electron capture and emission are both significant. A rate equation model is used to determine the corresponding transfer rates and the average occupation numbers of the dots as a function of the bias voltage.

DOI: [10.1103/PhysRevB.104.035303](https://doi.org/10.1103/PhysRevB.104.035303)

I. INTRODUCTION

Self-assembled quantum dots (SAQDs) [1] are not only studied extensively in fundamental science [2–5], they have also found their way into applications such as light-emitting diodes [6] or quantum dot lasers [7]. SAQDs are furthermore discussed in relation to transport devices, such as ultrasmall dynamic random access memory cells [8]. For this field, the dynamical properties of electronic transitions between the SAQD states and the environment are highly relevant. Many aspects of such charge transfers have been studied in the past two decades [9–23].

In standard elastic capacitance-voltage (CV) spectroscopy [9], resonances indicate the energetic alignment of the SAQD electron or hole states with the Fermi energy of the reservoir [9–12]. In this situation, the Fermi-Dirac distributions in the SAQD layer and in the back gate are identical, and we refer to this as *equilibrium*. The concept can also be extended to the nonequilibrium case [13,24]. In such CV experiments, the capture and emission times enter via the frequency dependence of the capacitance amplitudes and define an average, characteristic time constant [13,14]. However, the capture and emission time constants cannot be determined separately from such data. Recently, progress has been reported in this respect due to various experimental techniques. In transconductance spectroscopy, voltage pulses were used to prepare the charge state of the SAQDs, after which the capture and emission times were determined from the conductivity transients in a nearby two-dimensional electron gas [15,16]. Kurzmann *et al.* [17] measured electron escape rates from SAQDs via the quenching of excitonic transitions. Also, electron tunneling rates have been determined by the effect of these electrons on the Auger ionization processes [18].

These techniques have in common that they rely on an electron reservoir close to the SAQD layer, i.e., with a distance of ≤ 30 nm, to allow elastic tunneling, or that spacer layers of larger thickness are sufficiently doped to enable a predominantly flat band between the reservoir and the SAQDs close to resonance [11]. Therefore, they are unsuitable to study capture rates of SAQDs embedded in large, weakly doped spacers to the reservoirs, as is common in optical applications such as light-emitting diodes [6], laser structures [7], single photon sources [2], or solar cells [25]. Recently, such highly isolated SAQDs were studied in relation to ultralong spin qubit lifetimes [26]. Some further experiments based on optical studies of electron filling processes in SAQDs [19–21] as well as indirect measurements studying the influence of the electron capture dynamics on the subsequent photon emission [22,23] have been carried out. Previous studies based on deep-level transient spectroscopy (DLTS) [27] have shown a significant influence of the electron capture dynamics on subsequent electron emission [28–31]. In these situations, the sample is out of equilibrium, but a local equilibrium can be reached after the transients have decayed. Hitherto, an all-electrical measurement scheme suited to directly study both the capture and emission transients of SAQD layers with large distances to the reservoirs and/or out of equilibrium has not been reported yet.

Here, we show that such a scheme can be implemented based on established DLTS measurement techniques by measuring both capture and emission transients. For this proof of principle, an SAQD layer is embedded into an insulating layer providing distances of ≈ 500 nm from the electron reservoirs. In a significant bias voltage interval, capture and emission occurs simultaneously, resulting in nontrivial capacitance transients. We analyze them with a rate equation model to obtain the voltage-dependent capture and emission rates as well as the steady-state occupation probability of the dots. In Sec. II, the sample design and the experimental setup are described. The experimental results are reported in Sec. III. The measurements are interpreted within a rate equation model in Sec. IV. The paper concludes with a summary and an outlook (Sec. V).

^{*}Thomas.Heinzel@hhu.de[†]Present address: DESY, Notkestrasse 85, 22607 Hamburg, Germany.

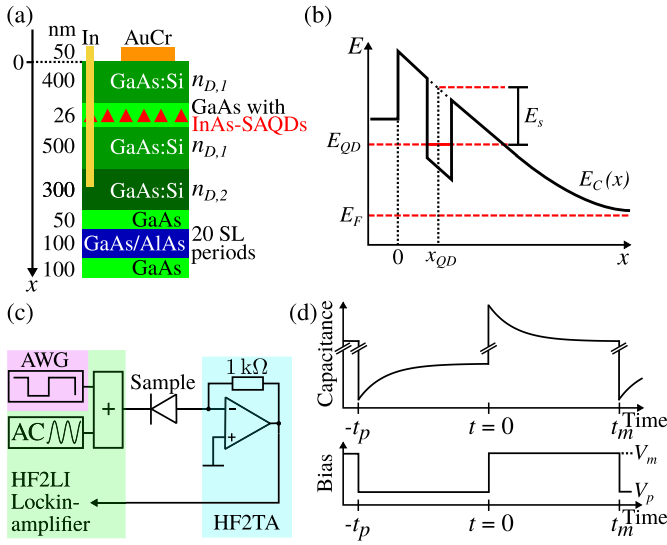


FIG. 1. (a) Cross-sectional schematic view of the sample layout. The SAQD layer is indicated by the red triangles. (b) Schematic band diagram for the case of a negative voltage applied to the top gate with respect to the grounded embedded electrode, including our conventions for the quantities of relevance. (c) Scheme of the measurement setup. (d) Illustration of the bias voltage pulses and transient capacitive response.

II. SAMPLE CHARACTERIZATION AND EXPERIMENTAL TECHNIQUES

In the structures under study, the SAQDs reside in a plane inside a semiconductor heterostructure grown by molecular beam epitaxy. On top of a GaAs single crystal, a GaAs/AlAs short-period superlattice is grown that decreases the surface roughness and acts as a protective barrier for impurities that may segregate from the substrate toward the SAQD layer; see Fig. 1(a). An embedded electrode is formed by a 300 nm layer of highly Si-doped GaAs with a doping density of $n_{D,2} = 2 \times 10^{18} \text{ cm}^{-3}$. A weakly Si-doped GaAs spacer layer (doping density $n_{D,1} = 2 \times 10^{16} \text{ cm}^{-3}$) establishes a large distance between this electrode and the SAQD layer, which is grown in the Stranski-Krastanov mode. The layer contains InAs SAQDs with a sheet density of 10^{11} cm^{-2} and is surrounded by in total 26 nm of undoped GaAs. The SAQDs have a nearly circular base of $\approx 30 \text{ nm}$ diameter, and a height of approximately 7 nm. A weakly doped GaAs layer (thickness 400 nm, doping density $n_{D,1} = 2 \times 10^{16} \text{ cm}^{-3}$) covers the SAQDs and forms the surface of the heterostructure.

The wafer is cut into pieces with an area of $5 \text{ mm} \times 5 \text{ mm}$. Optical lithography and subsequent metallization are applied to define a Cr/Au top electrode of lateral size $0.3 \text{ mm} \times 0.3 \text{ mm}$, and, via a subsequent alloy step, an indium Ohmic contact to the back electrode. In terms of DLTS, the overall structure can be regarded as a Schottky diode, with the SAQD layer representing an ensemble of defect states. This structure is the same as that used in Ref. [32].

The sample is inserted into a liquid nitrogen dewar. At a temperature of $T = 77 \text{ K}$, negative DC bias voltages are applied to the top gate with respect to the back contact, which is kept at the virtual ground of an HF2TA transimpedance

amplifier ($Z = 1 \text{ k}\Omega$) from Zurich Instruments. The voltage pulses are generated using a Keithley Model 3390 arbitrary waveform generator (AWG) with a transition time of 100 ns.

The potential energy of the electrons increases as one approaches the top gate from the back contact; see Fig. 1(b) for a sketch of the potential landscape, where also the labeling conventions of the energies and distances with relevance for the following discussions are introduced. The electronic ground-state energy of the SAQDs is denoted by E_{QD} , while the corresponding binding energy E_s is the energy difference $E_C(x_{QD}) - E_{QD}$, with $x_{QD} = 413 \text{ nm}$ being the distance of the SAQD layer from the sample surface. E_F denotes the Fermi energy for electrons in the back contact. For the measurements of capacitance transients, an AC voltage of 20 mV amplitude and a frequency of 28.9 MHz is superimposed to the DC bias voltages, and the out-of-phase signal of the resulting current is measured as a function of time (corresponding to transient capacitance) using an HF2LI lock-in amplifier from Zurich Instruments and sampled using a PicoScope 5444B digital oscilloscope from Pico Technology. All transients were sampled with a time resolution of at least $\Delta t = 10 \mu\text{s}$ over a variable recording time. This measurement configuration is illustrated in Fig. 1(c). By applying different bias voltages to the gate [Fig. 1(d)], the energies of the electronic states in the SAQDs can be tuned, and the system reacts by electron capture or emission, respectively, the time dependence of which can be monitored by capacitance transients. A certain initial condition is established by applying a preparation voltage V_p for a time t_p . Afterwards, a measurement voltage V_m is applied for a time t_m during which the capacitance transient $C(t)$ is recorded.

III. EXPERIMENTAL RESULTS

We first look at the electron filling dynamics as a function of V_m by Laplace-DLTS (LDLTS) [33].

The capture transients are measured after applying a preparation voltage $V_p = -2.0 \text{ V}$ for $t_p = 50 \text{ ms}$ to ensure that the emission processes have decayed well below the detection threshold [32]. Hence, the SAQDs can be expected to be empty to a good approximation. For each V_m , the capacitance transients are averaged over 3×10^5 individual traces in order to obtain a signal-to-noise level > 1000 as required for a numerically stable inverse Laplace transform.

In Fig. 2(a), typical averaged capacitance transients observed for the electron capture are reproduced. Already in the raw data, a strong dependence of the characteristic decay time τ on V_m is observed. As V_m is increased, τ decreases. In previous isothermal measurements of the emission rates as a function of the bias voltage [32], we observed very good agreement with the Vincent theory of thermally assisted tunneling [34], where the voltage dependence enters via the transparency of an approximately triangular barrier. Thus, as a first assumption, it appears plausible to apply this theory to the voltage dependence of the capture rate as well. According to the Fowler-Nordheim picture [35], the transparency η of this tunnel barrier is given by

$$\eta = \exp\left(-\frac{4}{3} \frac{\sqrt{2m^*} E_s^{3/2}}{q\hbar F}\right), \quad (1)$$

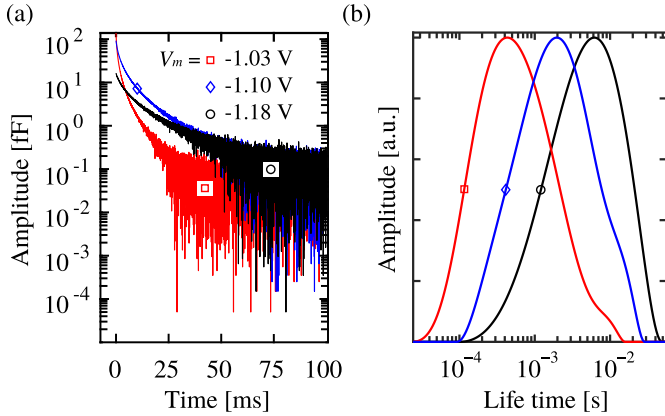


FIG. 2. Absolute value of the capacitance transients for three different measurement voltages V_m after depletion of the SAQDs by a preparation voltage of $V_p = -2.0$ V (a) and the corresponding Laplace spectra, with normalized amplitudes (b).

where F is the electric field and m^* is the effective electron mass. Since band-structure calculations show an approximately linear relationship between V_m and F [36], and an increase in η leads to an increased charge-transfer rate, one expects an increasing time constant as V_m is increased, in striking contrast to the observations. We note that this ansatz does not imply that the captured electrons originate from the back electrode; see below.

This indicates that for the capture dynamics in our system, elastic tunneling across the barrier between the SAQDs and the conduction band is of marginal relevance. Rather, since an increase of V_m decreases $E_{\text{QD}} - E_F$, this observation suggests that the capture of electrons has a thermally activated character.

The most obvious assumption is thermal activation across the energy barrier $E_a = E_C(x_{\text{QD}}) - E_F$ between the back contact and the quantum dots; see Fig. 1(b). An equilibrium model for this process, however, leads to a contradiction with the measurements. To see this, we have calculated the band structure for the applied bias voltage to obtain $E_C(x, V)$ and the local electron density $n_e(x, V)$ at 77 K, using a one-dimensional Poisson-Schrödinger solver [37] and GNU-Octave [38]. In detail, the SAQD layer is not included in the simulation but rather is included by hand afterwards. This is possible since the energies of the SAQD states with respect to the GaAs band edge are well known from many experiments (see, e.g., Refs. [22,39]), and in particular also for our present system from capacitance transients for the emission process reported earlier [32]. The sample structure was simulated as given in Fig. 1(a) with a built-in potential of 0.63 V as obtained from a conventional $C^{-2}(V)$ analysis [36]. If we assume a Fermi-Dirac distribution of the electrons in the back contact, the occupation probability for electrons at the energy levels of the SAQDs is merely 10^{-26} at $V_m = -1$ V, where a strong charging signal can be observed. Furthermore, integrating the calculated local electron density over an interval of ± 100 nm around the SAQD layer and multiplying it with the gate area yields an average number of only 10^{-12} electrons available per dot. Thus, electron capture of electrons from the back contact within an equilibrium picture can safely be

excluded for the pulse voltages used here. This is also in tune with our observation of a significant DC current flow between the top electrode and the back gate under the bias voltages used here [36]. In the following, we therefore do not assume an equilibrium distribution for the electrons between the SAQDs and the back gate [24], although it is not generally excluded and may be possible for specific bias voltages. Instead, we describe the transfer process empirically in terms of capture and emission rates without any reference to the conduction band profile.

The inverse Laplace transforms of the transients give the corresponding lifetime distributions; see Fig. 2(b). Each transient is dominated by a single time constant, in contrast to previous measurements of electron emission on the same sample, where separate time constants from the single- and two-electron state could be observed [32]. It should be emphasized that the peak shape originates from the regularization method necessary to stabilize the numerical Laplace inversion, and it cannot be interpreted in terms of physical sample properties.

The amplitudes of the transients drop rapidly as V_m is decreased below -1.0 V, i.e., a decrease by an order of magnitude is found as V_m is decreased from -1.03 to -1.18 V. This strong suppression puts a lower limit to the accessible range of V_m where capture can be observed.

To study the voltage dependence of the charge-transfer dynamics, we have performed lock-in DLTS [40] measurements at $T = 77$ K using a square-wave voltage pulse with $t_p = t_m = 94.9$ ms, and a transition time of $t_{p \leftrightarrow m} = 100$ ns, as sketched in Fig. 1(d). The voltages V_p and V_m cover all combinations within $[-3.0$ V, 0 V] with a step size of $\Delta V = 40$ mV. After applying V_p for t_p , the transient is measured at V_m applied for the time interval t_m with a time resolution of $\Delta t = 10$ μ s. Prior to the start of each averaging process, we wait for a settling time of 3 s in order to let the system adjust to the new parameters. After measuring 500 identical transients per combination of V_p and V_m , the lock-in signal $S(V_p, V_m)$ is calculated [40] from the average of these transients, where

$$S(V_p, V_m) = \sum_{i=1}^{N_t/2} C(t_i, V_p, V_m) - \sum_{i=N_t/2+1}^{N_t} C(t_i, V_p, V_m), \quad (2)$$

with the total number of data points N_t in the transient. No gate-off period has been used, since ringing/overshooting of our setup was negligible for the parameter ranges in use. The lock-in method is used here since it is impossible to acquire the required large amount of data by LDLTS in a reasonable time. The results are shown in Fig. 3(a). A positive signal (orange to dark red) corresponds to an increase in charge stored at the SAQD layer, while a negative one (dark blue to yellow) indicates a decrease. A vanishing signal represents either no charge transfer or a transfer that is too fast or too slow to cause a significant change during t_m .

Two prominent features can be observed. For $V_p \lesssim -1$ V and $V_m \in [-1.2, -1.0]$ V the positive signal shows that electron capture dominates, at a rate within the rate window of the lock-in function. Likewise, for $V_p \gtrsim -1$ V and $V_m \in [-2.0, -1.0]$ V the signal is negative, indicative of predominant electron emission. While both of these features depend strongly on V_m , there is almost no dependence on the

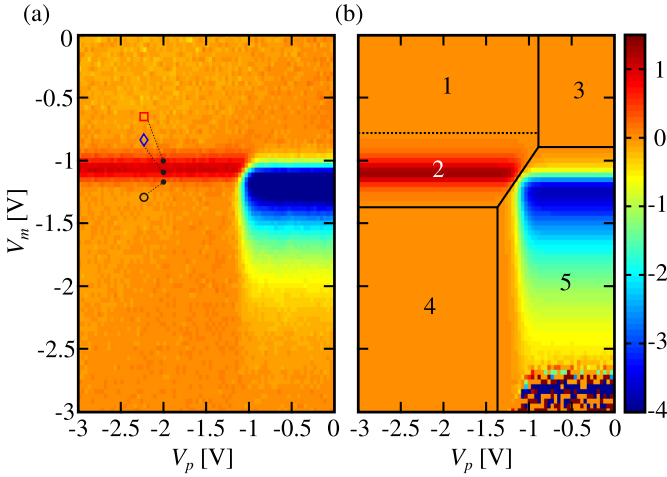


FIG. 3. Color plot of the measured (a) and calculated (b) lock-in signal $S(V_p, V_m)$ in arbitrary units as a function of V_p and V_m . The same color map applies to both subfigures. The black dots in (a) mark the points where the three capture transients shown in Fig. 2 (with the corresponding symbols) were taken. The numbers in (b) denote different charge-transfer regimes as explained in the text.

preparation voltage outside of the transition interval, given by $V_p \approx (-1.0 \pm 0.2)$ V. As we will show in more detail below, the capture and emission rates are comparable in this interval, and the average occupation probability of the relevant SAQD states varies around 50%. Kapteyn *et al.* [29] studied the dependence of the emission DLTS signal amplitude both as a function of V_p for a fixed V_m and as a function of V_m for a fixed V_p . Their approach is equivalent to lineouts of the region $V_p > V_m$ of our Fig. 3, since in the work of Kapteyn *et al.* only the electron emission was measured. Qualitatively, their data match our findings very well. Here, we study the capture dynamics over a wide parameter range, leading to information from both the dynamics and magnitudes of the filling process, as well as from its interplay with the subsequent emission.

IV. RATE EQUATION MODEL AND INTERPRETATION

Since we study the SAQD system in a nonequilibrium state, an interpretation of the data based on a self-consistent solution of the Poisson-Schrödinger equation [37], which corresponds to a band structure in equilibrium, is inadequate here, while a calculation of the nonequilibrium band structure is beyond our scope. Rather, we proceed by interpreting the experiments in terms of a rate equation model. This approach does not depend on geometric properties or the material compositions of the SAQDs. The emission rates from the one- and two-electron state can be measured separately by LDLTS [32]. On the other hand, the capture dynamics reported above show only one time constant. We thus model our system by assuming that an SAQD can be charged with up to two electrons. Capture occurs with a voltage-dependent rate $c(V)$ that is independent of the charge state of the dot. We assume two separate rates $r_{10}(V)$ and $r_{21}(V)$ for emission from the one- and the two-electron state, respectively, and a capture rate independent of the charging state. Further studies at lower temperatures may be able to resolve the state-dependence of

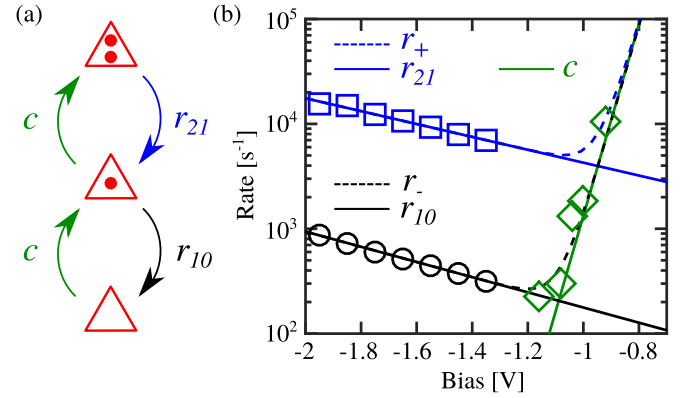


FIG. 4. (a) Illustration of the rate equation model, Eqs. (3)–(5). Red triangles denote SAQDs and the full red circles show electrons therein, while the transfer rates are symbolized by arrows. (b) Measured transfer rates in comparison to the rate equation model. The symbols denote isothermal rate constant measurements of the two emission paths [32] and of the capture process, respectively. The solid lines show the transfer rates according to Eqs. (8)–(10), using the results of the fit described in the text. The dashed lines represent the rate constants according to Eq. (7).

the capture rate, an experiment that is beyond our scope here. The electron transfer dynamics can be described by the set of differential equations for the time evolution of the density of SAQDs that have either captured zero, one, or two electrons:

$$\dot{n}_0 = -cn_0 + r_{10}n_1, \quad (3)$$

$$\dot{n}_1 = -cn_1 + r_{21}n_2 + cn_0 - r_{10}n_1, \quad (4)$$

$$\dot{n}_2 = +cn_1 - r_{21}n_2. \quad (5)$$

Here, a dotted symbol denotes the time derivative of the quantity. The relations of the quantities in this model are illustrated in Fig. 4(a). From its solution, the total charge density in the SAQD layer $n(t)$ can be derived, which is proportional to the measured capacitance transients,

$$C(t) \propto n(t) = n_1(t) + 2n_2(t). \quad (6)$$

Equations (3)–(5) were solved analytically using the SymPy library [41], and the solutions are given in the supplemental material [36]. By analyzing the resulting expression for $C(t)$ [Eq. (6)], it can be shown that it is a superposition of two exponential decays with two observable charge-transfer rates r_{\pm} given by

$$r_{\pm} = \frac{1}{2}(2c + r_{10} + r_{21} \pm \sqrt{4cr_{10} + r_{10}^2 - 2r_{21}r_{10} + r_{21}^2}). \quad (7)$$

This analytical solution is well-known from the study of multistep reaction kinetics in chemistry where this set of differential equations describes the time-dependent concentration of the substances involved [42]. Here, we use this solution for a wide variety of initial conditions, as opposed to its use in chemistry, where the equations are often simplified due to a specific initial condition.

TABLE I. Fit parameters used to calculate the results shown in Figs. 3(b) and 4(b).

m_{10} (V^{-1})	n_{10}	m_{21} (V^{-1})	n_{21}	m_c (V^{-1})	n_c
-1.67	3.51	-1.41	6.94	21.02	28.21

Based on previous measurements of an exponential voltage dependence of the emission rates [32], we model the rates as follows:

$$r_{10}(V) = \exp(m_{10}V + n_{10})s^{-1}, \quad (8)$$

$$r_{21}(V) = \exp(m_{21}V + n_{21})s^{-1}, \quad (9)$$

$$c(V) = \exp(m_cV + n_c)s^{-1}. \quad (10)$$

The constants introduced here— m_{ij} , n_{ij} , m_c , and n_c —are to be determined by a fit to the measured data. For the emission rates, the m_{ij} correspond to the slope of the approximated Vincent correction factor [43], whereas the n_{ij} represents the logarithm of the pure thermal emission rates without any residual voltage dependence. Due to the lack of equivalent theories for the capture process that we are aware of, the interpretation of the respective fit parameters remains to be discussed. To calculate the capacitance transients for any combination of V_p and V_m , we need to insert into Eqs. (8)–(10) the exact time dependence of the bias transition between V_p and V_m and assume plausible initial conditions for $n_i(t = 0)$.

The time constants of the transients vary greatly as a function of the bias voltage and can assume quite high values. To reach the steady state as the initial condition for each measurement would require an adaptation of t_p for each V_p and take an *a priori* unknown amount of time. Fortunately, the model does not require a steady state as the initial condition, which greatly simplifies the measurement process. We assume that after t_p , a steady state has not necessarily been reached, and we take into account the exact time evolution of the preparation transients as a function of V_p . This evolution depends in turn on the time evolution of the previous measurement. This is taken into account by solving Eqs. (3)–(5) for an arbitrary initial condition, for example $n_0(t = 0) = 1$ and $n_1(t = 0) = n_2(t = 0) = 0$, over five subsequent pulse cycles. We observe that after already three cycles, the signal is independent of the selected initial condition. Therefore, we accept the final transient for V_m as the solution.

To obtain the unknown parameters in Eqs. (8)–(10), we fit our model to the measurements shown in Fig. 3(a). Figure 3(b) shows the lock-in signal obtained from the calculated transients using the same time resolution as in the measurement. In addition to the parameters in Eqs. (8)–(10), a scaling factor was fitted to account for the unknown proportionality in Eq. (6). The artifacts for $V_m < -2.5$ V are due to limited floating point accuracy while calculating Eqs. (8) and (9), and they were excluded from the fit. The relevant fitting parameters are given in Table I.

We note that the values for m_{10} and m_{21} agree well with the voltage dependence of the Vincent correction factor used in previous discussions of the isothermal emission rates from the *s*-states in Ref. [32]: The correction factor [36] shows a voltage dependence that can be approximated to a very good

degree by Eqs. (8) and (9). For both *s*-states, such an approximation for $V_m < -1.0$ V, under which the emission features were observed, yields a slope of $m = -1.59$ V^{-1} , i.e., the Vincent correction factor depends only weakly on the binding energy. We attribute the remaining, charge-state-dependent variations of our empirical model to the larger bias voltage range studied here, and possibly to additional interactions not accounted for in the Vincent theory. Additionally, the voltage-independent emission rates given by $\exp(n_{ij})$ closely match those obtained after applying the Vincent correction; see Fig. 4(b) in Ref. [32]. The capture constants m_c and n_c , finally, parametrize the voltage dependence of the capture rate, the physical interpretation of which is, to the best of our knowledge, unclear due to a lack of established theories.

Good agreement between the measurement and the model is observed. Figure 4(b) shows the resulting voltage dependence of the rates [Eqs. (8)–(10)] as solid lines. The symbols represent LD LTS measurements of the emission rates [32] and the capture rates shown in Sec. III, respectively, while the dashed lines show the charge-transfer rates according to Eq. (7). In the voltage interval where the emission rates could be measured by LD LTS, the observable charge-transfer rates are identical to the respective emission rates, indicating that here, electron capture is negligible. On the other hand, the LD LTS capture measurements reported above have been carried out at voltages where the charge-transfer rates have not yet converged to $c(V)$. Rather, they are influenced by competing emission processes in a non-negligible way. It should be noted, therefore, that great care is required when transients measured in such a regime are related to a band-structure profile. From the smallest observable charge-transfer rate of $r_- \approx 2.5 \times 10^2$ s^{-1} at $V \approx -1.2$ V we can calculate that one has to wait at this bias voltage for at least 19 ms until the corresponding transients have decayed by 99%. This corresponds to the worst case of the time required for a saturated charging pulse. Even though in our measurement this time was exceeded for all measurements, a saturated pulse did not generally lead to an equilibrium distribution. After a decayed transient, the SAQDs are merely in a steady-state configuration that appears to be independent of the charge distribution in the rest of the sample.

We proceed by extracting this steady-state configuration of the SAQDs as a function of the bias voltage, characterized by their average occupancy with electrons. This configuration corresponds to the solution of Eqs. (3)–(6) in the limit $t \rightarrow \infty$. The results are shown in Fig. 5.

For $V \lesssim -1.2$ V, the dots are empty in the stationary state, while they are occupied with two electrons for $V \gtrsim -0.85$ V. In the transition region in Figs. 3 and 4(b), the occupancy changes from 0 to 2 as V is increased, with a maximum for n_1 at $V = -1.025$ V. This is in tune with the observed strong decrease of the transient amplitude as the bias voltage decreases below -1.1 V (see Fig. 2). Furthermore, it confirms assumptions made previously, namely that the dots can be prepared in an empty state at $V_p \leq -1.4$ V and in a filled state at $V_p \geq -0.5$ V. Moreover, a physical interpretation of the different areas observed in Fig. 3 is now straightforward: In Region 1, the SAQDs get emptied during V_p and capture electrons at a fast rate above the resolution threshold during V_m . In Region 2, the capture rate falls inside the measurable

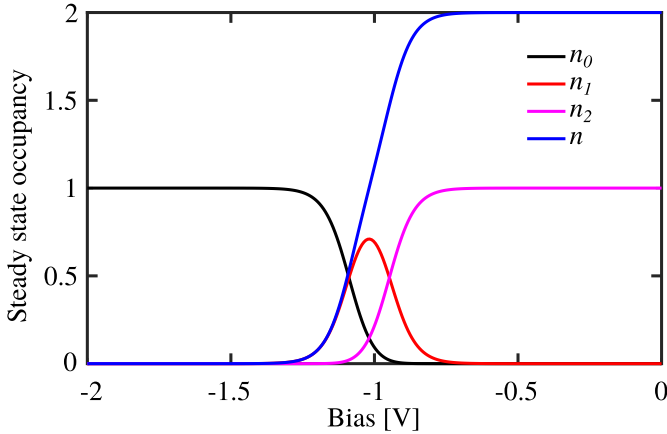


FIG. 5. Steady-state occupancy of the zero-, one-, and two-electron configurations $n_i(V)$ and the average number of electrons per dot $n(V)$.

window, while in Region 4, electron capture is negligible during t_m , i.e., the SAQDs are essentially empty. We note that only in this region is the observed electron occupation of the dots in equilibrium with the back contact. In Region 3, on the other hand, the SAQDs are filled with (at least) two electrons during V_p and remain charged during V_m . As V_m decreases, one enters into Region 5, where electron emission can be observed down to voltages of approximately -2 V. At even lower voltages, the emission becomes too fast to be monitored with our setup.

V. SUMMARY AND OUTLOOK

The reported experiments demonstrate that it is possible to determine the electron capture and emission rates of SAQDs by transient capacitance spectroscopy far from equilibrium

and without knowledge regarding the band-structure profile under these conditions. A system of coupled rate equations enables the extraction of the rate constants for electron capture and emission from the observed transients, which are influenced by both processes in the intermediate regime, where capture and emission occur simultaneously. Furthermore, by this analysis, the average occupation number of the dots with electrons as well as the voltage ranges for exclusively filling or emptying the dot states are obtained. Moreover, the concepts developed here are conceptually applicable to a variety of SAQD material systems as well as to hole states, in particular for samples where the SAQD layer is far away from electron reservoirs, like in laser structures or light-emitting diodes. Further studies on the present system may comprise isothermal measurements at various temperatures in order to determine the temperature dependence of the transfer rates, as well as possible influences of defects in the environment of the SAQD layer [44]. Advances regarding the sample inhomogeneity or by faster electronics, as well as measurements at lower temperatures, may enable the determination of state-dependent capture and emission rates. A better understanding of the transfer processes may be possible with the help of self-consistent simulations of the band structure out of equilibrium.

ACKNOWLEDGMENTS

Computational support and infrastructure was provided by the Centre for Information and Media Technology (ZIM) at the University of Düsseldorf (Germany). C.R.-E., S.S., A.D.W., and A.L. gratefully acknowledge support of TRR 160/2-Project B04, DFG 383065199, and the DFH/UFA CDFa-05-06.

- [1] D. Leonard, M. Krishnamurthy, C. M. Reeves, S. P. Denbaars, and P. M. Petroff, *Appl. Phys. Lett.* **63**, 3203 (1993).
- [2] P. Michler, A. Kiraz, C. Becher, W. V. Schoenfeld, P. M. Petroff, L. Zhang, E. Hu, and A. Imamoglu, *Science* **290**, 2282 (2000).
- [3] M. Kroutvar, Y. Ducommun, D. Heiss, M. Bichler, D. Schuh, G. Abstreiter, and J. J. Finley, *Nature (London)* **432**, 81 (2004).
- [4] C. L. Salter, R. M. Stevenson, I. Farrer, C. Nicoll, D. A. Ritchie, and A. J. Shields, *Nature (London)* **465**, 594 (2010).
- [5] A. Faraon, A. Majumdar, D. Englund, E. Kim, M. Bajcsy, and J. Vuckovic, *New J. Phys.* **13**, 055025 (2011).
- [6] I. L. Krestnikov, N. A. Maleev, A. V. Sakharov, A. R. Kovsh, A. E. Zhukov, A. F. Tsatsulnikov, V. M. Ustinov, Z. I. Alferov, N. N. Ledentsov, D. Bimberg, and J. A. Lott, *Semicond. Sci. Technol.* **16**, 844 (2001).
- [7] V. M. Ustinov, N. A. Maleev, A. E. Zhukov, A. R. Kovsh, A. Y. Egorov, A. V. Lunev, B. V. Volovik, I. L. Krestnikov, Y. G. Musikhin, N. A. Bert, P. S. Kopev, and Z. I. Alferov, *Appl. Phys. Lett.* **74**, 2815 (1999).
- [8] A. Marett, T. Nowozin, J. Gelze, F. Luckert, and D. Bimberg, *Appl. Phys. Lett.* **95**, 242114 (2009).
- [9] H. Drexler, D. Leonard, W. Hansen, J. P. Kotthaus, and P. M. Petroff, *Phys. Rev. Lett.* **73**, 2252 (1994).
- [10] O. Wibbelhoff, A. Lorke, D. Reuter, and A. W. Wieck, *Appl. Phys. Lett.* **86**, 092104 (2005).
- [11] P. N. Brounkov, A. Polimeni, S. T. Stoddart, M. Henini, L. Eaves, P. C. Main, A. R. Kovsh, Y. G. Musikhin, and S. G. Konnikov, *Appl. Phys. Lett.* **73**, 1092 (1998).
- [12] P. Kailuweit, D. Reuter, A. Wieck, O. Wibbelhoff, A. Lorke, U. Zeitler, and J. Maan, *Physica E* **32**, 159 (2006).
- [13] S. R. Valentin, J. Schwinger, P. Eickelmann, P. A. Labud, A. D. Wieck, B. Sothmann, and A. Ludwig, *Phys. Rev. B* **97**, 045416 (2018).
- [14] R. J. Luyken, A. Lorke, A. O. Govorov, J. P. Kotthaus, G. Medeiros-Ribeiro, and P. Petroff, *Appl. Phys. Lett.* **74**, 2486 (1999).
- [15] A. Beckel, A. Ludwig, A. D. Wieck, A. Lorke, and M. Geller, *Phys. Rev. B* **89**, 155430 (2014).
- [16] D. Zhou, A. Beckel, A. Ludwig, A. D. Wieck, A. Lorke, and M. Geller, *Appl. Phys. Lett.* **106**, 243105 (2015).
- [17] A. Kurzmann, A. Ludwig, A. D. Wieck, A. Lorke, and M. Geller, *Appl. Phys. Lett.* **108**, 263108 (2016).

- [18] A. Kurzmann, A. Ludwig, A. D. Wieck, A. Lorke, and M. Geller, *Nano Lett.* **16**, 3367 (2016).
- [19] S. Raymond, S. Fafard, P. J. Poole, A. Wojs, P. Hawrylak, S. Charbonneau, D. Leonard, R. Leon, P. M. Petroff, and J. L. Merz, *Phys. Rev. B* **54**, 11548 (1996).
- [20] P. Miska, J. Even, O. Dehaese, and X. Marie, *Appl. Phys. Lett.* **92**, 191103 (2008).
- [21] Y. I. Mazur, V. G. Dorogan, E. Marega, Z. Y. Zhuchenko, M. E. Ware, M. Benamara, G. G. Tarasov, P. Vasa, C. Lienau, and G. J. Salamo, *J. Appl. Phys.* **108**, 074316 (2010).
- [22] A. Schramm, S. Schulz, J. Schaefer, T. Zander, C. Heyn, and W. Hansen, *Appl. Phys. Lett.* **88**, 213107 (2006).
- [23] C. Walther, J. Bollmann, H. Kissel, H. Kirmse, W. Neumann, and W. Masselink, *Phys. B* **273-274**, 971 (1999).
- [24] M. Geller, *Appl. Phys. Rev.* **6**, 031306 (2019).
- [25] A. Luque, A. Marti, and C. Stanley, *Nat. Photon.* **6**, 146 (2012).
- [26] G. Gillard, I. Griffiths, G. Ragunathan, A. Ulhaq, C. McEwan, E. Clarke, and E. A. Chekhovich, *npj Quantum Inf.* **7**, 43 (2021).
- [27] D. V. Lang, *J. Appl. Phys.* **45**, 3023 (1974).
- [28] S. Anand, N. Carlsson, M.-E. Pistol, L. Samuelson, and W. Seiffert, *Appl. Phys. Lett.* **67**, 3016 (1995).
- [29] C. M. A. Kapteyn, F. Heinrichsdorff, O. Stier, R. Heitz, M. Grundmann, N. D. Zakharov, D. Bimberg, and P. Werner, *Phys. Rev. B* **60**, 14265 (1999).
- [30] S. Schulz, A. Schramm, C. Heyn, and W. Hansen, *Phys. Rev. B* **74**, 033311 (2006).
- [31] O. Engström, M. Kaniewska, M. Kaczmarczyk, and W. Jung, *Appl. Phys. Lett.* **91**, 133117 (2007).
- [32] L. Schnorr, T. Heinzel, S. Scholz, A. Ludwig, and A. D. Wieck, *J. Appl. Phys.* **124**, 104301 (2018).
- [33] L. Dobaczewski, P. Kaczor, I. D. Hawkins, and A. R. Peaker, *J. Appl. Phys.* **76**, 194 (1994).
- [34] G. Vincent, Ph.D. thesis, Université de Claude Bernard Lyon, Institut National des Sciences Appliquées, 1978.
- [35] R. H. Fowler and L. Nordheim, *Proc. Roy. Soc. Lond. A* **119**, 173 (1928).
- [36] See Supplemental Material at <http://link.aps.org/supplemental/10.1103/PhysRevB.104.035303> for details.
- [37] G. Snider, 1D Poisson, <https://www3.nd.edu/~gsnider/>, Accessed on Jun 9th, 2021.
- [38] J. W. Eaton, D. Bateman, S. Hauberg, and R. Wehbring, GNU Octave version 5.2.0 manual: a high-level interactive language for numerical computations, <https://octave.org/doc/v5.2.0/>, 2020.
- [39] S. Schulz, S. Schnüll, C. Heyn, and W. Hansen, *Phys. Rev. B* **69**, 195317 (2004).
- [40] D. S. Day, M. Y. Tsai, B. G. Streetman, and D. V. Lang, *J. Appl. Phys.* **50**, 5093 (1979).
- [41] A. Meurer, C. P. Smith, M. Paprocki, O. Čertík, S. B. Kirpichev, M. Rocklin, A. Kumar, S. Ivanov, J. K. Moore, S. Singh, T. Rathnayake, S. Vig, B. E. Granger, R. P. Muller, F. Bonazzi, H. Gupta, S. Vats, F. Johansson, F. Pedregosa, M. J. Curry *et al.*, *Peer J. Comput. Sci.* **3**, e103 (2017).
- [42] V. Korobov and V. Ochkov, *Chemical Kinetics with Mathcad and Maple* (Springer, Vienna, 2011).
- [43] G. Vincent, A. Chantre, and D. Bois, *J. Appl. Phys.* **50**, 5484 (1979).
- [44] J. Kerski, P. Lochner, A. Ludwig, A. D. Wieck, A. Kurzmann, A. Lorke, and M. Geller, *Phys. Rev. Appl.* **15**, 024029 (2021).

Electron capture and emission dynamics of self-assembled quantum dots far from equilibrium with the environment

L. Schnorr, J. Labes, L. Kürten, and T. Heinzel*

Solid State Physics Laboratory, Heinrich-Heine-Universität

Düsseldorf, 40204 Düsseldorf, Germany

C. Rothfuchs-Engels, S. Scholz, A. Ludwig, and A. D. Wieck

Lehrstuhl für Angewandte Festkörperphysik,

Ruhr-Universität Bochum, 44780 Bochum, Germany

Abstract

This supplement gives the analytical solution to the system of differential equations used in the discussion of the measured data alongside the Python-code used to calculate it, the calculated relationship between the applied bias voltage and the electric field at the quantum dot layer as well as the calculated relationship between the applied bias voltage and the Vincent correction factor for both s-states. Furthermore the measured current-voltage and capacitance-voltage characteristics are given.

I. SYMPY-CODE

The SymPy code to solve the system of differential equations is listed below.

The SymPy version used is 1.5.1-1p152.1.2.

The Python interpreter version used is 3.6.12-1p152.4.14.1.

The source code is also given in the file `saqd.py`.

```
1 from sympy import *
2
3 init_printing()
4
5 #Define symbols and functions:
6 t = Symbol('t', real=True, positive=True)
7
8 n_2 = Function('n_2')(t)
9 n_1 = Function('n_1')(t)
10 n_0 = Function('n_0')(t)
11
12 r21 = Symbol('r21', real=True, positive=True)
13 r10 = Symbol('r10', real=True, positive=True)
14 c = Symbol('c', real=True, positive=True)
15
16 #Define initial conditions:
17 N00 = Symbol('N00', real=True, positive=True)
18 N10 = Symbol('N10', real=True, positive=True)
19 N20 = Symbol('N20', real=True, positive=True)
20
21 #Define system of differential equations
22 eq0 = Eq(n_0.diff(), r10*n_1 - c*n_0)
23 eq1 = Eq(n_1.diff(), - r10*n_1 + c*n_0 + r21*n_2 - c*n_1)
24 eq2 = Eq(n_2.diff(), - r21*n_2 + c*n_1)
25
```

```

26 eq = (eq0, eq1, eq2)
27
28 #Solve the system:
29 result = dsolve(eq, ics={sympify('n_0(0)'):N00,sympify('n_1(0)'):N10,
    sympify('n_2(0)'):N20})
30
31 #Print Python code:
32 print("Results:")
33 print("n0:")
34 print((result[0].rhs))
35 print("n1:")
36 print((result[1].rhs))
37 print("n2:")
38 print((result[2].rhs))
39
40 print("\n")
41
42 #Print Latex code:
43 print(latex(result[0],long_frac_ratio=2))
44 print("\n")
45 print(latex(result[1],long_frac_ratio=2))
46 print("\n")
47 print(latex(result[2],long_frac_ratio=2))

```

This script prints the solution as Python-code and \LaTeX -code to the standard output. This output is given in the file `stdout.txt`.

II. SOLUTION

The analytical solutions for $n_0(t)$, $n_1(t)$ and $n_2(t)$ are given below for the initial conditions $n_0(0) = N_{00}$, $n_1(0) = N_{10}$ and $n_2(0) = N_{20}$.

$$\begin{aligned}
n_0(t) = & \frac{r_{10}r_{21}(N_{00} + N_{10} + N_{20})}{c^2 + cr_{21} + r_{10}r_{21}} + \frac{e^{t\left(-c - \frac{r_{10}}{2} - \frac{r_{21}}{2} + \frac{1}{2}\sqrt{4cr_{10} + r_{10}^2 - 2r_{10}r_{21} + r_{21}^2}\right)}}{4c(c^2 + cr_{21} + r_{10}r_{21})\sqrt{4cr_{10} + r_{10}^2 - 2r_{10}r_{21} + r_{21}^2}} \left(r_{10} \right. \\
& - r_{21} - \sqrt{4cr_{10} + r_{10}^2 - 2r_{10}r_{21} + r_{21}^2} \Big) \left(-2N_{00}c^3 - N_{00}c^2r_{10} - N_{00}c^2r_{21} \right. \\
& - N_{00}c^2\sqrt{4cr_{10} + r_{10}^2 - 2r_{10}r_{21} + r_{21}^2} - N_{10}c^2r_{10} + N_{10}c^2r_{21} \\
& - N_{10}c^2\sqrt{4cr_{10} + r_{10}^2 - 2r_{10}r_{21} + r_{21}^2} + 2N_{10}cr_{10}r_{21} + 3N_{20}cr_{10}r_{21} - N_{20}cr_{21}^2 \\
& + N_{20}cr_{21}\sqrt{4cr_{10} + r_{10}^2 - 2r_{10}r_{21} + r_{21}^2} + N_{20}r_{10}^2r_{21} - N_{20}r_{10}r_{21}^2 \\
& \left. + N_{20}r_{10}r_{21}\sqrt{4cr_{10} + r_{10}^2 - 2r_{10}r_{21} + r_{21}^2} \right) \\
& + \frac{e^{t\left(-c - \frac{r_{10}}{2} - \frac{r_{21}}{2} - \frac{1}{2}\sqrt{4cr_{10} + r_{10}^2 - 2r_{10}r_{21} + r_{21}^2}\right)}}{4c(c^2 + cr_{21} + r_{10}r_{21})\sqrt{4cr_{10} + r_{10}^2 - 2r_{10}r_{21} + r_{21}^2}} \left(r_{10} - r_{21} \right. \\
& + \sqrt{4cr_{10} + r_{10}^2 - 2r_{10}r_{21} + r_{21}^2} \Big) \left(2N_{00}c^3 + N_{00}c^2r_{10} + N_{00}c^2r_{21} \right. \\
& - N_{00}c^2\sqrt{4cr_{10} + r_{10}^2 - 2r_{10}r_{21} + r_{21}^2} + N_{10}c^2r_{10} - N_{10}c^2r_{21} \\
& - N_{10}c^2\sqrt{4cr_{10} + r_{10}^2 - 2r_{10}r_{21} + r_{21}^2} - 2N_{10}cr_{10}r_{21} - 3N_{20}cr_{10}r_{21} + N_{20}cr_{21}^2 \\
& + N_{20}cr_{21}\sqrt{4cr_{10} + r_{10}^2 - 2r_{10}r_{21} + r_{21}^2} - N_{20}r_{10}^2r_{21} + N_{20}r_{10}r_{21}^2 \\
& \left. + N_{20}r_{10}r_{21}\sqrt{4cr_{10} + r_{10}^2 - 2r_{10}r_{21} + r_{21}^2} \right) \\
& \quad \quad \quad (1)
\end{aligned}$$

$$\begin{aligned}
n_1(t) = & \frac{cr_{21}(N_{00} + N_{10} + N_{20})}{c^2 + cr_{21} + r_{10}r_{21}} + \frac{e^{t\left(-c - \frac{r_{10}}{2} - \frac{r_{21}}{2} - \frac{1}{2}\sqrt{4cr_{10} + r_{10}^2 - 2r_{10}r_{21} + r_{21}^2}\right)}}{4c(c^2 + cr_{21} + r_{10}r_{21})\sqrt{4cr_{10} + r_{10}^2 - 2r_{10}r_{21} + r_{21}^2}} \left(-2c \right. \\
& - r_{10} + r_{21} - \sqrt{4cr_{10} + r_{10}^2 - 2r_{10}r_{21} + r_{21}^2} \left. \right) \left(2N_{00}c^3 + N_{00}c^2r_{10} + N_{00}c^2r_{21} \right. \\
& - N_{00}c^2\sqrt{4cr_{10} + r_{10}^2 - 2r_{10}r_{21} + r_{21}^2} + N_{10}c^2r_{10} - N_{10}c^2r_{21} \\
& - N_{10}c^2\sqrt{4cr_{10} + r_{10}^2 - 2r_{10}r_{21} + r_{21}^2} - 2N_{10}cr_{10}r_{21} - 3N_{20}cr_{10}r_{21} + N_{20}cr_{21}^2 \\
& + N_{20}cr_{21}\sqrt{4cr_{10} + r_{10}^2 - 2r_{10}r_{21} + r_{21}^2} - N_{20}r_{10}^2r_{21} + N_{20}r_{10}r_{21}^2 \\
& \left. + N_{20}r_{10}r_{21}\sqrt{4cr_{10} + r_{10}^2 - 2r_{10}r_{21} + r_{21}^2} \right) \\
& + \frac{e^{t\left(-c - \frac{r_{10}}{2} - \frac{r_{21}}{2} + \frac{1}{2}\sqrt{4cr_{10} + r_{10}^2 - 2r_{10}r_{21} + r_{21}^2}\right)}}{4c(c^2 + cr_{21} + r_{10}r_{21})\sqrt{4cr_{10} + r_{10}^2 - 2r_{10}r_{21} + r_{21}^2}} \left(-2c - r_{10} + r_{21} \right. \\
& + \sqrt{4cr_{10} + r_{10}^2 - 2r_{10}r_{21} + r_{21}^2} \left. \right) \left(-2N_{00}c^3 - N_{00}c^2r_{10} - N_{00}c^2r_{21} \right. \\
& - N_{00}c^2\sqrt{4cr_{10} + r_{10}^2 - 2r_{10}r_{21} + r_{21}^2} - N_{10}c^2r_{10} + N_{10}c^2r_{21} \\
& - N_{10}c^2\sqrt{4cr_{10} + r_{10}^2 - 2r_{10}r_{21} + r_{21}^2} + 2N_{10}cr_{10}r_{21} + 3N_{20}cr_{10}r_{21} - N_{20}cr_{21}^2 \\
& + N_{20}cr_{21}\sqrt{4cr_{10} + r_{10}^2 - 2r_{10}r_{21} + r_{21}^2} + N_{20}r_{10}^2r_{21} - N_{20}r_{10}r_{21}^2 \\
& \left. + N_{20}r_{10}r_{21}\sqrt{4cr_{10} + r_{10}^2 - 2r_{10}r_{21} + r_{21}^2} \right) \\
& \quad \quad \quad (2)
\end{aligned}$$

$$\begin{aligned}
n_2(t) = & \frac{c^2(N_{00} + N_{10} + N_{20})}{c^2 + cr_{21} + r_{10}r_{21}} + \frac{e^{t\left(-c - \frac{r_{10}}{2} - \frac{r_{21}}{2} + \frac{1}{2}\sqrt{4cr_{10} + r_{10}^2 - 2r_{10}r_{21} + r_{21}^2}\right)}}{2(c^2 + cr_{21} + r_{10}r_{21})\sqrt{4cr_{10} + r_{10}^2 - 2r_{10}r_{21} + r_{21}^2}} \left(-2N_{00}c^3 \right. \\
& - N_{00}c^2r_{10} - N_{00}c^2r_{21} - N_{00}c^2\sqrt{4cr_{10} + r_{10}^2 - 2r_{10}r_{21} + r_{21}^2} - N_{10}c^2r_{10} + N_{10}c^2r_{21} \\
& - N_{10}c^2\sqrt{4cr_{10} + r_{10}^2 - 2r_{10}r_{21} + r_{21}^2} + 2N_{10}cr_{10}r_{21} + 3N_{20}cr_{10}r_{21} - N_{20}cr_{21}^2 \\
& + N_{20}cr_{21}\sqrt{4cr_{10} + r_{10}^2 - 2r_{10}r_{21} + r_{21}^2} + N_{20}r_{10}^2r_{21} - N_{20}r_{10}r_{21}^2 \\
& \left. + N_{20}r_{10}r_{21}\sqrt{4cr_{10} + r_{10}^2 - 2r_{10}r_{21} + r_{21}^2} \right) \\
& + \frac{e^{t\left(-c - \frac{r_{10}}{2} - \frac{r_{21}}{2} - \frac{1}{2}\sqrt{4cr_{10} + r_{10}^2 - 2r_{10}r_{21} + r_{21}^2}\right)}}{2(c^2 + cr_{21} + r_{10}r_{21})\sqrt{4cr_{10} + r_{10}^2 - 2r_{10}r_{21} + r_{21}^2}} \left(2N_{00}c^3 + N_{00}c^2r_{10} + N_{00}c^2r_{21} \right. \\
& - N_{00}c^2\sqrt{4cr_{10} + r_{10}^2 - 2r_{10}r_{21} + r_{21}^2} + N_{10}c^2r_{10} - N_{10}c^2r_{21} \\
& - N_{10}c^2\sqrt{4cr_{10} + r_{10}^2 - 2r_{10}r_{21} + r_{21}^2} - 2N_{10}cr_{10}r_{21} - 3N_{20}cr_{10}r_{21} + N_{20}cr_{21}^2 \\
& + N_{20}cr_{21}\sqrt{4cr_{10} + r_{10}^2 - 2r_{10}r_{21} + r_{21}^2} - N_{20}r_{10}^2r_{21} + N_{20}r_{10}r_{21}^2 \\
& \left. + N_{20}r_{10}r_{21}\sqrt{4cr_{10} + r_{10}^2 - 2r_{10}r_{21} + r_{21}^2} \right) \\
& \quad \quad \quad (3)
\end{aligned}$$

III. ELECTRIC FIELD

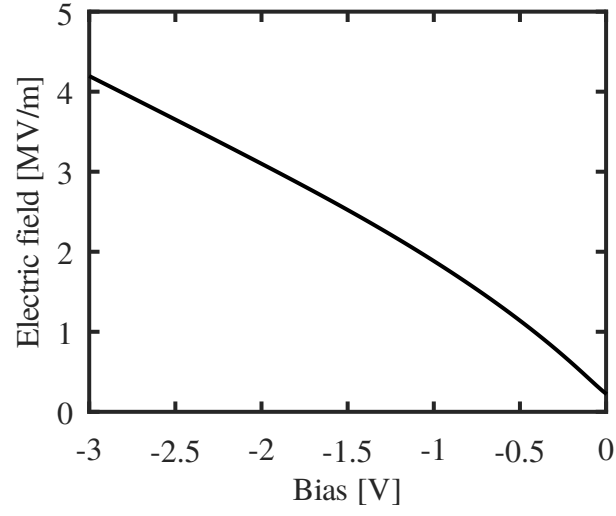


FIG. 1. Calculated relationship between the applied bias voltage and the electric field strength at the SAQD layer at $T = 77$ K.

IV. VINCENT CORRECTION

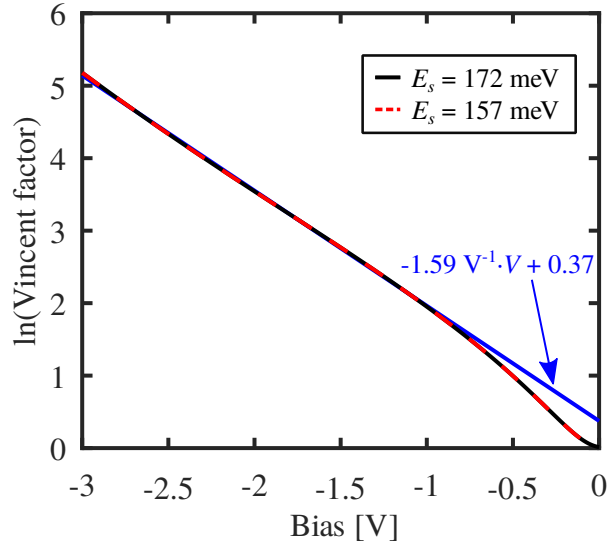


FIG. 2. Calculated relationship between the applied bias voltage and the natural logarithm of the Vincent correction factor expected for the SAQD s-states at $T = 77$ K. A linear approximation for $V < -1.0$ V where measurement signals could be observed shows excellent agreement.

V. IV CHARACTERISTICS

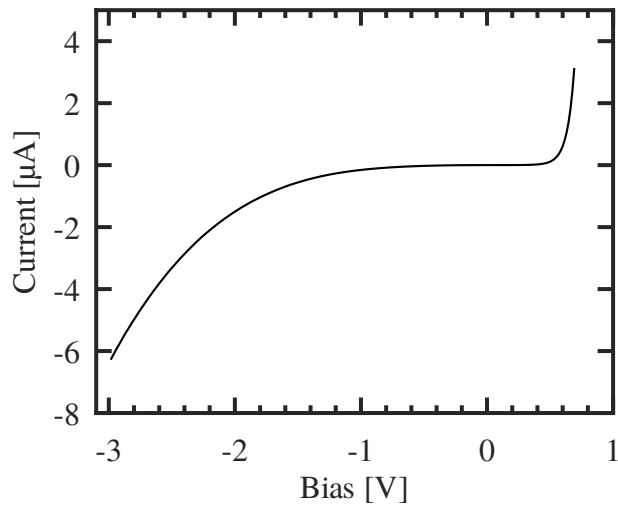


FIG. 3. Plot of the DC current-voltage characteristics at $T = 77$ K.

VI. CV-ANALYSIS

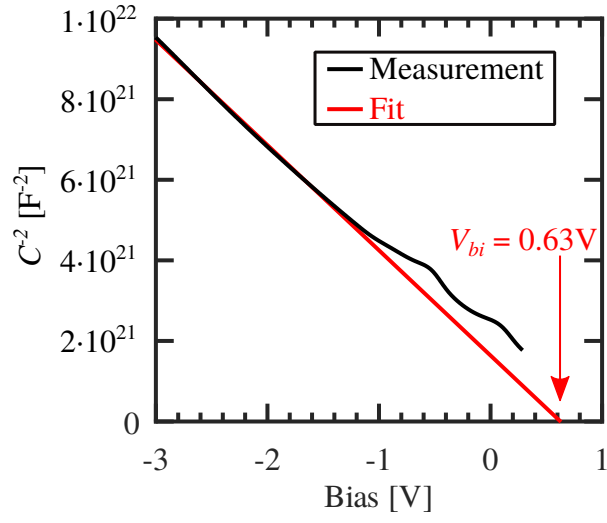


FIG. 4. Plot of the squared inverse sample capacitance as a function of the applied bias voltage at $T = 77$ K. A linear fit over the region $V < -1.3$ V where the SAQDs are empty yields a barrier height of $V_{bi} = 0.63$ V.

* thomas.heinzel@hhu.de

Chapter 6

CV-Hysteresis at low temperatures

6.1 Context

Hysteretic behavior of SAQDs as a function of the applied bias voltage is well known [55,56,60,62,65,144,145] and has been observed via capacitive measurement techniques [55–58]. In SAQDs embedded into a Schottky structure a hysteretic CV can be related to a difference in the amount of charge that is stored inside the SAQD layer between the up- and down-sweeps [86].

The amount of charge stored inside the dots depends on the charging and discharging dynamics as a function of the bias voltage. After these dynamics were measured and the resulting charge distributions modeled at $T = 77$ K the next goal of this thesis was to adapt this approach to lower temperatures and use its results to predict the hysteretic capacitance voltage relationship that can be observed at low temperatures. The increased resolution due to the larger time constants at lower temperatures and the more pronounced bias voltage dependence that is no longer overshadowed by thermal emission allowed for significantly more insight than the measurements at $T = 77$ K. It was possible to clearly resolve the emission from the s-, p- and d-state of the SAQDs and, for the first time in these structures, observe charge state dependent capture rates. The model used to describe the dynamics thus had to be extended and was subsequently only solvable numerically. Exemplary the dynamics at $T = 7$ K have been modeled and as one key result it could be shown that the capture rates get smaller the more charge is stored inside the dots.




From the model the hysteretic capacitance voltage relationship could indeed be predicted in good agreement with the measurement. A continuous time [146] Markov chain [147] model can predict the time dependence of the system at experimentally inaccessible time scales.

The results have been published in a peer reviewed international journal and are included in this thesis as Paper 3.



6.2 Paper 3

PHYSICAL REVIEW B **104**, 205310 (2021)

Hysteretic capacitance-voltage characteristics of self-assembled quantum dots far from equilibrium with their environment

L. Schnorr , O. Khoukhi, L. Berg , and T. Heinzel *

Solid State Physics Laboratory, Heinrich-Heine-Universität Düsseldorf, 40204 Düsseldorf, Germany

C. Rothfuchs-Engels,[†] S. Scholz, A. Ludwig , and A. D. Wieck 

Lehrstuhl für Angewandte Festkörperphysik, Ruhr-Universität Bochum, 44780 Bochum, Germany



(Received 22 September 2021; revised 15 November 2021; accepted 16 November 2021; published 29 November 2021)

Capacitance-voltage measurements on self-assembled quantum dot layers exposed to strong electric fields and with large distances to the reservoirs show a marked hysteretic behavior. It is shown that at low temperatures this hysteresis can be explained quantitatively in terms of state-dependent capture and emission rates that are obtained by a rate equation model, applied to the measured capacitance transients. The occupation dynamics and the steady-state configuration can be extracted from these data via a Markov chain model.

DOI: [10.1103/PhysRevB.104.205310](https://doi.org/10.1103/PhysRevB.104.205310)

Reference

L. Schnorr, O. Khoukhi, L. Berg, T. Heinzel, C. Rothfuchs-Engels, S. Scholz, A. Ludwig, and A. D. Wieck Phys. Rev. B **104**, 205310 (2021)

DOI: <https://doi.org/10.1103/PhysRevB.104.205310>

©2021 American Physical Society






Copyright statement

The author has the right to use the article or a portion of the article in a thesis or dissertation without requesting permission from APS, provided the bibliographic citation and the APS copyright credit line are given on the appropriate pages.

Contributions

I planned all and conducted most of the experiments and analyzed all data. I contributed to the manuscript writing.

Hysteretic capacitance-voltage characteristics of self-assembled quantum dots far from equilibrium with their environment

L. Schnorr , O. Khokhi, L. Berg , and T. Heinzel ^{*}*Solid State Physics Laboratory, Heinrich-Heine-Universität Düsseldorf, 40204 Düsseldorf, Germany*C. Rothfuchs-Engels,[†] S. Scholz, A. Ludwig , and A. D. Wieck *Lehrstuhl für Angewandte Festkörperphysik, Ruhr-Universität Bochum, 44780 Bochum, Germany*

(Received 22 September 2021; revised 15 November 2021; accepted 16 November 2021; published 29 November 2021)

Capacitance-voltage measurements on self-assembled quantum dot layers exposed to strong electric fields and with large distances to the reservoirs show a marked hysteretic behavior. It is shown that at low temperatures this hysteresis can be explained quantitatively in terms of state-dependent capture and emission rates that are obtained by a rate equation model, applied to the measured capacitance transients. The occupation dynamics and the steady-state configuration can be extracted from these data via a Markov chain model.

DOI: [10.1103/PhysRevB.104.205310](https://doi.org/10.1103/PhysRevB.104.205310)

I. INTRODUCTION

Self-assembled quantum dots (SAQDs) are quasi-zero-dimensional semiconductor islands embedded in a crystalline semiconductor host [1,2]. Due to the electronic band offsets, they are capable of capturing, storing, and re-emitting electrons or holes, respectively. SAQDs have been of great scientific interest over the past three decades due to their versatility for fundamental research [3–6] as well as because of their application potential [7]. SAQDs are used routinely in semiconductor optoelectronics, in particular in quantum dot lasers [8,9], single photon sources [10], and light-emitting diodes [11]. Regarding all-electronic applications like memory cells [12–14] or memristors [15], it is well known that the charging/discharging dynamics of SAQDs can generate hysteretic behavior as a function of a bias voltage [16–22], detectable, for example, in the capacitance of the structure [21–24] or in the conductance of a nearby conductive channel, on which the SAQDs act as a floating gate [14,18–20,22,25–29]. Charging/discharging times of 600 ps have been reported [30], while the storage time depended strongly on the temperature and can reach values of 10^4 s at a temperature of 180 K [13]. The markedness of the hysteresis depends, in general, on the modifications of the potential landscape accompanied by the electron transfer [28,31]. For several experiments, these modifications were described qualitatively and with high plausibility [18,19,21–24]. However, to understand these hysteretic effects in more detail, a quantitative description is desirable. In particular, it is important to be able to determine the capture and emission rates of the SAQD states as a function of the external parameters. Such information can be useful not only to explain certain phenomena in more detail, like the inversion of the hysteresis orientation above

a threshold bias [32] or nontrivial shapes of hysteresis loops [20], but also to improve characteristic values, for example, the limits for ultrafast charging of SAQDs [33], relevant for single-photon sources.

Here, we present an experimental concept which allows the determination of the bias voltage-dependent (and temperature-dependent) capture and emission rates of the SAQD states that take part in the hysteresis. The SAQDs are in states far from equilibrium with the environment due to the strong electric field and large distances to reservoirs prevent corresponding elastic electron transfers. Such a layout is typical for memory devices as well as for optoelectronic applications. Deep level transient spectroscopy (DLTS, [34]), a well-established technique in the field [35–44], is used in its version of *Lock in-DLTS* [45], as an excellent compromise between high-energy resolution and acceptable measurement times. A rate equation model allows to extract the electron transfer rates of the participating states from the measured capacitance transients. From these rates, the average electron occupation numbers of the SAQDs as a function of time are determined. They not only provide an explanation in terms of the corresponding depletion region width z_d , but also describe the measured hysteresis loop quite well and allow the prediction of the steady-state configuration in the limit of negligible voltage sweep rates.

In Sec. II, the sample and the experimental methods are described. Section III reports the DLTS measurements, which are analyzed within the rate equation model in Sec. IV. These results are used in Sec. V for the modeling and explanation of the capacitance voltage hysteresis, and in Sec. VI for calculating the steady state. The paper concludes with a summary and an outlook (Sec. VII).

II. EXPERIMENTAL SETUP AND MEASUREMENT TECHNIQUES

The sample structure and the measurement technique were described in detail elsewhere [43,44]. In brief, we use a

^{*}thomas.heinzel@hhu.de[†]Present address: DESY, Notkestrasse 85, 22607 Hamburg, Germany.

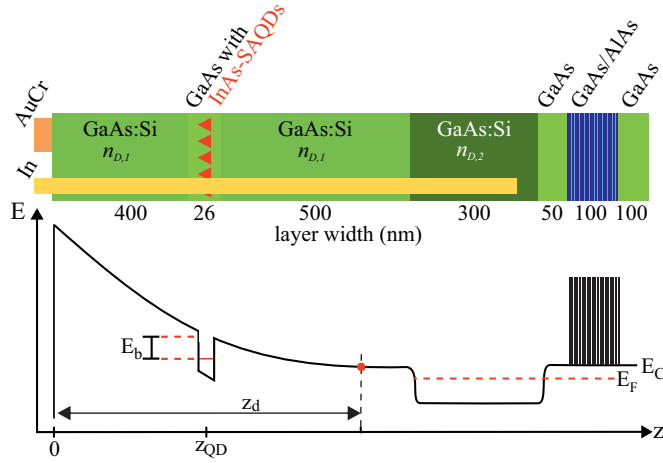


FIG. 1. Top: Cross-sectional schematic view of the sample layout. The SAQD layer is indicated by the red triangles. The back electrode is accessed via an alloyed In contact, and the top gate is formed by a Cr/Au electrode. Silicon doping densities are indicated by $n_{D,1}$ and $n_{D,2}$. Bottom: Schematic band diagram for the case of a negative voltage applied to the top gate with respect to the grounded back electrode, including our conventions for the quantities of relevance. The width of the depletion layer is denoted by z_d .

GaAs/AlAs heterostructure as a model system, grown by molecular beam epitaxy, with a SAQD layer 500 nm above a Si^+ -doped back contact and 426 nm below the sample surface, see Fig. 1(a). The InAs SAQDs have a sheet number density of $n_{QD} = 10^{14} \text{ m}^{-2}$ and are embedded in a 26-nm layer of undoped GaAs. Bias voltages can be applied between a square Cr/Au top electrode (edge length 0.3 mm) and the back electrode, which is accessed via an alloyed In contact. The densities of the Si doping in the spacer layers are $n_{D,1} = 6.02 \times 10^{21} \text{ m}^{-3}$ and $n_{D,2} = 2 \times 10^{24} \text{ m}^{-3}$. The active sample area covers approximately 9×10^6 quantum dots.

The sample is inserted into a liquid helium cryostat with a temperature range from 3 K to 300 K. DC bias voltages are applied to the top gate with respect to the back contact, kept at virtual ground via a HF2TA transimpedance amplifier ($Z = 1 \text{ k}\Omega$) from Zurich Instruments, the output of which is fed into a Zurich Instruments HF2LI lock in amplifier. The voltage pulses are generated using a Keithley Model 3390 arbitrary waveform generator with a transition time of 100 ns and are superimposed to the AC test voltage generated by the lock in amplifier. Thus, the output current obtained at a phase shift of $\pi/2$ with respect to the input AC voltage detects the differential capacitance of the sample.

III. EXPERIMENTAL RESULTS

A. Capacitance-voltage measurements and their temperature dependence

Multiple capacitance-voltage sweeps between $V = -4 \text{ V}$ and $V = +0.3 \text{ V}$ were recorded at various temperatures between $T = 7 \text{ K}$ and room temperature. For each temperature both the up- and down-sweeps were measured. The bias voltage step size was $\Delta V = 12.5 \text{ mV}$ with a waiting time of $\Delta t = 0.85 \text{ s}$ and the capacitance was measured via a test

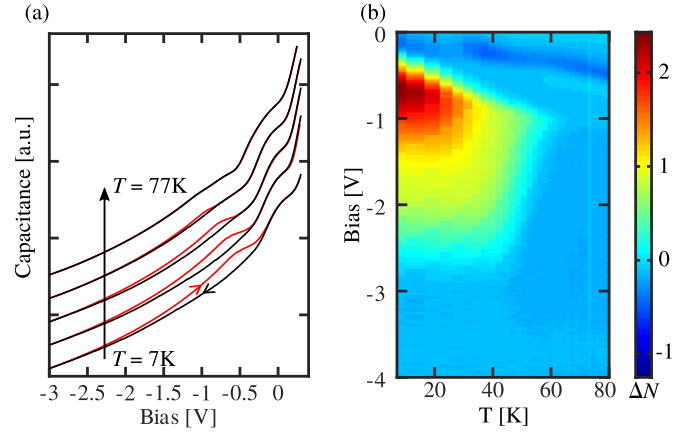


FIG. 2. (a) Capacitance-voltage hysteresis as a function of temperature with red and black lines corresponding to the up- and down-sweeps, respectively. The temperature values are (from bottom to top) $T = 7 \text{ K}$, 22 K , 33 K , 52 K , and 77 K . Adjacent traces are offset vertically for clarity. (b) Difference of the number of electrons stored per SAQD between the up- and down-sweep as a function of the bias voltage and temperature.

signal with an amplitude of $V_{ac} = 10 \text{ mV}$ and a frequency of $f_{ac} = 10.44 \text{ MHz}$. The lock in time constant was set to $\tau = 20.33 \text{ ms}$. A selection of these traces is shown in Fig. 2(a).

As the bias voltage is increased from $V = -4 \text{ V}$ to $V = +0.3 \text{ V}$ at $T = 7 \text{ K}$ [lower-most trace in Fig. 2(a)], two peaks can be observed on top of the smooth voltage dependence expected for a Schottky diode capacitance, one at $V \approx -0.6 \text{ V}$ and a second one at $V = 0 \text{ V}$. In the successive down-sweep, however, only the peak at $V = 0 \text{ V}$ is observed, while the second one is absent. A similar behavior was reported in earlier work [13,24,46]. This hysteretic behavior is the main focus of the present work.

As the temperature is increased, both features shift towards lower bias voltages. The hysteretic peak becomes weaker until it vanishes at about $T = 60 \text{ K}$. The nonhysteretic peak, however, becomes more pronounced as the temperature is increased up to $T \approx 150 \text{ K}$ above which its shape and position remain essentially unchanged (not shown).

In Fig. 2(b), the difference ΔN in the number of electrons stored per SAQD between the up- and down-sweeps is shown as a function of the bias voltage and the temperature, see Sec. V for details. The maximum hysteresis opening thus corresponds to a charge difference of more than two electrons per SAQD at low temperatures. Qualitatively, its origin can be described as follows [24]. At sufficiently negative bias voltages V the SAQDs are empty. As V is increased, the width z_d of the space charge layer decreases according to $z_d = \sqrt{\frac{2\epsilon\epsilon_0}{en_D}(V_{bi} - V)}$, where V_{bi} is the built-in voltage and e denotes the elementary charge. This leads to an increase of the capacitance according to $C = \epsilon\epsilon_0 A/z_d$, where A denotes the area underneath the top gate, which causes the smooth increase of C with V . Above a threshold voltage, electrons are captured at a significant rate by the SAQDs, leading to an average electron number N per SAQD. This causes an increase of z_d since these electrons have to be compensated

by additional positively charged donor ions [46]

$$z_d(N) = \sqrt{\frac{2}{en_D} [\epsilon\epsilon_0(V_{bi} - V) + Nen_{QD}z_{QD}]} \quad (1)$$

As a consequence, the capacitance decreases to $C = \epsilon\epsilon_0 A/z_d(N)$ when the steady state is reached. During our up-sweeps and in the hysteresis interval, however, the sweep rate is comparable to or larger than the smallest charge transfer rate, and the steady state has not yet been reached. Consequently, a larger capacitance as compared to the steady-state value is measured. Likewise, in a down-sweep, the measured capacitance can be smaller than its steady-state value. Therefore, one expects to observe characteristic capacitance transients in response to voltage steps with positive (negative) sign for negative (positive) voltage steps and with time constants that depend on the capture and emission rates of the participating SAQD states. As we will show below, the relation between the time constants of the transients and the state-dependent electron transfer rates is nontrivial but explains the hysteresis in quantitative terms.

B. Lock in: DLTS measurements

We determine the electron transfer rates from capacitance transients of the sample in response to abrupt voltage steps. The transients are characterized by lock in-DLTS measurements at four selected temperatures, namely at $T = 7$ K, 16 K, 41 K, and 77 K. Measurement voltages $V_m \in [-3.0$ V, 0 V] were applied after preparation voltages V_p . Each voltage was applied for a time interval $t_p = t_m = 498$ ms. Measurements were recorded for combinations of V_p and V_m over the measurement interval with a voltage step size of $\Delta V = 40$ mV. Afterwards, the lock in signal $S(V_p, V_m)$ was calculated according to

$$S(V_p, V_m) = \sum_{i=1}^{N_t/2} C(t_i, V_p, V_m) - \sum_{i=N_t/2+1}^{N_t} C(t_i, V_p, V_m), \quad (2)$$

where N_t is the number of time samples in the recorded transient. Thus, the lock in signal represents the difference of the areas in the first and the second half of the transient. It approaches zero for time constants much smaller or much larger than the measurement window and shows a maximum for a time constant of $\approx 40\%$ of the evaluated recording time [44]. The results are shown in Fig. 3.

At $T = 7$ K, three clearly separated negative emission peaks can be observed at $V_p > -0.5$ V for $V_m \approx -2.55$ V, $V_m \approx -1.2$ V, and $V_m \approx -0.4$ V. All emission peaks are approximately symmetric with respect to V_m . For $V_p < -0.5$ V, electron capture can be observed via a positive lock in-DLTS signal at $V_m \approx (-0.4 \pm 0.1)$ V. Outside of the transition region from electron emission to capture at $V_p \approx -0.5$ V the emission peaks do not exhibit any dependence on V_p . The capture peak, however, shows a step-like dependence on V_p on its border towards smaller V_m with two steps occurring at approximately $V_p = -1.25$ V and $V_p = -2.4$ V.

At $T = 16$ K, the features remain qualitatively unchanged, with the capture and emission signals at the largest V_m values shifting towards smaller V_m . The transition region between the capture and emission regimes has decreased to $V_p \approx -0.6$ V.

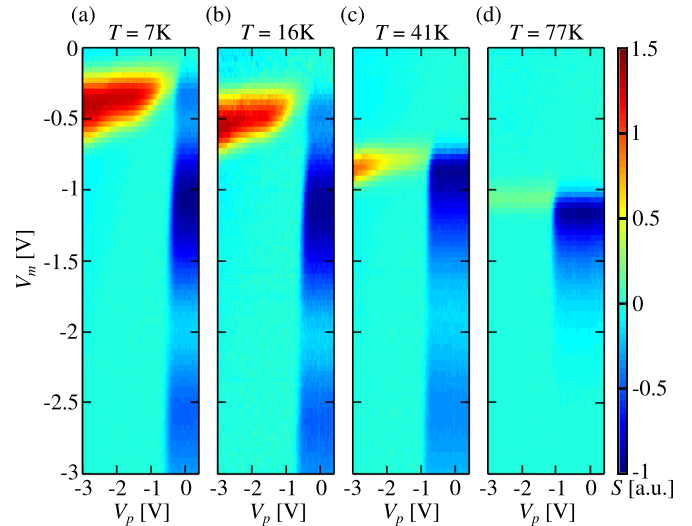


FIG. 3. Lock in-DLTS measurements at $T = 7$ K, 16 K, 41 K, and 77 K (a)–(d). The colorscale value of each spectrum is scaled to -1 at its respective minimum.

At $T = 41$ K, however, the changes are more pronounced: only two emission peaks can be observed, a large one that is asymmetric with respect to V_m as well as an approximately symmetric one centered at $V_m \approx -2.55$ V, separated by a minimum at $V_m \approx -0.9$ V. The capture signal is significantly weaker compared to those at lower temperatures and now covers the interval $V_m \in [-1$ V, -0.75 V]. A slight dependence of its low-voltage edge on V_p can still be observed, but the resolution is too small to identify the steps here. The transition region between the capture and emission regimes has shifted downwards to $V_p \approx -0.9$ V.

Only one asymmetrical emission signal can be observed at $T = 77$ K, which has its minimum at $V_m \approx -1.2$ V. A relatively weak capture signal at $V_m \approx -1.05$ V can still be detected. Neither the capture nor the emission peaks show a V_p dependence outside the transition region that has now shifted to $V_p \approx -1$ V.

Thus, a monotonous behavior of the temperature dependence is observed: as the T increases, the capture signal becomes less pronounced compared to the strongest respective emission peak, while its position moves in the direction of smaller V_m . The transition region between electron capture and emission shifts towards smaller V_p as T is increased. The fine-structure of both the capture and emission signals smear out as T increases. Furthermore, no emission signals can be observed at measurement voltages larger than the upper boundary of the capture structure on the V_m axis.

In the following, we restrict ourselves to an analysis of the situation at the lowest temperature, where the richest structure is observed and the emission occurs by elastic tunneling only. A quantitative discussion of the behavior at larger temperatures, where thermally activated processes are significant, is beyond our scope here and will be provided elsewhere.

IV. RATE EQUATION MODEL

To analyze quantitatively the observed lock in-DLTS signals taken at $T = 7$ K, we proceed by modeling the charge

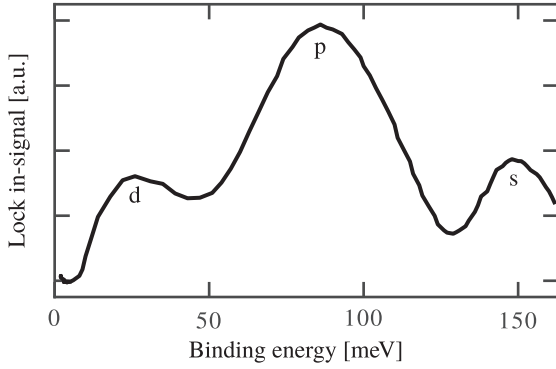


FIG. 4. Energy spectrum obtained from the emission features observed at $T = 7$ K, calculated via Eq. (3).

transfer dynamics by a system of coupled differential equations [47].

A. Rate equations for the electron transfer dynamics

Based on previous measurements on the same sample [43] we attribute the emission feature observed at $V_m \approx -2.6$ V at $T = 7$ K to electron emission from the s -states.

In analogy to the analysis described in Ref. [43], the energy spectrum can be calculated from the emission transients, but now at temperatures where elastic tunneling is dominant. Via the relationship derived by Korol *et al.* [48], the time constant of the capacitance transient is given by

$$\tau = \frac{4\sqrt{2m^*E_b}}{eF} \exp\left(\frac{4}{3} \frac{\sqrt{2m^*E_b}^{3/2}}{e\hbar F}\right). \quad (3)$$

Here, E_b is the binding energy of the captured electrons (see also Fig. 1) and F denotes the electric field at the SAQD layer. The spectrum shown in Fig. 4 can be obtained by taking a line scan through the lock in–DLTS colorscale plot, Fig. 3(a), at $V_p = 0$. The voltage dependence in the obtained spectrum $S(V_m)$ can be converted into an electric field-dependent spectrum $S(F)$ via the voltage-dependent band structure of the sample as obtained from a one-dimensional Poisson-Schrödinger solver [49]. This electric field dependence is then converted into energy and presented in Fig. 4 by solving numerically Eq. (3) for the binding energy E_b with $\tau = \text{const.} = 0.398 \cdot t_m = 198$ ms, fixed by our transient recording time and the rate window of lock in signal.

The large energy spacing of ≈ 60 meV between the peaks, as well as their relative magnitude indicate that they originate from the s (smallest V_m), p , and d (largest V_m) states. Sublevels like s_1, s_2, p_1 , and so on cannot be resolved here. We therefore assume that the step-like structure of the capture peak arises from a superposition of three different capture paths, one for the s , p , and d states each. This gives rise to the system of coupled differential equations:

$$\dot{w}_0 = -c_{0s} \cdot w_0 + r_{s0} \cdot w_s, \quad (4)$$

$$\dot{w}_s = -c_{sp} \cdot w_s + r_{ps} \cdot w_p + c_{0s} \cdot w_0 - r_{s0} \cdot w_s, \quad (5)$$

$$\dot{w}_p = +c_{sp} \cdot w_s - r_{ps} \cdot w_p + r_{dp} \cdot w_d - c_{pd} \cdot w_p, \quad (6)$$

$$\dot{w}_d = +c_{dp} \cdot w_p - r_{dp} \cdot w_d, \quad (7)$$

TABLE I. Fit parameters used to calculate the results shown in Figs. 5(b), 5(c), and 6.

x	y	$m_{xy} [\text{V}^{-1}]$	n_{xy}	$m_{yx} [\text{V}^{-1}]$	n_{yx}
0	s	13.53	8.63	−6.15	−14.08
s	p	16.18	7.71	−4.97	−4.16
p	d	15.68	6.35	−16.66	−2.91

where w_0 is the probability for one SAQD being empty, while w_j is the probability that state j and all states at lower energies are occupied, while all states with larger energies are empty. The capture and emission rates related to these occupation probabilities are denoted by c_{ij} and r_{ij} , $i, j \in \{0, s, p, d\}$, respectively.

The total, time-dependent occupation number per dot is then given by

$$N(t) = 2 \cdot w_s(t) + 6 \cdot w_p(t) + 12 \cdot w_d(t). \quad (8)$$

Here, the weighting factors rely on the assumption that all sublevels of each SAQD state, e.g., the p state, share the same occupancy for all times. Other reasonable assumptions are possible as well which, however, cause only marginal changes of the fit parameters discussed below (not shown).

B. Fit of the experimental transients

We proceed by fitting the rate equation model to the data using a similar approach as reported earlier [44], where the choice of the initial conditions for the differential equations and the simulation of the pulse sequences are kept the same. The individual electron transfer rates are modeled by

$$c_{xy}(V) = \exp(m_{xy} \cdot V + n_{xy}) s^{-1}, \quad (9)$$

$$r_{yx}(V) = \exp(m_{yx} \cdot V + n_{yx}) s^{-1}, \quad (10)$$

where $x, y \in \{0, s, p, d\}$.

The lock in signal is calculated via Eq. (2) from the total charge per dot under the assumption that $\text{red } \Delta C(t) \propto N(t)$. The constants m_{xy} and n_{xy} are the fit parameters, alongside a scaling factor that accounts for the proportionality between $N(t)$ and $\Delta C(t)$.

Equations (4) to (7) have no analytical solution. We thus solve them numerically for each iteration of the fitting process, using the RADAU solver of the SCIPY library [50] which implements a fifth-order implicit Runge-Kutta method [51].

To avoid excessive computation times, the calculated rates were limited to $\leq 10^3 \text{ s}^{-1}$. This cutoff is justified by the recording time of $t_m = 498$ ms, which leads to a rate window of the lock in signal that is centered around $r_{\text{ref}} = (0.398 \cdot t_m)^{-1} = 5.1 \text{ s}^{-1}$, more than two orders of magnitude smaller.

The results of this fit algorithm are given in Table I, and the corresponding, numerically obtained lock in–DLTS signals are shown in comparison to the experimental data in Figs. 5(a) and 5(b). The resulting capture and emission rate functions are depicted in Fig. 5(c). Starting from a negative bias voltage, say $V = -3$ V, all emission rates are large as compared to the capture rates, and the SAQDs are empty in a steady state. As V is increased, the emission rates decay exponentially while significant capture sets in around $V = -1$ V. The capture rates

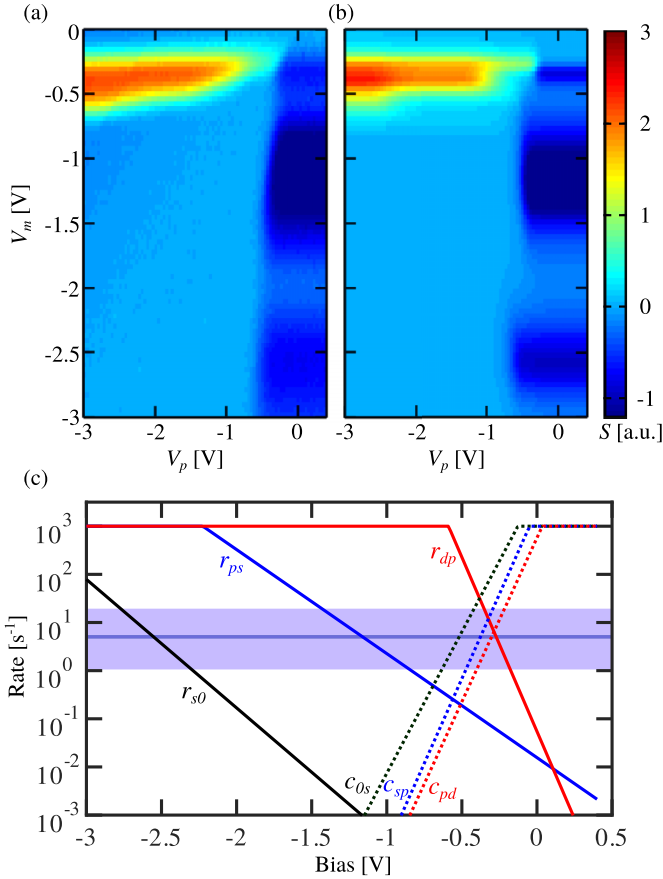


FIG. 5. (a) Measured and (b) calculated lock in-DLTS spectra for the measurement at $T = 7$ K and the voltage-dependent electron transfer rates (c), as obtained from the fit.

increase exponentially with increasing bias voltage, leading to an occupied steady state, with an occupation probability $w_j(V)$ (see below).

For the emission processes, the physical interpretation of the obtained fit parameters is straightforward: each exponential voltage dependence, parameterized by its two fit parameters, is an approximation to the general expression describing the emission dynamics, which in our case of $T = 7$ K consists of pure tunneling, Eq. (3). This approximation is valid in the voltage interval in which the resulting emission rate falls within the rate window of $r_{\text{ref}} = 5.1 \text{ s}^{-1}$ of our lock in-DLTS filter function. This value is denoted by the purple horizontal line in Fig. 5(c) alongside the corresponding full width at half maximum interval (indicated by the shaded area). We note that, only in this interval, our simple assumption of the respective rates as a function of the bias voltage needs to approximate the real dependence since outside this window the contribution to the measured signal is negligible. For the capture processes, we envisage a similar interpretation, but to the best of our knowledge, a model for the capture dynamics of electrons under the conditions present here is yet to be developed. It should be noted that the shape of the capture peak can only be reproduced accurately as long as $c_s > c_p > c_d$. Other scenarios lead to a qualitatively different shape (not shown). This may be indicative of the Coulomb barrier set up by the electrons already captured in the SAQDs, which (while

the system remains at the same bias voltage) suppresses the capture of further electrons. Thus, the dynamics of the capture processes cannot be dominated by the tunneling barrier width in our case. This finding is in contrast to the observations by Luyken *et al.* [52] who measured larger transfer rates for higher SAQD states which they were able to explain via the increased tunneling coefficient through the smaller potential barrier. Their measurements, however, studied each SAQD state at bias voltages where the respective state was aligned with the Fermi level in the back contact and the difference between charging and discharging times was negligible to a good approximation. Our measurements, however, are carried out with the states well above the bulk Fermi level and far from equilibrium with the environment, where capture and emission rates can differ by orders of magnitudes, see Fig. 5(c).

Based on these findings, we can now interpret qualitatively the behavior at higher temperatures. The shift of the capture peak towards smaller V_m in Fig. 3 with increasing temperature is indicative of increasing capture rates. Since they become larger as V is increased, the shift of the peaks towards more negative V_m compensates the increased thermal contribution, such that the combined rate still matches our experimental rate window. The same line of arguing is applicable to the emission peaks. The measured charge transfer rates are, however, composed of the individual transfer rates in a nontrivial way [44], where the observed decay rates are never smaller than each individual charge transfer rate. This explains the asymmetry of emission peaks close to the capture peaks in the lock in-DLTS spectra since, for larger V_m than the position of the capture peaks, there will always be a capture rate larger than any emission rate that will dominate the dynamics and make it too fast to be observable.

V. APPLICATION TO THE CV HYSTERESIS

We continue by solving the system of differential Eqs. (4) to (7) using the previously determined fit parameters for the slowly varying bias voltage that was applied during the measurement of the CV hysteresis.

The system is solved numerically for two sweep cycles, each from $V = +0.3 \text{ V}$ to $V = -4 \text{ V}$ and back, with the initial condition that all SAQDs are completely filled. The bias voltage is stepped by $\Delta V = \pm 12.5 \text{ mV}$ (depending on the sweep direction) every $\Delta t = 0.85 \text{ s}$. The calculation is considered to be finished when the solution has become independent of the initial condition.

From these simulations, the occupation probability of the SAQD states $w_j(V)$ for the down- and up-sweep is obtained, where $j \in \{0, s, p, d\}$, leading directly to a computed value for $\Delta N(V)$. Experimentally, $\Delta N(V)$ can be obtained from the measured CV hysteresis opening via the relation [46]

$$\Delta N = \frac{(\epsilon_0 \epsilon A)^2 n_D \cdot n_{QD}}{2z_{QD}} (C_{\text{down}}^{-2} - C_{\text{up}}^{-2}), \quad (11)$$

where A is the gate area and $C_{\text{down(up)}}$ the capacitance in a down (up)-sweep.

The corresponding computed and experimentally determined results are compared in Fig. 6(a). Reasonable agreement is found, both with respect to its magnitude and

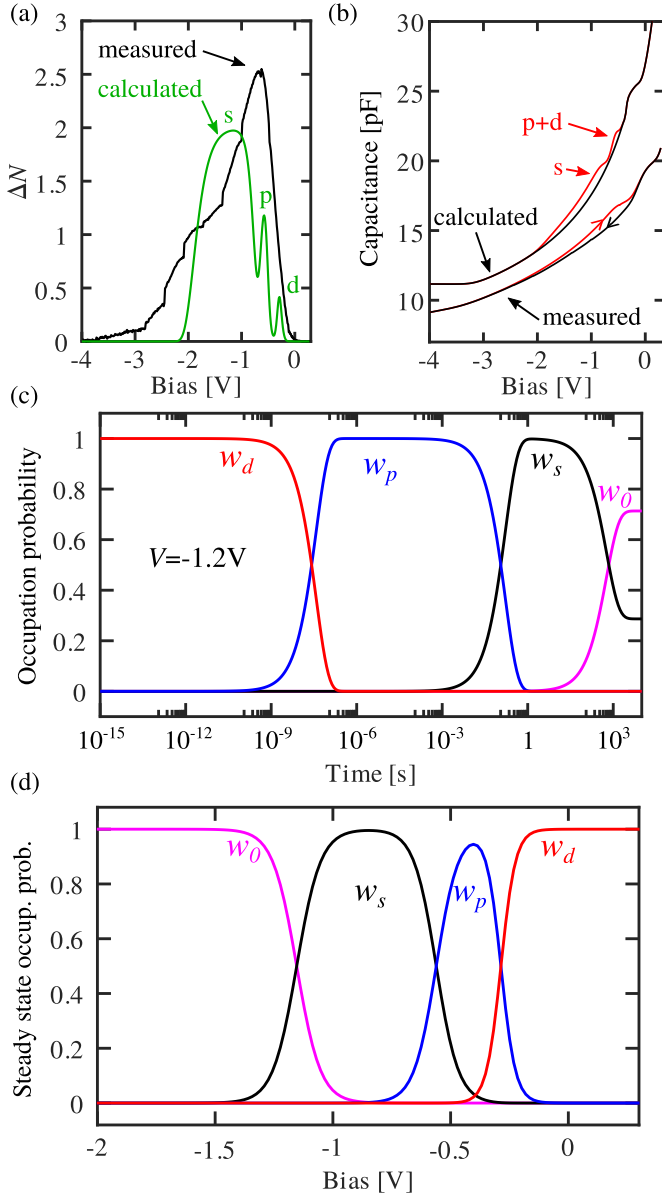


FIG. 6. Measured and calculated values for (a) ΔN , (b) measured and calculated CV hysteresis, (c) time evolution towards the steady state at $V = -1.2$ V, and the voltage dependence of the steady-state occupancy at (d) $T = 7$ K.

its position along the bias voltage axis. In the calculation the contributions of the individual charge states can be resolved, whereas in the measurement, such an attribution is not possible. The assignment of the three features in the calculation to the individual charge states is obtained by setting the respective contribution of one state to zero and checking which feature vanishes. It is obvious that the s states form the largest contribution to the hysteresis, which seems plausible since their electron transfer rates are the smallest ones, they are thus affected most strongly by the varying bias voltage. For the p states, a small contribution is visible, while the participation of the d states, however, is close to be negligible since they can adapt sufficiently rapidly to the changed bias voltage.

To reproduce the CV characteristics of the down-sweep numerically, the band structure of the sample is solved in a

first step, using a one-dimensional Poisson and Schrödinger solver [49]. A doping density of $n_{D,1} = 6.02 \times 10^{21} \text{ m}^{-3}$ as obtained from a $C^{-2}(V)$ analysis of the measured down-sweep was used, and the SAQD layer was simulated by a 21-nm layer of InGaAs with a constant charge density. The result of this simulation for $T = 7$ K is shown in Fig. 6(b) (upper black trace). It can be seen that the nonhysteretic shoulder at $V \approx 0$ is reproduced simply by the different layered materials. By rearranging Eq. (11) we can obtain the capacitance of the up-sweep from the calculated down-sweep and the simulated charge difference between the sweeps. The result is shown in Fig. 6(b) (upper red curve). Good agreement with the measurement [lower traces in Fig. 6(b)] can be observed regarding the boundaries of the hysteresis on the voltage axis. Two separate peaks can be observed for the s - and p -state contributions in the simulation, which cannot be resolved in the measurement. The hysteresis due to the d states is completely invisible in the CV curve.

Thus, by the analysis presented above, the qualitative picture developed in Sec. III A can be quantified and interpreted in terms of the weight by which individual SAQD states contribute to the hysteresis via their capture and emission rates. The good agreement between the measurements and the model furthermore implies that changes of the electron transfer rates by variation of the occupation numbers of the SAQDs are of minor importance, albeit this effect may explain the remaining deviations between the model and the experiment. These effects are hard to quantify since this would require unreasonably many fit parameters in our model, or maybe even a three-dimensional treatment of the SAQD potential as a function of their occupation, which is beyond our present scope.

Under the assumption that the average charge density in the SAQD layer is small compared to the doping density, the maximum, normalized opening of the hysteresis trace can be approximated as [46] $\Delta C/C_s = N n_{QD} z_{QD} / 2 \epsilon \epsilon_0 (V_{bi} - V)$. Hence, the opening of this type of hysteresis can be maximized by increasing n_{QD} or z_{QD} to their upper limits and can be suppressed by corresponding minimizations.

As the temperature is increased, the transfer rates increase as well and the SAQDs come closer to their steady state during the time window $\Delta t = 0.85$ s at each voltage. Thus, the hysteresis decreases and vanishes for our parameters at $T \approx 60$ K, see Fig. 2(b). While for the model presented here, there is no analytical expression for the observable capacitance transient as a function of the individual rates, it is reasonable to assume that the combined rate can never be slower than any individual rate. Hence, the maximum sweep rate where no hysteresis can be observed can be estimated from our model by taking the slowest individual electron transfer rate for the s state at $V \approx -1.2$ V, i.e., $r_{\min} \approx 10^{-3} \text{ s}^{-1}$ for $T = 7$ K, as the limiting factor.

VI. CALCULATION OF THE STEADY-STATE CONFIGURATION

The experimentally determined electron transfer rates can be used as input for a continuous time [53] Markov chain [54] model, with the goal to obtain the steady-state configuration, which may be inaccessible experimentally, for example, due

to the required slow voltage sweep rates. In this picture, the states of the Markov chain correspond to the charge states ($0, s, p, d$) of the SAQDs in that particular order, and we can therefore define the corresponding transition rate matrix [53] for each bias voltage as

$$Q = \begin{pmatrix} -c_{0s} & c_{0s} & 0 & 0 \\ r_{s0} & -(r_{s0} + c_{sp}) & c_{sp} & 0 \\ 0 & r_{ps} & -(r_{ps} + c_{pd}) & c_{pd} \\ 0 & 0 & r_{dp} & -r_{dp} \end{pmatrix}, \quad (12)$$

from which the occupation numbers follow via

$$P(t) = \exp(Qt), \quad (13)$$

and thus the steady-state configuration follows according to

$$P = \lim_{t \rightarrow \infty} \exp(Qt), \quad (14)$$

which was evaluated numerically using GNU OCTAVE [55].

Figure 6(c) shows, as an example, the time evolution of the system from an initial state where all SAQD states are occupied, i.e., at $V = 0$, towards its steady-state configuration at $V = -1.2$ V where the s states have equal capture and emission rates. It can be seen that the d states have a lifetime of the order of microseconds while the s states decay on the order of seconds. In general, we observed a convergence towards the steady state after, at most, 6000 s for the voltage range studied here. Calculation examples for further scenarios are given in the Supplemental Material [56].

Thus, to measure a steady-state CV of our system at $T = 7$ K, one would have to wait at least $t = 6000$ s between each voltage step which makes such an experiment impractical. Therefore, the numerical determination of the steady-state occupation probability represents a valid alternative. Here, the voltage-dependent steady-state configuration was calculated by approximating the limit in Eq. (14) by setting $t = 10^7$ s. In the steady-state configuration the rows of P are identical and the columns correspond to the occupation probability of the corresponding SAQD state. For our system this result is shown in Fig. 6(d). It can be seen that for $V < 1.5$ V the SAQDs are empty. For $V < -0.9$ V only the s states contribute to the filling factor whereas for $V < -0.5$ V both the s and the p

states are contributing. Only for $V > -0.5$ V do the d states begin to be filled with electrons.

VII. SUMMARY AND OUTLOOK

The hysteretic capacitance-voltage characteristics of self-assembled quantum dot layers with large distances to reservoirs and in strong electric fields was measured and the charge transfer dynamics was analyzed within a rate equation model. It has emerged how the hysteresis is determined by the capture and emission rates of the SAQD states, which were obtained via lock-in-DLTS. Reasonable quantitative agreement of the experimentally observed and calculated hysteresis traces as well as of the measured and calculated electron occupation numbers is found for all temperatures. The evolution of these rates as a function of the bias voltage supports an intuitive picture for the origin of the hysteresis, namely a time-dependent change of the width of the depletion region that forms between the top gate and the back electrode. Changes of the electron transfer rates by the local potential close to the SAQDs, on the other hand, appear to be of minor relevance in our system, but may be responsible for the residual deviations of the model to the experimental data. It has also been shown how these rates can be used to model the steady-state configuration, which may be inaccessible experimentally. Furthermore, the state-resolved capture rates have been measured, revealing that lower-lying states have larger capture rates, as one might expect from energetic considerations. The developed methodology is quite universal and can be applied to a variety of related scenarios, like storage of holes in SAQDs, different material systems, or the effect of the SAQD occupation number on the conductance of a nearby electron gas, as long as the relevant transfer rates lie within the experimentally accessible rate window. Hopefully, our studies inspire future work towards a better understanding of such systems, in particular regarding the electron capture process.

ACKNOWLEDGMENTS

Computational support and infrastructure was provided by the “Centre for Information and Media Technology” (ZIM) at the University of Düsseldorf (Germany). C.R., S.E.S., A.D.W., and A.L. gratefully acknowledge support of TRR 160/2-Project B04, DFG 383065199, and the DFH/UFA CDFA-05-06.

-
- [1] D. Leonard, M. Krishnamurthy, C. M. Reeves, S. P. Denbaars, and P. M. Petroff, *Appl. Phys. Lett.* **63**, 3203 (1993).
 - [2] P. M. Petroff, A. Lorke, and A. Imamoglu, *Phys. Today* **54**, 46 (2001).
 - [3] P. Michler, A. Kiraz, C. Becher, W. V. Schoenfeld, P. M. Petroff, L. Zhang, E. Hu, and A. Imamoglu, *Science* **290**, 2282 (2000).
 - [4] M. Kroutvar, Y. Ducommun, D. Heiss, M. Bichler, D. Schuh, G. Abstreiter, and J. J. Finley, *Nature (London)* **432**, 81 (2004).
 - [5] C. L. Salter, R. M. Stevenson, I. Farrer, C. Nicoll, D. A. Ritchie, and A. J. Shields, *Nature (London)* **465**, 594 (2010).
 - [6] A. Faraon, A. Majumdar, D. Englund, E. Kim, M. Bajcsy, and J. Vuckovic, *New J. Phys.* **13**, 055025 (2011).
 - [7] D. J. Mowbray and M. S. Skolnick, *J. Phys. D: Appl. Phys.* **38**, 2059 (2005).
 - [8] V. M. Ustinov, N. A. Maleev, A. E. Zhukov, A. R. Kovsh, A. Y. Egorov, A. V. Lunev, B. V. Volovik, I. L. Krestnikov, Y. G. Musikhin, N. A. Bert, P. S. Kopev, and Z. I. Alferov, *Appl. Phys. Lett.* **74**, 2815 (1999).
 - [9] E. U. Rafailov, M. A. Cataluna, and W. Sibbett, *Nat. Photon.* **1**, 395 (2007).
 - [10] S. Buckley, K. Rivoire, and J. Vučković, *Rep. Prog. Phys.* **75**, 126503 (2012).

- [11] I. L. Krestnikov, N. A. Maleev, A. V. Sakharov, A. R. Kovsh, A. E. Zhukov, A. F. Tsatsulnikov, V. M. Ustinov, Z. I. Alferov, N. N. Ledentsov, D. Bimberg, and J. A. Lott, *Semicond. Sci. Technol.* **16**, 844 (2001).
- [12] M. Geller, A. Marent, T. Nowozin, and D. Bimberg, *J. Phys. Cond. Mat.* **20**, 454202 (2008).
- [13] T. Nowozin, A. Marent, M. Geller, D. Bimberg, N. Akçay, and N. Öncan, *Appl. Phys. Lett.* **94**, 042108 (2009).
- [14] A. Marent, T. Nowozin, M. Geller, and D. Bimberg, *Semicond. Sci. Technol.* **26**, 014026 (2011).
- [15] P. Maier, F. Hartmann, M. Emmerling, C. Schneider, M. Kamp, S. Hofling, and L. Worschech, *Phys. Rev. Appl.* **5**, 054011 (2016).
- [16] K. Koike, K. Saitoh, S. Li, S. Sasa, M. Inoue, and M. Yanoa, *Appl. Phys. Lett.* **76**, 1464 (2000).
- [17] N. Ooike, J. Motohisa, and T. Fukui, *Jpn. J. Appl. Phys.* **46**, 4344 (2007).
- [18] C. R. Muller, L. Worschech, J. Heinrich, S. Höfling, and A. Forchel, *Appl. Phys. Lett.* **93**, 063502 (2008).
- [19] A. Marent, T. Nowozin, J. Gelze, F. Luckert, and D. Bimberg, *Appl. Phys. Lett.* **95**, 242114 (2009).
- [20] P. Maier, F. Hartmann, M. Emmerling, C. Schneider, S. Höfling, M. Kamp, and L. Worschech, *Appl. Phys. Lett.* **105**, 053502 (2014).
- [21] D. Nataraj, N. Ooike, J. Motohisa, and T. Fukui, *Appl. Phys. Lett.* **87**, 193103 (2005).
- [22] E. S. Kannan, G.-H. Kim, and D. A. Ritchie, *Appl. Phys. Lett.* **95**, 143506 (2009).
- [23] M. Geller, A. Marent, T. Nowozin, D. Bimberg, N. Akçay, and N. Öncan, *Appl. Phys. Lett.* **92**, 092108 (2008).
- [24] A. Gubanov, A. Schramm, V. Polojärvi, and M. Guina, *J. Phys. D: Appl. Phys.* **46**, 325102 (2013).
- [25] C. Balocco, A. M. Song, and M. Missous, *Appl. Phys. Lett.* **85**, 5911 (2004).
- [26] B. Marquardt, M. Geller, A. Lorke, D. Reuter, and A. D. Wieck, *Appl. Phys. Lett.* **95**, 022113 (2009).
- [27] M. Geller, B. Marquardt, A. Lorke, D. Reuter, and A. D. Wieck, *Nanoscale Res. Lett.* **5**, 829 (2010).
- [28] Y.-A. Liao, Y.-K. Chao, S.-W. Chang, W.-H. Chang, J.-I. Chyi, and S.-Y. Lin, *Appl. Phys. Lett.* **103**, 143502 (2013).
- [29] T. Nowozin, A. Beckel, D. Bimberg, A. A. Lorke, and M. Geller, *Appl. Phys. Lett.* **104**, 053111 (2014).
- [30] J. Nannen, W. Quitsch, S. Eliasson, T. Kummell, and G. Bacher, *Phys. Rev. B* **85**, 035325 (2012).
- [31] H. Lu, F. Guo, B. Zhang, and W. Ning, *Micro & Nano Lett.* **11**, 623 (2016).
- [32] C. R. Muller, L. Worschech, and A. Forchel, *Phys. Rev. B* **79**, 205307 (2009).
- [33] J. Nannen, T. Kummell, M. Bartsch, K. Brunner, and G. Bacher, *Appl. Phys. Lett.* **97**, 173108 (2010).
- [34] D. V. Lang, *J. Appl. Phys.* **45**, 3023 (1974).
- [35] S. Anand, N. Carlsson, M.-E. Pistol, L. Samuelson, and W. Seiffert, *Appl. Phys. Lett.* **67**, 3016 (1995).
- [36] C. M. A. Kapteyn, F. Heinrichsdorff, O. Stier, R. Heitz, M. Grundmann, N. D. Zakharov, D. Bimberg, and P. Werner, *Phys. Rev. B* **60**, 14265 (1999).
- [37] S. W. Lin, C. Balocco, M. Missous, A. R. Peaker, and A. M. Song, *Phys. Rev. B* **72**, 165302 (2005).
- [38] S. Schulz, A. Schramm, C. Heyn, and W. Hansen, *Phys. Rev. B* **74**, 033311 (2006).
- [39] M. Geller, E. Stock, C. Kapteyn, R. L. Sellin, and D. Bimberg, *Phys. Rev. B* **73**, 205331 (2006).
- [40] O. Engström, M. Kaniewska, M. Kaczmarczyk, and W. Jung, *Appl. Phys. Lett.* **91**, 133117 (2007).
- [41] A. Schramm, S. Schulz, T. Zander, C. Heyn, and W. Hansen, *Phys. Rev. B* **80**, 155316 (2009).
- [42] T. Nowozin, L. Bonato, A. Högner, A. Wiengarten, D. Bimberg, W.-H. Lin, S.-Y. Lin, C. J. Reyner, B. L. Liang, and D. L. Huffaker, *Appl. Phys. Lett.* **102**, 052115 (2013).
- [43] L. Schnorr, T. Heinzl, S. Scholz, A. Ludwig, and A. D. Wieck, *J. Appl. Phys.* **124**, 104301 (2018).
- [44] L. Schnorr, J. Labes, L. Kurten, T. Heinzl, C. Rothfuchs-Engels, S. Scholz, A. Ludwig, and A. D. Wieck, *Phys. Rev. B* **104**, 035303 (2021).
- [45] D. S. Day, M. Y. Tsai, B. G. Streetman, and D. V. Lang, *J. Appl. Phys.* **50**, 5093 (1979).
- [46] S. Schulz, Ph.D. Thesis, Hamburg University (2005).
- [47] V. Korobov and V. Ochkov, *Chemical Kinetics with Mathcad and Maple* (Springer, Vienna, 2011).
- [48] E. N. Korol, *Ukr. Phys. J.* **18**, 1890 (1973).
- [49] G. Snider, 1D Poisson-Schrodinger solver (2017), <https://www3.nd.edu/~gsnider/>, Accessed on Sep. 15th, 2017.
- [50] P. Virtanen, R. Gommers, T. E. Oliphant, M. Haberland, T. Reddy, D. Cournapeau, E. Burovski, P. Peterson, W. Weckesser, J. Bright, S. J. van der Walt, M. Brett, J. Wilson, K. J. Millman, N. Mayorov, A. R. J. Nelson, E. Jones, R. Kern, E. Larson, C. J. Carey, Í. Polat, Y. Feng, E. W. Moore, J. VanderPlas, D. Laxalde, J. Perktold, R. Cimrman, I. Henriksen, E. A. Quintero, C. R. Harris, A. M. Archibald, A. H. Ribeiro, F. Pedregosa, P. van Mulbregt, and SciPy 1.0 Contributors, *Nature Methods* **17**, 261 (2020).
- [51] E. Hairer and G. Wanner, *Solving Ordinary Differential Equations II. Stiff and Differential-Algebraic Problems*, Vol. 14 (Springer, New York, 1996).
- [52] R. J. Luyken, A. Lorke, A. O. Govorov, J. P. Kotthaus, G. Medeiros-Ribeiro, and P. Petroff, *Appl. Phys. Lett.* **74**, 2486 (1999).
- [53] J. R. Norris, in *Markov Chains*, Cambridge Series in Statistical and Probabilistic Mathematics (Cambridge University Press, Cambridge, 1997), pp. 60–107.
- [54] A. A. Markov, *Sci. Context* **19**, 591 (2006).
- [55] J. W. Eaton, D. Bateman, S. Hauberg, and R. Wehbring, GNU Octave version 5.2.0 manual: A high-level interactive language for numerical computations (2020).
- [56] See Supplemental Material at <http://link.aps.org/supplemental/10.1103/PhysRevB.104.205310> for simulations under additional initial conditions.

Hysteretic capacitance-voltage characteristics of self-assembled quantum dots far from equilibrium with their environment

L. Schnorr, O. Khoukhi, L. Berg, and T. Heinzel*

Solid State Physics Laboratory, Heinrich-Heine-Universität Düsseldorf, 40204 Düsseldorf, Germany

C. Rothfuchs-Engels, S. Scholz, A. Ludwig, and A. D. Wieck

Lehrstuhl für Angewandte Festkörperphysik, Ruhr-Universität Bochum, 44780 Bochum, Germany

This supplement gives further information on the time dependent occupation probability of the SAQD ensembles at selected bias voltages as well as the voltage dependent time required to reach a steady state.

I. TIME EVOLUTION

Figure 1 shows the calculated, time dependent occupation probability of the SAQD layer for various bias voltages after preparation in the initial state with all three SAQD levels fully occupied. As discussed in the main text, the time needed to reach a steady state configuration shows a maximum for $V = -1.2$ V.

II. SETTLING TIME

Figure 2 shows the time needed to reach the steady state as a function of the bias voltage. Three peaks can be observed at $V = -1.2$ V, $V = -0.62$ V and $V = -0.29$ V which coincide with the crossings of the capture and emission rates for the s-, p- and d-states, respectively, in Fig. 5(c) of the main text, as well as with the maxima of the calculated hysteretic charge difference in Fig. 6(a) . The global maximum of the time needed to reach a steady state is located at $V = -1.2$ V where it amounts to 5200 s.

* thomas.heinzel@hhu.de

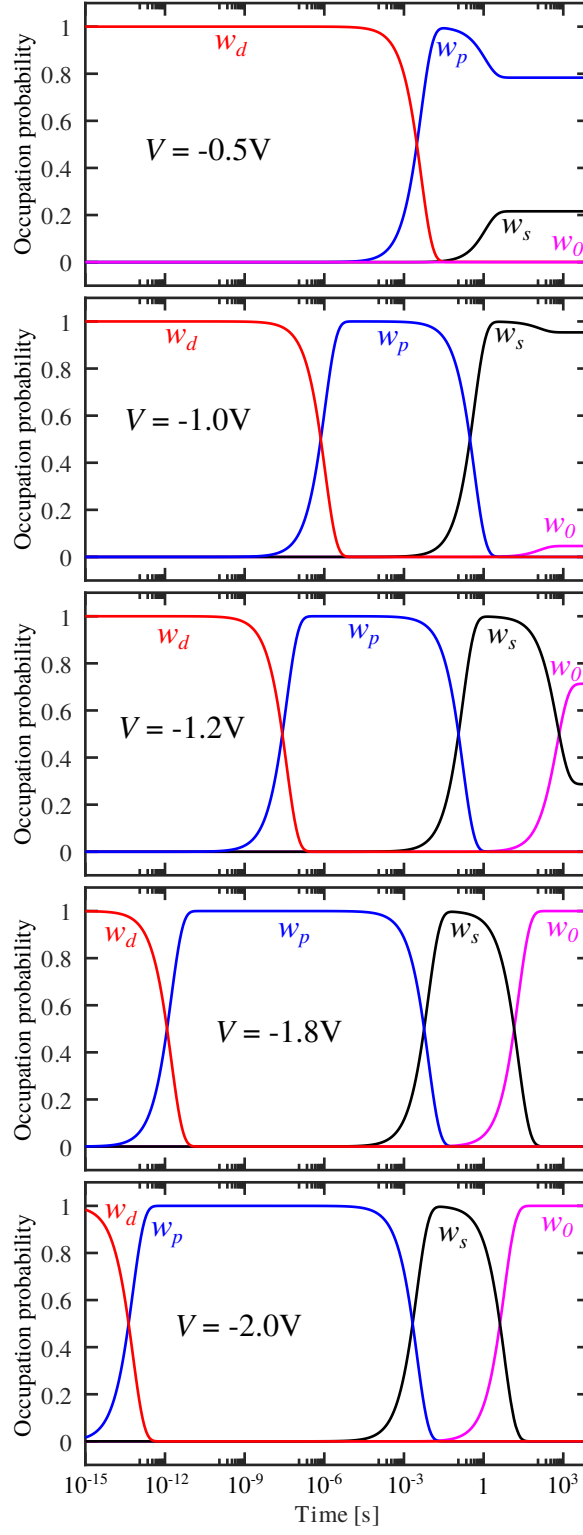


FIG. 1. Time evolution towards the steady state from completely filled SAQDs at various bias voltages.

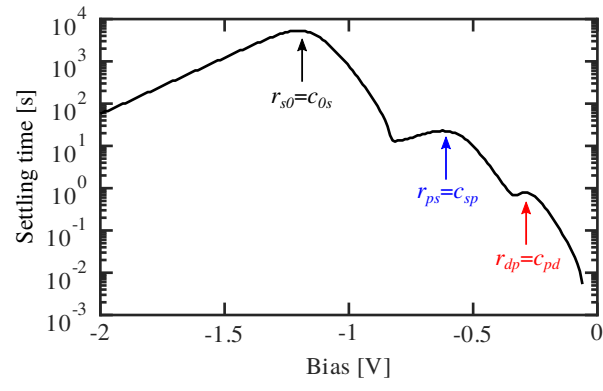


FIG. 2. Time needed to reach a steady state as a function of the bias voltage.

Chapter 7

Conclusion and outlook

Within this thesis it was demonstrated that Laplace DLTS is a valuable tool in the study of the charge transfer dynamics of SAQDs. The temperature and voltage dependence of the emission rates could be measured with a high enough resolution to resolve individual charge states. To do so, a regularized Laplace inversion algorithm was implemented that could deal both with the experimental realities of capacitance transient data and the large data sets that need to be transformed in parallel when parameter sweeps are studied.

Both conventional and Laplace DLTS have been used for the first time to study the electron capture rates as a function of the applied bias voltage both at temperatures where thermal activation is expected to dominate the dynamics and in the tunneling regime. The voltage range of these experiments also covered the transition regime where the dynamics of the system are governed by both the capture and emission processes and consequently neither could be neglected in the analysis. To describe the dynamics over the entire parameter space multi-step charging models were used which could model the measurements quantitatively over the entire parameter space. A representation of these models as continuous time Markov chains allowed for the prediction of the time dependence of the system at experimentally inaccessible time scales.

The capture rates measured in this thesis show that in the temperature range under study the capture rates decrease with decreasing temperature and increase with increasing bias voltage. The latter observation stands in contrast to behavior of the emission dynamics which increase with decreasing bias voltage due to the modification of the confinement potential caused by the band bending of the Schottky structure. This implies that the shape of the confinement potential is of negligible influence for the capture dynamics which are instead dominated by the voltage dependent energetic alignment of the SAQD states within the energy band structure. At low temperatures, where charge state dependent capture rates could be resolved, it was furthermore found that the capture rate decreases with an increasing amount of charge already present in the SAQDs, an effect that is in agreement with the well established Coulomb blockade.

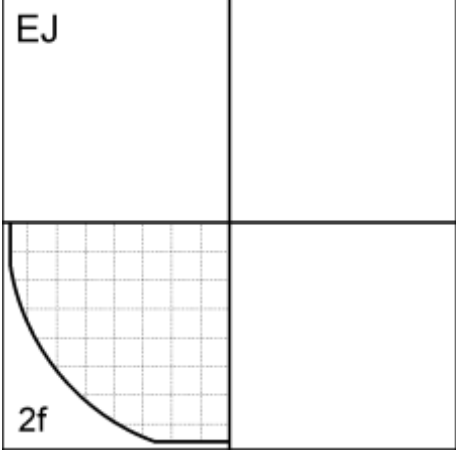
The knowledge obtained from the analysis of the charge transfer transients using the models described in this thesis could be used at low temperatures without modification

to quantitatively model the hysteretic capacitance-voltage traces measured at larger time scales. The features of the hysteretic CV traces could be unambiguously matched to the properties of the SAQDs and the sample structure. This makes such a modeling approach a valuable tool for the study of dynamics under conditions that are difficult or impossible to access in experiments.

The voltage dependent steady state configuration of the SAQD charge states could be extrapolated from the measured data showing that the occupancy of the dots is orders of magnitudes larger than expected when assuming a thermal equilibrium between the dots and the bulk material. Hence, the electron reservoir in the back contact of the Schottky structure cannot be the dominant source of electrons that get captured into the dots. A possible additional source could be leakage currents which are known to increase the electron capture rate [110]. To investigate this, detailed measurements of the leakage current as a function of bias voltage and temperature could be carried out and analyzed accordingly. Another approach could be to grow a sample structure that has additional barriers made of AlAs on the metal-facing and/or on the back contact-facing side of the SAQD layer. Such barriers would block off leakage currents and measurements of the capture rates as presented in this thesis could be used to observe the influence of each barrier configuration on the capture dynamics and the resulting steady state configurations.

A promising outlook for future measurements could also be a detailed study of the temperature dependence of the capture rates that has in this thesis only been conducted at two temperatures. Such an investigation might shed more light on the physical origin of the electrons that get captured into the SAQDs without the need to grow more sample structures.

So far only Schottky structures with one embedded layer of SAQDs have been studied using the methods presented in this thesis. All procedures described in this work are however expandable to multiple layers that could be positioned at almost arbitrary positions throughout the sample. A study of closely grown SAQD layers where the individual dots can quantum-mechanically couple to each other might offer additional insight into the field of quantum dot molecules [148]. More distantly grown SAQD layers could be used to study the longer range electrostatic influences of their respective electron occupancies on each others charge transfer dynamics.



Sample:	14691
Material:	GaAs
Orientation:	(100)
Wafer:	WV/23678/Un61
Rotation:	4
Pressure (Torr):	4.2×10^{-8}
Date:	27.08.2015
File:	14691.csv

[illegible]

Bibliography

- [1] D. Leonard, M. Krishnamurthy, C. M. Reaves, S. P. Denbaars, and P. M. Petroff, *Appl. Phys. Lett.* **63**, 3203 (1993).
 - [2] P. M. Petroff, A. Lorke, and A. Imamoglu, *Phys. Today* **54**, 46 (2001).
 - [3] A. Kurzmann, B. Merkel, B. Marquardt, A. Beckel, A. Ludwig, A. D. Wieck, A. Lorke, and M. Geller, *physica status solidi (b)* **254**, 1600625 (2017).
 - [4] R. J. Luyken, A. Lorke, A. O. Govorov, J. P. Kotthaus, G. Medeiros-Ribeiro, and P. Petroff, *Appl. Phys. Lett.* **74**, 1999 (2486).
 - [5] S. R. Valentin, J. Schwinger, P. Eickelmann, P. A. Labud, A. D. Wieck, B. Sothmann, and A. Ludwig, *Phys. Rev. B* **97**, 045416 (2018).
 - [6] P. Michler, A. Kiraz, C. Becher, W. V. Schoenfeld, P. M. Petroff, L. Zhang, E. Hu, and A. Imamoglu, *Science* **290**, 2282 (2000).
 - [7] M. Kroutvar, Y. Ducommun, D. Heiss, M. Bichler, D. Schuh, G. Abstreiter, and J. J. Finley, *Nature* **432**, 81 (2004).
 - [8] C. L. Salter, R. M. Stevenson, I. Farrer, C. Nicoll, D. A. Ritchie, and A. J. Shields, *Nature* **465**, 594 (2010).
 - [9] A. Faraon, A. Majumdar, D. Englund, E. Kim, M. Bajcsy, and J. Vuckovic, *New J. Phys.* **13**, 055025 (2011).
 - [10] A. Beckel, A. Ludwig, A. D. Wieck, A. Lorke, and M. Geller, *Phys. Rev. B* **89**, 155430 (2014).
 - [11] I. L. Krestnikov, N. A. Maleev, A. V. Sakharov, A. R. Kovsh, A. E. Zhukov, A. F. Tsatsulnikov, V. M. Ustinov, Z. I. Alferov, N. N. Ledentsov, D. Bimberg, and J. A. Lott, *Semicond. Sci. Technol.* **16**, 8844 (2001).
 - [12] V. M. Ustinov, N. A. Maleev, A. E. Zhukov, A. R. Kovsh, A. Y. Egorov, A. V. Lunev, B. V. Volovik, I. L. Krestnikov, Y. G. Musikhin, N. A. Bert, P. S. Kopev, and Z. I. Alferov, *Appl. Phys. Lett.* **74**, 2815 (1999).
 - [13] E. U. Rafailov, M. A. Cataluna, and W. Sibbett, *Nature Photonics* **1**, 395 (2007).
 - [14] A. Luque, A. Marti, and C. Stanley, *Nature Photonics* **6**, 146 (2012).
 - [15] T. Li, H. Lu, L. Fu, H. H. Tan, C. Jagadish, and M. Deganaï, *Appl. Phys. Lett.* **106**, 053902 (2015).
 - [16] S. Buckley, K. Rivoire, and J. Vučković, *Rep. Prog. Phys.* **347**, 539 (1990).
-

-
- [17] P. Maier, F. Hartmann, M. Emmerling, C. Schneider, S. Höfling, and L. Worschech, *Phys. Rev. Appl.* **5**, 0540112 (2016).
 - [18] M. Geller, A. Marent, T. Nowozin, and D. Bimberg, *J. Phys. Cond. Mat.* **20**, 454202 (2008).
 - [19] T. Nowozin, A. Marent, M. Geller, D. Bimberg, N. Akcay, and N. Öncan, *Appl. Phys. Lett.* **94**, 042108 (2009).
 - [20] A. Marent, T. Nowozin, M. Geller, and D. Bimberg, *Semicond. Sci. Technol.* **26**, 014026 (2011).
 - [21] Y.-A. Liao, Y.-. Chao, S.-W. Chang, W.-H. Chang, J.-I. Chyi, and S.-Y. Lin, *Appl. Phys. Lett.* **103**, 143502 (2013).
 - [22] H. Lu, F. Guo, B. Zhang, and W. Ning, *Micro & Nano Lett.* **11**, 623 (2016).
 - [23] J. Nannen, W. Quitsch, S. Eliasson, T. KÜmmell, and G. Bacher, *Phys. Rev. B* **85**, 035325 (2012).
 - [24] D. Zhou, A. Beckel, A. Ludwig, A. D. Wieck, A. Lorke, and M. Geller, *Appl. Phys. Lett.* **106**, 243105 (2015).
 - [25] H. Drexler, D. Leonard, W. Hansen, J. P. Kotthaus, and P. M. Petroff, *Phys. Rev. Lett.* **73**, 2252 (1994).
 - [26] O. Wibbelhoff, A. Lorke, D. Reuter, and A. W. Wieck, *Appl. Phys. Lett.* **86**, 092104 (2005).
 - [27] P. N. Brounkov, A. Polimeni, S. T. Stoddart, M. Henini, L. Eaves, P. C. Main, A. R. Kovsh, Y. G. Musikhin, and S. G. Konnikov, *Appl. Phys. Lett.* **73**, 1092 (1998).
 - [28] P. Kailuweit, D. Reuter, A. Wieck, O. Wibbelhoff, A. Lorke, U. Zeitler, and J. Maan, *Physica E: Low-dimensional Systems and Nanostructures* **32**, 159 (2006).
 - [29] D. V. Lang, *J. Appl. Phys.* **45**, 3023 (1974).
 - [30] S. Anand, N. Carlsson, M.-E. Pistol, L. Samuelson, and W. Seiffert, *Appl. Phys. Lett.* **67**, 3016 (1995).
 - [31] C. M. A. Kapteyn, F. Heinrichsdorff, O. Stier, R. Heitz, M. Grundmann, N. D. Zakharov, D. Bimberg, and P. Werner, *Phys. Rev. B* **60**, 14265 (1999).
 - [32] C. M. A. Kapteyn, M. Lion, R. Heitz, D. Bimberg, P. M. Brunkov, B. V. Volovik, S. G. Konnikov, A. R. Kovsh, and V. M. Ustinov, *Appl. Phys. Lett.* **76**, 1573 (2000).
 - [33] C. M. A. Kapteyn, M. Lion, R. Heitz, D. Bimberg, C. Miesner, T. Asperger, and G. Abstreiter, *Appl. Phys. Lett.* **77**, 4169 (2000).
 - [34] M. Geller, C. Kapteyn, L. Müller-Kirsch, R. Heitz, and D. Bimberg, *Appl. Phys. Lett.* **82**, 2706 (2003).
 - [35] O. Engström, M. Malmkvist, Y. Fu, H. O. Olafsson, and E. O. Sveinbjörnsson, *Appl. Phys. Lett.* **83**, 3578 (2003).
-

-
- [36] S. Schulz, S. Schnüll, C. Heyn, and W. Hansen, *Phys. Rev. B* **69**, 195317 (2004).
 - [37] A. Schramm, S. Schulz, J. Schaefer, T. Zander, C. Heyn, and W. Hansen, *Appl. Phys. Lett.* **88**, 213107 (2006).
 - [38] A. Schramm, S. Schulz, C. Heyn, and W. Hansen, *Phys. Rev. B* **77**, 153308 (2008).
 - [39] A. Schramm, S. Schulz, T. Zander, C. Heyn, and W. Hansen, *Phys. Rev. B* **80**, 155316 (2009).
 - [40] L. Dobaczewski, P. Kaczor, I. D. Hawkins, and A. R. Peaker, *J. Appl. Phys.* **76**, 194 (1994).
 - [41] S. W. Lin, A. M. Song, M. Missous, I. D. Hawkins, B. Hamilton, O. Engström, and A. R. Peaker, *Mat. Sci. Engin. C* **26**, 760 (2006).
 - [42] P. Kruszewski, L. Dobaczewski, V. P. Markevich, C. Mitchell, M. Missous, and A. R. Peaker, *Physica B - Cond. Mat.* **580**, 401 (2007).
 - [43] S. Schulz, A. Schramm, C. Heyn, and W. Hansen, *Phys. Rev. B* **74**, 033311 (2006).
 - [44] O. Engström and M. Kaniewska, *Nanoscale research letters* **3**, 179 (2008).
 - [45] R. Nagarajan, D. Tauber, and J. E. Bowers, *International Journal of High Speed Electronics and Systems* **05**, 1–44 (1994).
 - [46] J. Wang, M. Haldar, L. Li, and F. Mendis, *IEEE Photonics Technology Letters* **8**, 34 (1996).
 - [47] L. Schnorr, T. Heinzl, S. Scholz, A. Ludwig, and A. D. Wieck, *J. Appl. Phys.* **124**, 104301 (2018).
 - [48] S. Raymond, S. Fafard, P. J. Poole, A. Wojs, P. Hawrylak, S. Charbonneau, D. Leonard, R. Leon, P. M. Petroff, and J. L. Merz, *Phys. Rev. B* **54**, 11548 (1996).
 - [49] P. Miska, J. Even, O. Dehaese, and X. Marie, *Appl. Phys. Lett.* **92**, 191103 (2008).
 - [50] Y. I. Mazur, V. G. Dorogan, E. Marega, Z. Y. Zhuchenko, M. E. Ware, M. Benamara, G. G. Tarasov, P. Vasa, C. Lienau, and G. J. Salamo, *J. Appl. Phys.* **108**, 074316 (2010).
 - [51] C. Walther, J. Bollmann, H. Kissel, H. Kirmse, W. Neumann, and W. Masselink, *Physica B: Condensed Matter* **273–274**, 971 (1999).
 - [52] L. Schnorr, J. Labes, L. Kürten, T. Heinzl, C. Rothfuchs-Engels, S. Scholz, A. Ludwig, and A. D. Wieck, *Phys. Rev. B* **104**, 035303 (2021).
 - [53] L. Schnorr, O. Khoukhi, L. Berg, T. Heinzl, C. Rothfuchs-Engels, S. Scholz, A. Ludwig, and A. D. Wieck, *Phys. Rev. B* **104**, 205310 (2021).
 - [54] D. V. Averin and K. K. Likharev, *Journal of low temperature physics* **62**, 345 (1986).
 - [55] D. Nataraj, N. Ooike, J. Motohisa, and T. Fukui, *Appl. Phys. Lett.* **87**, 193103
-

- (2005).
- [56] E. S. Kannan, G.-H. Kim, and D. A. Ritchie, Appl. Phys. Lett. **95**, 143506 (2009).
 - [57] M. Geller, A. Marent, T. Nowozin, D. Bimberg, N. Akçay, and N. Öncan, Appl. Phys. Lett. **92**, 092108 (2008).
 - [58] A. Gubanov, A. Schramm, V. Polojärvi, and M. Guina, J. Phys. D: Appl. Phys. **46**, 325102 (2013).
 - [59] C. Balocco, A. M. Song, and M. Missous, Appl. Phys. Lett. **85**, 5911 (2004).
 - [60] C. R. Müller, L. Worschech, J. Heinrich, S. Höfling, and A. Forchel, Appl. Phys. Lett. **93**, 063502 (2008).
 - [61] B. Marquardt, M. Geller, A. Lorke, D. Reuter, and A. D. Wieck, Appl. Phys. Lett. **95**, 022113 (2009).
 - [62] A. Marent, T. Nowozin, J. Gelze, F. Luckert, and D. Bimberg, Appl. Phys. Lett. **95**, 242112 (2009).
 - [63] M. Geller, B. Marquardt, A. Lorke, D. Reuter, and A. D. Wieck, Nanoscale Res. Lett. **5**, 829 (2010).
 - [64] T. Nowozin, A. Beckel, D. Bimberg, A. A. Lorke, and M. Geller, Appl. Phys. Lett. **104**, 053111 (2014).
 - [65] P. Maier, F. Hartmann, M. Emmerling, C. Schneider, S. Höfling, M. Kamp, and L. Worschech, Appl. Phys. Lett. **105**, 053502 (2014).
 - [66] L. De Broglie, Ann. Phys. **10**, 22 (1925).
 - [67] T. Fließbach, *Quantenmechanik: Lehrbuch zur Theoretischen Physik III*, Springer Berlin Heidelberg, 2018.
 - [68] D. F. Underwood, T. Kippeny, and S. J. Rosenthal, The Journal of Physical Chemistry B **105**, 436 (2001).
 - [69] B. Dubertret, P. Skourides, D. J. Norris, V. Noireaux, A. H. Brivanlou, and A. Libchaber, Science **298**, 1759 (2002).
 - [70] K. Horibe, T. Kodera, and S. Oda, Appl. Phys. Lett. **106**, 083111 (2015).
 - [71] M. Ciorga, A. S. Sachrajda, P. Hawrylak, C. Gould, P. Zawadzki, S. Jullian, Y. Feng, and Z. Wasilewski, Phys. Rev. B **61**, R16315 (2000).
 - [72] V. B. Verma, U. Reddy, N. L. Dias, K. P. Bassett, X. Li, and J. J. Coleman, IEEE Journal of Quantum Electronics **46**, 1827 (2010).
 - [73] A. Cho and J. Arthur, Progress in Solid State Chemistry **10**, 157 (1975).
 - [74] K. L. Wang, D. Cha, J. Liu, and C. Chen, Proceedings of the IEEE **95**, 1866 (2007).
 - [75] C. Rothfuchs, F. Semond, M. Portail, O. Tottereau, A. Courville, A. D. Wieck, and A. Ludwig, Nuclear Instruments and Methods in Physics Research Section B: Beam Interactions with Materials and Atoms **409**, 107 (2017), Proceedings of the 20th International Conference on Ion Beam Modification of Materials (IBMM
-

- 2016).
- [76] M. Volmer and A. Weber, *Z. Phys. Chem.* **119**, 277 (1926).
 - [77] F. C. Frank and J. H. van der Merve, *Proc. R. Soc. London A* **198**, 205 (1949).
 - [78] I. N. Stranski and L. Krastanow, *Monatshefte für Chemie und verwandte Teile anderer Wissenschaften* **71**, 351 (1937).
 - [79] T. Heinzel, *Mesoscopic Electronics in Solid State Nanostructures*, Wiley-VCH, 2007.
 - [80] W. Ostwald, *Zeitschrift für Physikalische Chemie* **22**, 289 (1897).
 - [81] B. D. Min, Y. Kim, E. K. Kim, S.-K. Min, and M. J. Park, *Phys. Rev. B* **57**, 11879 (1998).
 - [82] A. Raab and G. Springholz, *Appl. Phys. Lett.* **77**, 2991–2993 (2000).
 - [83] V. Fock, *Z. Phys.* **47**, 446 (1928).
 - [84] C. G. Darwin, *Proc. Cambr. Philos. Soc.* **27**, 86 (1931).
 - [85] L. P. Kouwenhoven, D. G. Austing, and S. Tarucha, *Reports on Progress in Physics* **64**, 701 (2001).
 - [86] S. Schulz, *Kapazitäts- und Kapazitätstransientenspektroskopie an selbstorganisiert gewachsenen InAs-Quantenpunkten*, PhD thesis, Universität Hamburg, 2005.
 - [87] R. J. Warburton, B. T. Miller, C. S. Dürr, C. Bödefeld, K. Karrai, J. P. Kotthaus, G. Medeiros-Ribeiro, P. M. Petroff, and S. Huant, *Phys. Rev. B* **58**, 16221 (1998).
 - [88] W. Schottky, *Zeitschrift für Physik* **118**, 539 (1942).
 - [89] F. Thuselt, *Physik der Halbleiterbauelemente*, Springer Berlin Heidelberg, 2011.
 - [90] G. Myburg, F. Aurret, W. Meyer, C. Louw, and M. Van Staden, *Thin solid films* **325**, 181 (1998).
 - [91] J. Bardeen, *Phys. Rev.* **71**, 717 (1947).
 - [92] G. Margaritondo, *Reports on Progress in Physics* **62**, 765 (1999).
 - [93] G. Snider, 1D Poisson-Schrödinger solver, <https://www3.nd.edu/~gsnider/>, Accessed on Sep 15th, 2017.
 - [94] H. Card and E. Rhoderick, *Journal of Physics D: Applied Physics* **4**, 1589 (1971).
 - [95] E. H. Rhoderick, *IEEE Proceedings I-Solid-State and Electron Devices* **129**, 1 (1982).
 - [96] M. Cerchez, H. Langer, M. E. Achhab, T. Heinzel, H. Lüder, and D. Ostermann, *Appl. Phys. Lett.* **103**, 033522 (2013).
 - [97] J. Werner, *Appl. Phys. A* **47**, 291 (1988).
 - [98] J. L. Benton, *Journal of Crystal Growth* **106**, 116 (1990).
 - [99] L. Schnorr, M. Cerchez, D. Ostermann, and T. Heinzel, *Phys. Status Solidi B* **253**, 690 (2016).
-

-
- [100] W. Shockley and W. T. Read, *Phys. Rev.* **87**, 835 (1952).
 - [101] G. L. Miller, D. V. Lang, and L. C. Kimerling, *Annual Review of Materials Science* **7**, 377 (1977).
 - [102] K. J. Laidler, *Journal of Chemical Education* **61**, 494 (1984).
 - [103] G. Vincent, *Étude des niveaux profonds dans GaAs par analyse des transitoires d'admittance*, PhD thesis, Université de Claude Bernard Lyon, Institut National des Sciences appliquées, 1978.
 - [104] G. Vincent, A. Chantre, and D. Bois, *J. Appl. Phys.* **50**, 5484 (1979).
 - [105] G. Frenkel, *Phys. Rev.* **4**, 647 (1938).
 - [106] J. G. Simmons, *Phys. Rev.* **155**, 657 (1967).
 - [107] K. D. Sattler, *Handbook of nanophysics: Nanoelectronics and Nanophotonics*, chapter 2, CRC press, 2010.
 - [108] J. Hartke, *J. Appl. Phys.* **39**, 4871 (1968).
 - [109] P. A. Martin, B. Streetman, and K. Hess, *J. Appl. Phys.* **52**, 7409 (1981).
 - [110] M. C. Chen, D. V. Lang, W. C. Dautremont-Smith, A. M. Sergent, and J. P. Harbison, *Appl. Phys. Lett.* **44**, 790 (1984).
 - [111] E. K. Kim, H. Y. Cho, S. Min, S. H. Choh, and S. Namba, *J. Appl. Phys.* **67**, 1380 (1990).
 - [112] K. Dmowski, B. Lepley, E. Losson, and M. E. Bouabdellati, *Journal of Applied Physics* **74**, 3936 (1993).
 - [113] V. Korobov and V. Ochkov, *Chemical Kinetics with Mathcad and Maple*, Springer, Vienna, 2011.
 - [114] R. Williams, *J. Appl. Phys.* **37**, 3411 (1966).
 - [115] H. London, G. R. Clarke, and E. Mendoza, *Phys. Rev.* **128**, 1992 (1962).
 - [116] W. E. Gifford and R. C. Longworth, *Journal of Engineering for Industry* **86**, 264 (1964).
 - [117] Zurich Instruments, *HF2 User Manual*.
 - [118] pico Technology, *PicoScope 6 PC Oscilloscope Software User's Guide*.
 - [119] T. Miyagi, T. Ogawa, M. Kamei, Y. Wada, T. Mitsuhashi, A. Yamazaki, E. Ohta, and T. Sato, *Jpn. J. Appl. Phys.* **40**, L404 (2001).
 - [120] D. S. Day, M. Y. Tsai, B. G. Streetman, and D. V. Lang, *J. Appl. Phys.* **50**, 5093 (1979).
 - [121] A. A. Istratov and O. F. Vyvenko, *Review of Scientific Instruments* **70**, 1233 (1999).
 - [122] Y.-K. Kwok and D. Barthez, *Inverse Problems* **5**, 1089 (1989).
 - [123] H. Hassanzadeh and M. Pooladi-Darvish, *Applied Mathematics and Computation* **189**, 1966 (2007).
 - [124] K. S. Crump, *J. ACM* **23**, 89 (1976).
-

-
- [125] D. P. Gaver, *Operations Research* **14**, 444 (1966).
- [126] P. Hansen, *Discrete Inverse Problems*, Society for Industrial and Applied Mathematics, 2010.
- [127] C. Lanczos, *Applied Analysis*, p. 272 ff., Prentice-Hall, Inc., 1956.
- [128] D. G. Gardner, *Annals of the New York Academy of Sciences* **108**, 195 (1963).
- [129] A. N. Tikhonov, *Soviet Math. Dokl.* **4**, 1035 (1963).
- [130] C. L. Lawson and R. J. Hanson, *Solving least squares problems*, chapter 26, SIAM, 1995.
- [131] V. A. Morozov, *USSR Computational Mathematics and Mathematical Physics* **8**, 63 (1968).
- [132] C. L. Lawson, R. J. Hanson, D. R. Kincaid, and F. T. Krogh, *ACM Trans. Math. Softw.* **5**, 308–323 (1979).
- [133] Q. Wang, X. Zhang, Y. Zhang, and Q. Yi, AUGEM: automatically generate high performance dense linear algebra kernels on x86 CPUs, in *Proceedings of the International Conference on High Performance Computing, Networking, Storage and Analysis*, SC '13, New York, NY, USA, 2013, Association for Computing Machinery.
- [134] X. Zhang, Q. Wang, and Y. Zhang, Model-Driven Level 3 BLAS Performance Optimization on Loongson 3A Processor, ICPADS '12, p. 684–691, USA, 2012, IEEE Computer Society.
- [135] Intel, www.intel.com/content/www/us/en/developer/tools/oneapi/onemkl.html, 2021, [Accessed on Dec 13th, 2021].
- [136] E. H. Moore, *Bulletin of the American Mathematical Society* **26**, 394–395 (1920).
- [137] R. Penrose, *Mathematical Proceedings of the Cambridge Philosophical Society* **51**, 406–413 (1955).
- [138] M. Lourakis, levmar: Levenberg-marquardt nonlinear least squares algorithms in C/C++, <https://users.ics.forth.gr/~lourakis/levmar/>, Jul. 2004, [Accessed on 13 Dec. 2021.].
- [139] K. Levenberg, *Quart. Appl. Math.* **2**, 164 (1944).
- [140] D. W. Marquardt, *Journal of the Society for Industrial and Applied Mathematics* **11**, 431 (1963).
- [141] L. Dobaczewski, A. R. Peaker, and K. Bonde Nielsen, *J. Appl. Phys.* **96** (2004).
- [142] J. Coutinho, O. Andersen, L. Dobaczewski, K. Bonde Nielsen, A. R. Peaker, R. Jones, S. Öberg, and P. R. Briddon, *Phys. Rev. B* **68**, 184106 (2003).
- [143] M. Geller, *Appl. Phys. Rev.* **6**, 031306 (2019).
- [144] K. Koike, K. Saitoh, S. Li, S. Sasa, M. Inoue, and M. Yanoa, *Appl. Phys. Lett.* **76**, 1464 (2000).
- [145] N. Ooike, J. Motohisa, and T. Fukui, *Jpn. J. Appl. Phys.* **46**, 4344 (2007).
- [146] J. R. Norris, *Continuous-time Markov chains I*, p. 60–107, Cambridge Series in
-

- Statistical and Probabilistic Mathematics, Cambridge University Press, 1997.
- [147] A. A. Markov, *Science in Context* **19**, 591–600 (2006).
- [148] S. Suraprapapich, Y. Shen, V. Odnoblyudov, Y. Fainman, S. Panyakeow, and C. Tu, *Journal of Crystal Growth* **301-302**, 735 (2007), 14th International Conference on Molecular Beam Epitaxy.
-

Danksagung

An dieser Stelle möchte ich den Leuten danken die besonders zum Gelingen dieser Arbeit beigetragen haben.

Zuerst möchte ich meinem Doktorvater Prof. Dr. Thomas Heinzl dafür danken, dass ich die Möglichkeit hatte meine Doktorarbeit bei ihm in der Gruppe schreiben zu können. Vielen Dank für die jahrelange tolle Betreuung schon seit meiner Bachelorarbeit und genauso für die vielen Freiräume die Du mir gelassen hast, wenn ich mal wieder eine neue Idee hatte was man basteln und ausprobieren könnte. Außerdem bin ich sehr dankbar, dass Du mir ermöglicht hast zum TRNM-Meeting nach Levi hinter den finnischen Polarkreis zu fahren, was eine unglaublich spannende und wertvolle Erfahrung war die ich sonst sehr wahrscheinlich nie gemacht hätte.

Prof. Dr. Andreas D. Wieck und Dr. Arne Ludwig von der Ruhr-Universität Bochum möchte ich für die jahrelange tolle Kooperation und die erstklassigen Proben die Ihr für uns gewachsen habt danken ohne die diese Arbeit nicht möglich gewesen wäre. Die vielen Besuche bei Euch waren stets sehr angenehm und haben mich immer weitergebracht. Charlotte Rothfuchs-Engels danke ich für die Präparation der Probe an der ich während meiner Promotion gemessen habe, und natürlich auch für die kleineren gemeinsamen Projekte mit denen wir unsere Bachelorstudierenden versorgen konnten.

Auch danke ich Prof. Dr. Axel Görlitz für das Mentoring und Prof. Dr. Reinhold Egger für die Übernahme des Koreferats.

Bianka Lindenau danke ich dafür, dass sie stets den Überblick über alle Anträge, Formulare und Fristen hatte und ich in der Hinsicht nie mehr tun musste als hin und wieder etwas zu unterschreiben.

Den (ehemaligen) technischen Mitarbeitern am Institut Wilfried Gjungjek-Schützek und Uwe Zimmermann möchte ich für die Unterstützung über die Jahre danken wenn es darum ging einen ganz bestimmten Stecker oder eine Schraube zu finden oder mal wieder eine Wagenladung Flüssiggaskannen von A nach B zu bringen.

Ich habe mich von Anfang an am Lehrstuhl für Festkörperphysik sehr wohl gefühlt. Das lag an den hilfsbereiten und freundlichen Kolleginnen und Kollegen die ich über die Jahre kennenlernen durfte. Special thanks go out to Mihai Cerchez, you introduced me to the lab equipment when I joined the group and always had the time to help me with any questions I came up with, be it the inner workings of a cryostat or the right amount of plums to put into a pie. Thank you as well for letting me do the experiments in your electronics lecture, I had great fun doing it. Meinen (ehemaligen) MitdoktorandInnen Jakob, Svenja, Beate, Stefan, Christian und Cathrin danke ich für

die stets angenehme Zusammenarbeit und die gegenseitige Unterstützung, sei es im Leben oder in der Forschung, auch wenn unsere Themen teilweise recht verschieden waren. Meinem Bürogenossen und Nachfolger Lukas danke ich ganz besonders für die wertvollen Anregungen die ein zweiter Kopf in das SAQD-Projekt gebracht hat und dafür, dass er mir nach Jahren als einziger Doktorand auf diesem Thema einiges an Arbeit abgenommen hat. Nikolai möchte ich dafür danken, dass er als Student ohne Bezug zu meinem Projekt stets bereit war bei lästigen Aufgaben wie dem Umbauen des Kryostaten zu helfen und bereitwillig als Versuchskaninchen für mein Messprogramm hergehalten hat.

Auch die Betreuung von Bachelor- und Masterarbeiten hat mir viel Freude bereitet. Alles Gute und viel Erfolg weiterhin für Laura, Lars, Jennifer, Lukas und Ouafaa.

Meiner Mutter danke ich dafür, dass sie mich immer in meinen Interessen gefördert hat und die unzähligen Einkäufe zuerst im Lego-Katalog und später dann im örtlichen Elektronikladen finanziert hat. Ohne deine Unterstützung wäre ich nicht so weit gekommen!

Allen die beim Korrekturlesen dieser Arbeit geholfen haben bedanke ich mich hier auch noch einmal herzlichst!

Zu guter Letzt sei auch Konstantin, Svetlana, Schrack-sempai, Tori, Bingo, Sarawat, Tine, Amanda und Dayve gedankt die für den nötigen Ausgleich neben der wissenschaftlichen Arbeit gesorgt haben.
